ABSTRACT

Title of Dissertation: BALLISTOCARDIOGRAPHY: MATHEMATICAL MODELING, ANALYSIS, AND APPLICATION TO CARDIOVASCULAR HEALTH MONITORING

Azin Sadat Mousavi, Doctor of Philosophy, 2022

Dissertation directed by: Associate Professor, Jin-Oh Hahn
Department of Mechanical Engineering

The main goal of this dissertation is to improve the early detection and management of cardiovascular (CV) disease by developing novel ultra-convenient CV health and risk predictor monitoring techniques based on a physiological signal called ballistocardiogram (BCG). BCG is the recording of heart-induced body movements. It has great potential to enable ultra-convenient CV health monitoring due to its close association with cardiac functions and its amenity for convenient measurement (i.e., measurement devices such as weighing scales and wearables). Nonetheless, the shortage of physical understanding of the BCG is a serious challenge that has hampered its effective use in CV health and risk assessment. The scope of this dissertation can be explained under three themes: (i) physics-based modeling of BCG, (ii) BCG recording, and (iii) challenges in wearable BCG-based cuffless blood pressure monitoring.

In the first part of the dissertation, a closed-form physics-based model is developed to estimate BCG from a single blood pressure waveform. The feasibility of this model in the estimation of CV risk predictors is studied. This model is inspired by our team's prior work hypothesizing that the main mechanism for the genesis of the head-to-foot BCG is the pressure gradients in the ascending and descending aorta (the major artery in the body). In addition, a systematic BCG feature selection approach is introduced leveraging the developed closed-form BCG model. This model-based approach is superior to previous ad-hoc feature selection techniques in that it incorporates physiological knowledge of the arterial system and unlike ad-hoc approaches which are data specific its findings can be generalized to different independent datasets.

BCG waveforms recorded with different sensors and devices have morphological differences. Therefore, the next part of this work is dedicated to the study of different BCG recording devices and the construction of a BCG measurement apparatus that enables the recording of true BCG (as estimated in the mathematical model). The efficacy of the BCG recording apparatus in measuring BCG is shown in two human and animal experiments.

Finally, BCG can enable cuff-less blood pressure (BP) tracking by virtue of two perks. It can easily be instrumented using wearables and it can be used as a proximal timing reference to calculate pulse transit time (PTT) which is the basis of the most common technique for cuff-less BP tracking. However, most wearable BCG-based studies for cuff-less BP monitoring have resorted to only one posture (standing with hands placed on the sides). Therefore, in this work, the effect of posture on wrist BCG-PPG PTT is investigated. This work reveals the posture-induced changes in PTT in-depth for the first time, by invoking and quantifying the effect of possible physical mechanisms responsible for such changes.

BALLISTOCARDIOGRAPHY: MATHEMATICAL MODELING, ANALYSIS, AND APPLICATION TO CARDIOVASCULAR HEALTH MONITORING

by

Azin Sadat Mousavi

Dissertation submitted to the Faculty of the Graduate School of the
University of Maryland, College Park, in partial fulfillment
of the requirements for the degree of
Doctor of Philosophy
2022

Advisory Committee:
  Associate Professor Jin-Oh Hahn, Chair
  Professor Alison B. Flatau, Dean's Representative
  Professor Balakumar Balachandran
  Professor Hosam Fathy
  Professor Miao Yu

Dedication

To my darling mother, Shahnaz, my beloved father, Jalal, my dear husband, Hossein, and my lovely sister, Negin.

Acknowledgements

I would like to express my deepest gratitude to my advisor Prof. Hahn for his guidance and support that was critical to the success of this research.

I am grateful to Mr. Majid Aroom for his insights and assistance in the fabrication of the BCG apparatus.

I would like to thank my co-workers Dr. Sungtae Shin, Dr. Peyman Yusefian, and Yang Yao for their collaborations and contributions to this research.

My sincerest thanks to Prof. Balakumar Balachandran, Prof. Amr Baz, Han Zhu, and Nishant Nemani for their assistance in testing the BCG bed apparatus.

I am grateful to Prof. Balakumar Balachandran, Prof. Alison Flatau, Prof. Hosam Fathy, and Prof. Miao Yu for serving on my dissertation committee.

My deepest thanks go to all my labmates including Ali, Drew, Ghazal, Jessie, Junxi, Mohammad, Peyman, Ramin, Richard, Stephanie, Weidi, Xin, Yekanth, Yuanyuan, and Zahra for their friendship and support.

Table of Contents

List of figures

List of Tables

List of Abbreviations

AIC	Akaike Information Criterion
BCG	Ballistocardiogram
BF	Blood Flow
BH	Breath Holding
BP	Blood Pressure
CO	Cardiac Output
CP	Cold Pressor
CV	Cardiovascular
CVD	Cardiovascular Disease
DB	Direct Body
DP	Diastolic Pressure
ECG	Electrocardiogram
FFT	Fast Fourier Transform
HF	Head to Foot
HR	Heart Rate
HS	Holding a Shoulder
IACUC	Animal Care and Use Committee
ICG	Impedance Cardiography
IPG	Impedance Plethysmography
IRB	Institutional Review Board

LF	Low Frequency
LVET	Left Ventricular Ejection Time
MA	Mental Arithmetic
MAE	Mean Absolute Error
MAP	Mean Arterial Pressure
NIH	National Institute of Health
PAT	Pulse Arrival Time
PC	Placed on the Chest
PEP	Pre-Ejection Period
PP	Pulse Pressure
PPA	Pulse Pressure Amplification
PPG	Photoplethysmogram
PTT	Pulse Transit Time
PWA	Pulse Wave Analysis
PWV	Pulse Wave Velocity
RMSE	Root Mean Square Error
SB	Slow Breathing
SCG	Seismocardiogram
SD	Standard Deviation
SP	Systolic Pressure
TL	Tube Load

TPR	Total Peripheral Resistance
ULF	Ultra-Low Frequency

Chapter 1: Introduction

1.1. Background

Cardiovascular disease (CVD) is the leading cause of mortality and morbidity that imposes a profound impact on health and the economy in the United States as well as globally. According to the recent statistics reported by the American Heart Association, CVD is currently responsible for more deaths each year than cancer and chronic lower respiratory disease (the second and third causes of death, respectively) combined in the U.S. CVD also represents a considerable economic burden to society: by 2035, 45.1 % of the U.S. population will have some form of the disease and the total healthcare costs are expected to reach $1.1 trillion. In 2014, 7.4 million cardiovascular (CV) surgical procedures were performed in the U.S., making it one of the two most frequently performed surgical procedures [1].

Considering the profound negative effect of CVD on public health and the economy, its effective and early detection and management are paramount. Achieving this goal requires ubiquitous and ultra-convenient CV health and risk predictor monitoring. However, existing technologies for non-invasive measurement of CV risk predictors (such as central systolic pressure (SP) and central pulse pressure (PP)) and cardiovascular parameters (e.g. stroke volume (SV) and cardiac output (CO)) suffer from a subset of the following factors that hamper their widespread use: requirement of a cuff or costly equipment, inconvenient measurement site, or the need for trained operators [1]–[7]. Consequently, novel technologies that complement current techniques through ultraconvenient measurement and tracking of CV risk predictors will be beneficial in enhancing the prevention, detection, and treatment of CVD.

It has been known for over a century that the body recoils every time the heart beats. Ballistocardiogram (BCG) is the recording of these heart-induced body movements. In recent years, there has been a resurgence of interest in BCG for CV health monitoring due to its close relation to cardiac function and amenity for convenient measurement. In fact, early investigators have shown that there may be a close association between BCG morphology and some cardiac events [8]–[11]. Besides, recent technological advances in electronics have led to ultraconvenient and noninvasive BCG instrumentation [12].

Blood pressure (BP), an important CV health factor, can particularly benefit from the new resurgence in BCG through cuff-less BP trend tracking. There are currently two popular approaches for cuff-less BP monitoring: (i) Pulse transit time (PTT) [13] and (ii) pulse wave analysis (PWA) [14]. PTT is the time required for an arterial pulse wave to travel between two different sites in the arterial tree. PTT is inversely related to BP. The PWA approach leverages state-of-the-art machine learning approaches to use fiducial points detected in an arterial pulse wave (e.g. BCG) as predictors of BP. Some recent studies use a fusion of PTT and PWA for ubiquitous BP monitoring.

1.2. Research Motivation

Efforts to understand the underlying mechanism of the BCG using phenomenological models have been rare and mostly unsuccessful due to either their failure to reproduce major BCG waves [15], [16] or their substantial complexity [8], [17]. In the absence of a mechanistic understanding of BCG, most studies have resorted to brute force data mining approaches in which they rely on ad-hoc correlation analysis between a subjectively chosen set of BCG features and CV parameters of interest [7], [18]–[21].

Recently, Kim et. al. hypothesized a mathematical model that could elucidate the underlying mechanism of BCG force generation in the head-to-foot direction of the body [22]. This model suggests that the generation of the BCG force is mainly due to pressure gradients in the ascending and descending parts of the aorta. Despite its significant success in explaining the mechanism underlying the genesis of the BCG, this model leaves some open questions.

First, **a challenge** with the current model is that it requires three central blood pressure (BP) waveforms at different arterial sites to predict BCG. In other words, it relates three arterial BPs to the BCG waveform. Therefore, in its current form the model is not practically useful for BCG-based CV risk predictor measurement because it only shows how the BCG results from the three aortic BP waves but not how the three aortic BP waves or CV risk predictors can be derived from the BCG. To address this challenge, a closed-form BCG model must be developed that can internally estimate two of the arterial BP waveforms from a single recorded BP waveform and use these waveforms to predict the BCG.

The question of associating the BP waveforms at different locations of the arterial tree is an open and popular problem among researchers. Tube-load (TL) model is a prevalent and effective physics-based model of arterial hemodynamics which is mathematically tractable, and its parameters are equipped with physiological meanings [23]. Different simplifying assumptions on the hemodynamics of the arterial tree have resulted in the development of a wide variety of TL models with different levels of accuracy and complexity. Most studies involving TL models considered the aorta as a tube with a constant diameter [24], [25], although in reality, this is not the case. Available anatomical data shows a gradual reduction in the diameter of the aorta as the measurement site gets farther from the heart [26]. Only a handful of studies have considered geometrical tapering and among those studies validation efforts in human data have been rare [27]–[29]. This fact has motivated us to assess the effect of incorporating arterial tapering on the estimations of the TL model.

Second, the model predicted BCG is not validated against the reference BCG measured in the same subject. For this purpose, experimental ground truth BCG waveforms (as well as invasive BP waveforms) should be recorded in the same subject. BCG waveforms recorded with different sensors and different devices have morphological differences [30]. Therefore, **the challenge** here is to experimentally instrument BCG in a way that has a close morphology to the model predicted BCG (a.k.a. "true BCG"). Hence, a BCG instrumentation device is constructed that can measure "true BCG". This BCG measurement apparatus would enable "true BCG" instrumentation in animal subjects that eventually can be used for the purpose of BCG model validation.

Third, it has been shown that BCG, measured by a scale-like device (i.e., whole-body BCG), along with a second pulse waveform can be used for PTT-based cuff-less BP monitoring, and even the BCG-based PTT-PWA fusion has the potential for independent monitoring of systolic and diastolic pressure (SP and DP, respectively) [31]. However, the majority of the existing work on PTT-PWA fusion largely resorts to ad-hoc approaches in the selection of PWA features and the aggregation of these features into BP predictors [7], [18]–[21]. Therefore, **an open challenge** in the cuff-less BP tracking via whole-body BCG is the systematic selection of the BCG PWA features.

Fourth, as mentioned earlier, PTT as the time interval between the fiducial points in BCG and a distal pulse wave (i.e., Photoplethysmogram or PPG) has a remarkable correlation with BP. However, a major shortcoming of the current studies on the BCG-PPG PTT is that their investigation is only limited to one posture standing with arms vertically held down in the head-to-foot direction. Considering the low signal-to-noise ratio associated with the wrist BCG signal, its acquisition must ideally be performed under minimal body motions. While standing posture is reasonably convenient, there are body postures more convenient than standing (e.g., sitting and supine) that may yield less body motion. In addition, constraining the arm to the main trunk (e.g., by placing the hand on the chest or by putting the hand on the shoulder) rather than holding it down vertically in the head-to-foot direction may help in suppressing the wrist motions during BCG acquisition. However, neither the influence of the postural deviation from standing with arms vertically held in the head-to-foot direction on the efficacy of wrist BCG-PPG PTT in cuff-less BP tracking nor the physical mechanisms responsible for the influence, is known. A prior work reported that posture influences the BCG signal [32]. Hence, it is possible that BCG-PPG PTT varies with respect to posture even when BP remains constant. Yet, prior research to understand the impact and mechanism of posture on the BCG and PTT is very rare. Therefore, **another open challenge** is to investigate the versatility and generalizability of wrist BCG-PPG PTT in cuff-less BP tracking in other body and arm postures.

1.3. Dissertation Scope

The scope of this dissertation can be placed under four general topics: BCG Modeling, application of BCG in CV health monitoring, BCG recording, and challenges in the way of using BCG for CV health monitoring.

1.3.1 BCG Modeling

CLOSED-FORM BCG MODEL: A closed-form mathematical model is developed that can predict the BCG waveform from an arterial BP waveform. The modeling effort comprises two parts. In the first section, a model is built that relates BP waveforms at different locations in the aorta to each other (model of arterial hemodynamics). In the next part, the final closed-form model is generated by leveraging the mathematical model describing the mechanism underlying the genesis of BCG (BCG mechanism model) and integrating it with the model of arterial hemodynamics. The validity of the closed-form BCG model is tested by comparing the predictions of the model with the BCG recordings in the literature.

1.3.2 Application of BCG Model in CV Health Monitoring

MODEL-BASED BCG SENSITIVITY SCHEME: A model-based scheme is developed for the systematic selection of BCG features using the developed closed-form BCG model. To do so, the BCG model is integrated with the physiological knowledge of the arterial system to develop a scheme for sensitivity analysis. The sensitivity analysis scheme is equipped with a small set of physiologically interpretable parameters and allows for the investigation of the effect of changes in the CV state [including changes in the underlying BP level as well as cardiac and vascular functions such as stroke volume, arterial load impedance, and heart rate)] on the morphology of the BCG waveform. The relationship between the BCG waves and various CV parameters is investigated by perturbing the CV variables that are input to the model. Next, we propose a set of a few BCG PWA features that are most sensitive to the CV parameters of interest. In the end, to show the efficacy of the model-based feature selection, the selected PWA features are used to develop predictors of BP and tested in an experimental human study.

1.3.3 BCG Recording

BCG APPARATUS CONSTRUCTION: A BCG apparatus is constructed to enable the reliable instrumentation of the BCG waveform in human and animal subjects. A BCG measurement apparatus is designed and manufactured based on the literature survey of the previous designs and updated with modern electronic sensors. Then, the apparatus is tested in human and animal experiments to confirm its efficacy in acquiring the BCG waveform.

1.3.4 Challenges in CV Health Monitoring with BCG

POSTURE DEPENDENT VARIABILITY OF PTT: We investigate the posture-dependent variability in the wrist BCG-PPG PTT. BCG and PPG signals are acquired from human subjects under the different body and arm postures. PTT is computed as the time interval between fiducial points in BCG and PPG waves, and its variability with respect to the different postures is analyzed by invoking an array of possible physical mechanisms.

1.4. Summary of Contributions

The unique contributions of this dissertation are as follows:

1. Validation of exponentially tapered tube-load model as a mathematical representation of arterial hemodynamics in human data.
2. Development of a new closed-form mathematical model that relates BP waveforms in different locations of the arterial tree to each other and provides the transfer function between a single BP waveform and a single BCG waveform.

3. Development of a new model-based sensitivity analysis scheme for the systemic selection of BCG PWA features.

4. Construction of a BCG measurement apparatus capable of recording BCG waveforms in humans and large animals for the purpose of future model validation

5. Study of posture-dependent variability in BCG-PPG PTT and proposing the physical mechanisms responsible for this variability

1.5. Dissertation Structure

The dissertation is arranged in the following format. In chapter 2, the current work on the existing CV health monitoring techniques, modeling of the arterial hemodynamics, the definition of BCG and its instrumentation techniques, and cuff-less BP measurement methods are reviewed. In chapter 3, a comparative study on two models of wave propagation in the human aorta is discussed. Chapter 4 is dedicated to the study of the BCG mechanism model and the development of the closed-form model of BCG that estimates BCG waveform from a single arterial blood pressure waveform. To this end, the model of arterial hemodynamics selected from the study in chapter 3 is integrated with our team's prior hypothesis that the BCG is generated from the pressure gradients in the ascending and descending portions of the aorta, the major artery in the body. Chapter 5 is on the application of the closed-form BCG model for developing a sensitivity analysis scheme for systematic BCG feature selection. This model-based selection method is tested in an algorithm developed for cuff-less BP trend tracking using human experimental data. Chapter 6 consists of the study of the physical basis of the BCG measurement device and its design and fabrication. Chapter 7 contains a study on the posture-dependent variability in wearable BCG-based pulse transit time (PTT). PTT is the basis of the most common technique for cuff-less BP tracking and this study can facilitate enabling the wearable BCG-based PTT and consequently cuff-less BP monitoring. Chapter 8 summarizes the contributions of this dissertation. Finally, chapter 9 proposes future directions to continue this research.

Chapter 2: Literature Review

In this literature survey, current CV health monitoring techniques, modeling of arterial hemodynamics, the definition of BCG and its instrumentation techniques, and cuff-less BP measurement methods are reviewed.

2.1. State-of-the-art Techniques for Cardiovascular Health Monitoring

Prevention of cardiovascular disease (CVD) can greatly benefit from the identification of proper biological markers. According to a standard definition introduced by an NIH working group in 2001, “a risk marker or biomarker is a characteristic that is objectively measured and evaluated as an indicator of normal biological processes, pathological processes or pharmacological responses to therapeutic interventions” [33]. Several studies identified arterial biomarkers, such as arterial stiffness, central BP, pulse wave velocity (PWV), pressure pulse amplification (PPA), and wave reflection indices as predictors for CVD morbidity and mortality.

1. Central and peripheral BP

BP waveforms vary continuously as they propagate further away from the heart down the arterial tree. This phenomenon happens because of wave propagation and reflection in the arterial tree [34]. Therefore, due to its proximity to the heart, central BP has more clinical value in CV risk assessment than its peripheral counterpart [35]–[37]. Yet, measurement of central BP has greater risk and cost which hampers its widespread clinical use. Peripheral BP is in general easier to measure than the central BP and that’s why it has been widely used in clinical practice.

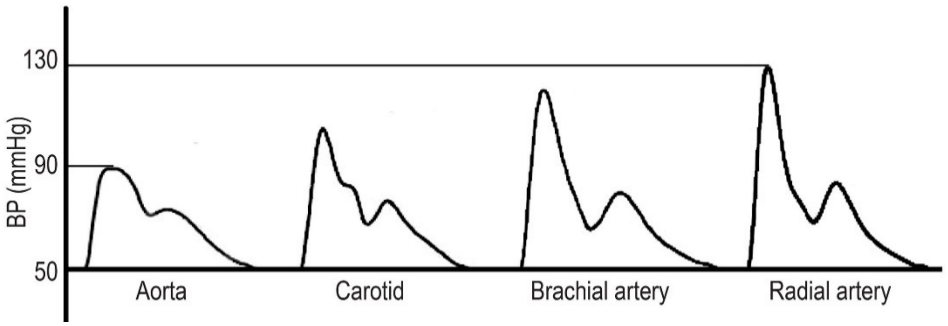

Fig. 2-1: BP waveforms as they move from the aorta to the radial artery [34]

Central BP waveforms can be measured using invasive and noninvasive techniques: in the invasive method, a catheter is placed inside the artery to measure the BP waveform. The strain gauge in the catheter contacts the fluid and measures the BP waves [24], [38]. An alternative non-invasive method of central BP measurement is carotid tonometry, which involves costly probes and trained operators [5], [6].

Several non-invasive methods have been developed for peripheral BP measurement: (i) auscultation, (ii) oscillometry, (iii) volume clamping, and (iv) tonometry. In the auscultation technique, an air cuff is placed around the arm and the systolic (SP) and diastolic pressures (DP) are found using the Korotkoff sounds. Oscillometry is like auscultation in that it requires a cuff. Small fluctuations of the cuff are measured to detect SP, DP, and mean arterial pressure (MAP). The volume clamp method needs a finger cuff and an optical sensor on the finger to measure BP. Tonometry is performed by applying the appropriate amount of pressure on an artery that is located near the surface to detect BP. When the sensor flattens the wall of an artery, tangential pressures are eliminated, and the sensor is exposed to the pressure within the artery which it records accurately. To apply the appropriate amount of "hold-down pressure" this technique requires trained operators.

In sum, all current methods of non-invasive BP measurement face one or more of these limitations: They need an external cuff, are bulky, and require a trained operator.

2. Pulse pressure amplification

Pulse pressure amplification (PPA) is the ratio between peripheral and central pulse pressures (PP) (pulse pressures = systolic pressure - diastolic pressure). Aortic-brachial PPA is a measure of arterial elasticity and an independent CV risk predictor [39]. To measure the PPA, a carotid-femoral tonometry procedure must be employed [2].

3. Pulse wave analysis (or equivalently Pulse transit time)

Pulse wave analysis (PWV) (or pulse transit time (PTT)) is the speed (or time) at which the arterial waveform propagates through the artery. It is an indicator of arterial stiffness. Measurement of PWV necessitates the inconvenient carotid-femoral tonometry technique [1], [3], [4].

2.2. Physics-Based Models of Arterial Hemodynamics

White box models of arterial hemodynamics have been long-standing. Researchers have used these physics-based mathematical models for making predictions and testing their understanding of the physiology underlying arterial hemodynamics. The available physics-based models may be divided into two classes: high-dimensional models and low-dimensional models as shown in Fig. 2-2. High-dimensional models including 2D and 3D models can give detailed descriptions of the local flow of the blood. These high-dimensional models are computationally complex and are generally used to simulate the local hemodynamics of specific arterial sites instead of the whole arterial tree [40]. In contrast to high-dimensional models, although less accurate, low-dimensional models have small computation costs, are more robust to inter-subject variability, and can reproduce many of the hemodynamic phenomena. Thus low-dimensional modeling has been employed by many researchers as an effective way to model the hemodynamic properties of the arterial tree in practice.

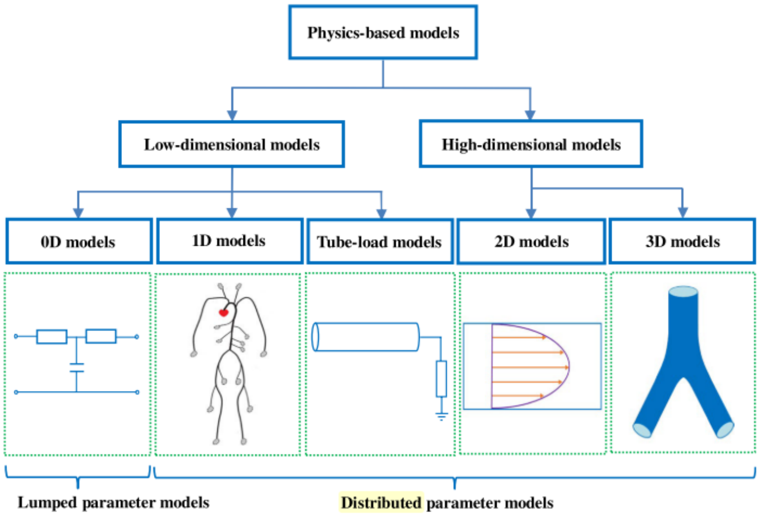

Fig. 2-2: The structure diagram of physical-based models in the cardiovascular system (source: [40]*)*

The low-dimensional models mainly consist of lumped parameter models, and distributed parameter models [40]. Lumped parameter models have a quite simple structure and are characterized by a small number of parameters that can be more easily estimated from clinically available arterial waveforms. The lumped parameter models are characterized by their pulse waveform, a function of time only. The most prevalent lumped parameter model is the "Windkessel" model proposed by Frank [41]. It models the arterial system as a capacitor, representing the large artery compliance (C), in parallel with a resistor, modeling the total peripheral resistance (TPR). Fig. 2-3 shows a simple Windkessel model. Although suitable for parameter estimation purposes, Windkessel models assume infinite pulse wave velocity (PWV) and therefore are unable to reproduce wave propagation and reflection phenomena that are essential in shaping the arterial waveforms.

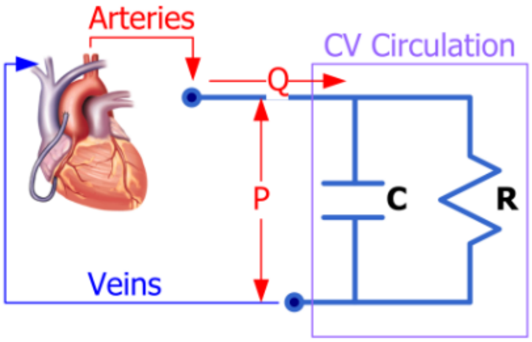

Fig. 2-3: Simple arterial Windkessel [42]

By contrast, distributed parameter models are capable of reproducing wave propagation and reflection dynamics by permitting finite PWV. Many distributed parameter models use the simplified Navier-Stokes equations to reproduce pressure and flow at any position in the entire arterial tree. Although these models tend to offer a much more accurate estimation of arterial hemodynamics, they need a large amount of computation. In addition, due to their excessively large number of parameters, they are difficult to identify which hampers their application in clinical practice [40].

Taking advantage of both Windkessel and distributed models, a middle ground model structure has been developed. This class of models is called tube-load (TL) models and has undergone much investigation by virtue of its ability to describe wave propagation and reflection and its mathematical tractability. These models are highly simplified transmission line models, which consist of multiple parallel tubes with terminal loads. The tube represents the wave propagation path in the large conduit arteries, whereas the load signifies the wave reflection site (e.g. arterial bed distal to a peripheral artery) [23]. Based on different assumptions, a wide variety of tube-load models with different complexities have been developed and investigated. The tube can be elastically and/or geometrically tapered or uniform as well as lossy (which exhibits energy dissipation) or lossless. There can also be different assumptions for the load. It can be non-parametric or parametric [23].

The most well-known TL model is the uniform lossless TL model [23], in which an artery of interest is modeled as a uniform lossless tube (or transmission line) terminated with a load that is in general frequency-dependent. In conjunction with the advances in novel techniques for estimating subject-specific parameters therein (e.g., (i) by fitting the TL model to diametric (such as arm and leg) BP waveforms and exploiting the fact that both of the diametric BP waveforms originate from the unknown yet common central BP [43], [44], or (ii) by fitting it to a distal BP waveform with physiologically relevant constraints that central blood flow is zero during diastole and/or central BP is smoother than distal BP [45]–[47]), the uniform lossless TL model is effective and robust in providing valuable insights related to the CV hemodynamics [48]–[56].

Despite its success thus far, the simplicity of the uniform lossless TL model motivates investigations for its potential improvement by incorporating more realistic components. In particular, arteries exhibit tapering, bifurcations, and BP loss. Due to the potential applicability of these models in clinical settings especially in the estimation of the central aortic waveforms, a lot of effort has been put into the validation of the tube-load models. Though, most of these validation efforts have been geared toward the validation of these models in animal data [42].

Among the handful of validation studies on human data, some of the extensions of uniform loss-less TL models have been investigated. It’s been shown that the TL models equipped with bifurcations and pressure loss demonstrate small but statistically significant improvement in their goodness of fit [57], [25].

However, the studies investigating the benefit of incorporating the geometric tapering into the TL model are mostly limited to animals. Table 2-1 shows the studies on the development and validation of the tapered tub-load models. To the best of our knowledge, only one study investigated the effect of geometric tapering in which the TL model was considered as a collection of multiple tubes in series with each other with variable diameters. No effort on the validation of exponential tapering in human data has been done.

Table 2-1: Studies on TL models with geometrical tapering

Year	Author	Validation data	Model description
1988	Einav, S. et. al. [58]	Model estimated data	20 segments, variable diameters
1995	Chang, K. et. al.[59]	Canine data	Linear tapering
1997	Fogliardi, R. et al. [27]	Canine data	Exponential tapering
2000	Segers, P., Verdonck, P. [28]	Hydraulic model data	Linear tapering
2007	Westerhof, B. et. al. [60]	No validation	7 segments, variable diameters
2018	Westerhof, B., Westerhof, N. [29]	Human data (literature)	Multiple segments, variable diameter

2.3. BCG Waveform, Mechanism, and Its Association with Cardiac Events

2.3.1 Cardiac Cycle

Every cardiac cycle is composed of different phases. A brief description of the events in the cardiac cycle can provide insights into the morphology of the ballistocardiogam and its association with cardiac events.

A single cardiac cycle can be divided into two basic phases: diastole and systole. Diastole represents the period of the time when ventricles are not contracting. Systole represents the time during which the left and right ventricles contract and eject blood into the aorta and pulmonary artery. During systole, the aortic and pulmonic valves open to permit ejection into the aorta and pulmonary artery. To analyze systole and diastole in more detail, the cardiac cycle is divided into multiple phases. The phases of the cardiac cycle are as follows:

1. Rapid filling of the ventricles
2. Slow filling of the ventricles
3. Atrial systole
4. Isovolumetric contraction
5. Rapid ejection
6. Slow ejection
7. Protodiastole
8. Isovolumetric relaxation

Fig. 2-4, often called the Wiggers diagram, shows the different events during the cardiac cycle for the left side of the heart. The top three curves show the pressure changes in the aorta, left ventricle, and left atrium respectively. The fourth curve shows the changes in left ventricular volume, the fifth depicts the electrocardiogram (ECG), and the sixth depicts a phonocardiogram, which is a recording of the sounds produced by the heart (mainly by heat vales) as it pumps [61].

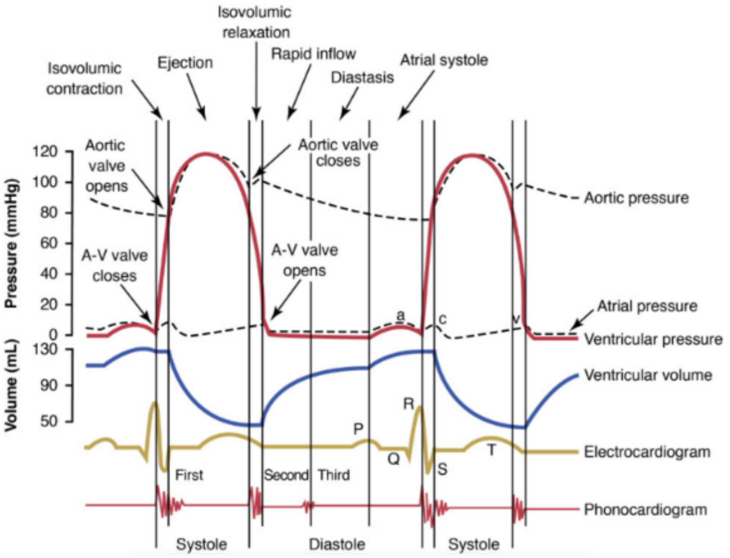

Fig. 2-4: Events in the cardiac cycle for left ventricle [61]

2.3.2 BCG Waveform

At every heartbeat, the blood traveling through the arterial tree produces changes in the center of mass of the body. Body micromovements are then produced by the reaction forces to maintain the overall momentum. Ballistocardiogram (BCG) is the recording of these heart-induced body movements [12]. BCG can be measured in different form factors such as displacement, velocity, and acceleration using a variety of devices (bed, chair, weighing scale, wearables) [12], [20], [62], [63]. Additionally, BCG is a vector quantity and can be measured in three dimensions.

The BCG waveform consists of a series of waves that are associated with each phase of the cardiac cycle. A typical whole-body BCG waveform in the head-to-foot direction is shown in Fig. 2-5 along with the name of each wave.

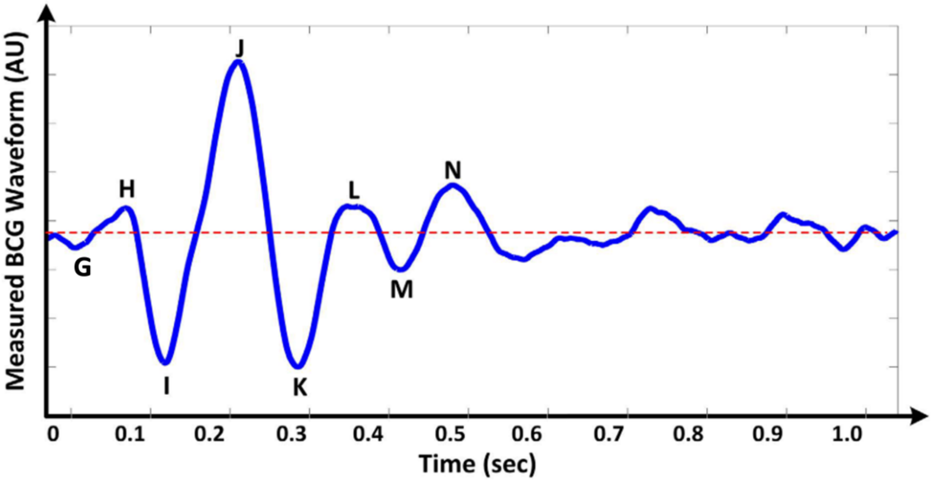

Fig. 2-5: An example of BCG waveform for one heartbeat [22]

Recently, Kim et. Al. introduced a mathematical model that could elucidate the underlying mechanism of BCG force generation in the head-to-foot direction of the body. They modeled the whole-body BCG as an instantaneous force in the head-to-foot direction. This model consists of two tubes in cascade which represent the ascending and descending part of the main artery of the body, the aorta (Fig. 2-6).

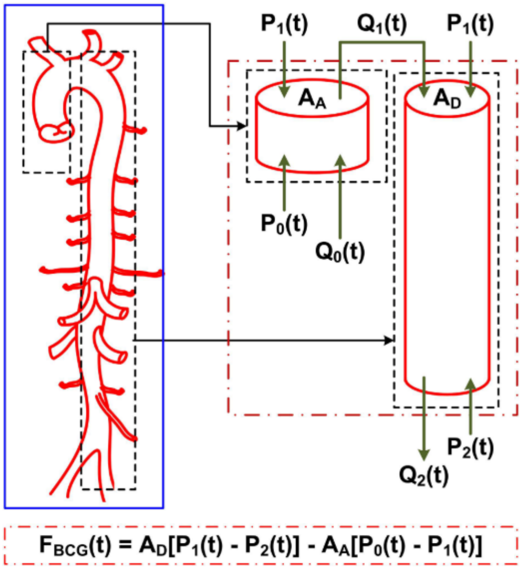

Fig. 2-6: A simplified model of the aorta to describe the mechanism of the BCG waveform. [22]

By analyzing the equilibrium of forces exerted on the blood in the aorta a simple model was developed that can estimate BCG [22].

$$\mathrm{F}_{\mathrm{BCG}} \approx A_D[P_1(t) - P_2(t)] - A_A[P_0(t) - P_1(t)] \tag{2-1}$$

This model suggests that the generation of the BCG force is mainly due to the pressure gradients in the ascending and descending aorta [22]. Leveraging this model, the authors described the mechanism of genesis of major BCG waves. Fig. 2-7 shows how the BP waveforms at the inlet, arch, and outlet of the aorta denoted by P_0, P_1, and P_2 construct the major BCG waves. According to the model and Fig. 2-7, the time of I wave initiation corresponds to the foot of the BP waveform at the inlet of the ascending aorta. The time of the J wave is associated with the foot of the BP waveform at the outlet of the descending aorta. Also, J wave amplitude may be proportional to relative changes in the aortic PP. The figure also shows that the amplitude of the J-K down-stroke is approximately proportional to the peripheral PP.

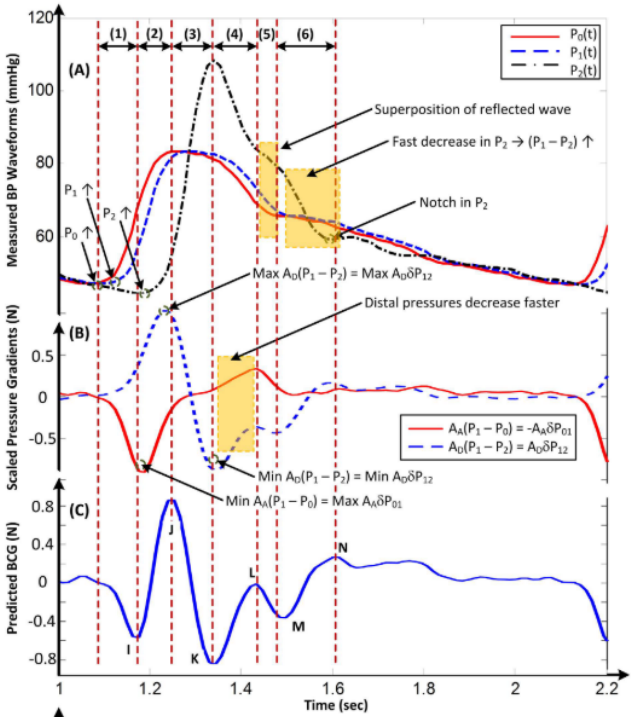

Fig. 2-7: Measured BCG waveform at different locations of the aorta, and corresponding estimated BCG waveform. (A) BP waveform at the inlet, apex, and outlet of the aorta (B) Force gradient in ascending and descending aorta (C) Estimated BCG waveform [22]

2.4. BCG Instrumentation

The BCG phenomenon was first documented by Gordon in 1877 [64]. He found out that as a subject stands on a weighing scale, the needle would vibrate synchronously with the subject's heartbeat [12]. Nearly 60 years later Starr and his colleagues designed an instrument in the shape of a table with a moving platform to measure BCG [65]. Throughout the 1900s until 1970, the classic BCG era, BCG was heavily investigated by researchers. However, after 1970 BCG was largely abandoned by investigators, due to its need for bulky measurement instruments and the advent of new technologies such as electrocardiogram and magnetic resonance imaging [12].

In recent years, technological advancements in electronics and signal processing, have simplified BCG instrumentation and assessment, which resulted in a resurgence of interest in this physiological signal in scientific and clinical settings. Fig. 2-8 shows several examples of modern BCG acquisition instruments that enable BCG measurement in various settings including in bed, at home, and in microgravity.

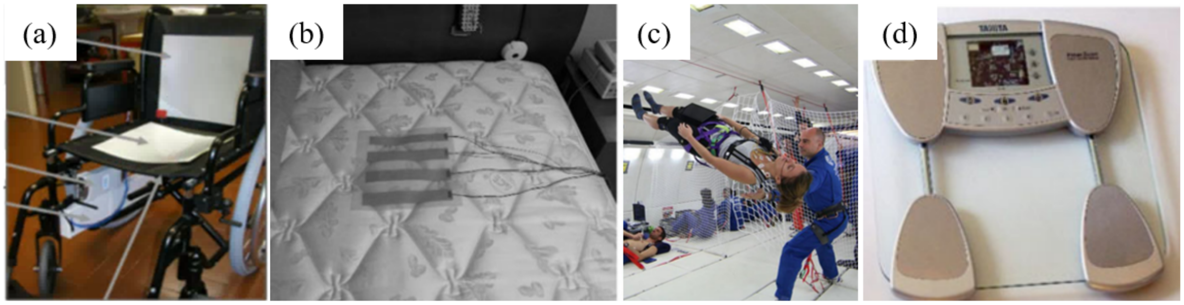

Fig. 2-8: Compilation of different examples of modern BCG measurement devices [63], [12]

2.4.1 Classical BCG Instrumentation Techniques

In this section, a summary of various BCG measurement systems that were developed in the classical BCG era is presented. Most types of classical BCG devices except for the direct body BCG consist of a platform on which the subject lies in the supine posture [66]. In 1956, the American heart association’s “Committee on Ballistocardiographic Terminology” divided the BCG instrumentation systems into four categories [67]: (i) high-frequency BCG (HF BCG), (ii) low-frequency BCG (LF BCG), (iii) ultra-low frequency BCG (ULF BCG), and (iv) direct body BCG (DB BCG)

This division is mostly based on the natural frequency of the BCG device with respect to the heart frequency (approximately 1 [Hz]). HF BCG generally has a higher frequency of 10 to 15 [Hz]. LF BCG apparatuses have a natural frequency of around 1 [Hz]. ULF BCG devices have a natural frequency of lower than 1 [Hz]. The DB BCG was considered an HF BCG and recordings of such devices were similar to recordings of HF BCG [67].

By the end of the BCG era, many studies suggested that the acceleration of ULF BCG may yield the BCG measurement over a wider range than the HF BCG devices and with less distortion due to the resonant properties of the body [68]. Therefore, ULF BCGs became the method of choice in classical BCG research [66]. Besides, studies on the BCG in microgravity suggested that these BCGs which ideally show the “true BCG” are closest in shape to the records obtained from ULF BCG devices [69]. As a result, since the plan in this dissertation is to fabricate a BCG measurement apparatus that can give the BCG measurement with the least distortion from the true heart-induced body movements, the ULF BCG devices developed in the classical BCG era were studied. Fig. 2-9 shows a compilation of the examples of ULF BCG devices.

Table 2-2 describes the ULF BCG devices found in the literature.

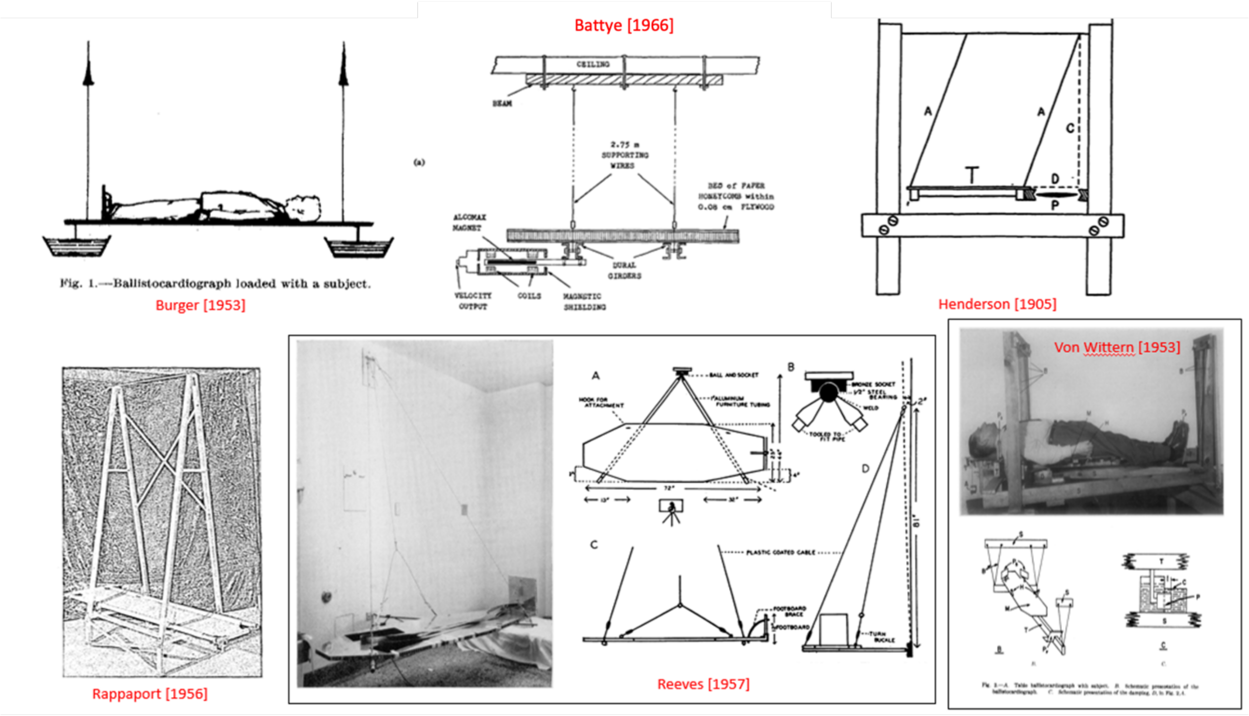

Fig. 2-9: Examples of ULF BCG measurement apparatus in classical BCG literature

Table 2-2: Examples of ULF BCG apparatus in classical BCG literature

Author [year]	Fn [c/s]	Cable Length	Bed Mass	Bed Frame	Suspension From	Damping	Lateral Motion	Form Factor	Locking
Burger [1953]	0.3	300 [cm]	5 [Kg]	Steel tube + canvas + vertical foot plate	Ceiling	Horizontal plate in treacle + 25% overshoot	Not constrained	Displacement	
Battye [1966]	0.3	275 [cm]	7.5 [kg]	Paper honeycomb sandwiched b/w sheets 0f 0.08 cm plywood + two cross girders made of duraluminum	Ceiling	Small damping in the head-to-foot direction	Four oil dashpots each underneath one end of the girders: Dip vertical plates oriented in the head to foot direction (lateral motion is overdamped)	Velocity	Raised and stabled by a hydraulic jack
Henderson [1905]	?	?	9 [Kg]	1.2 cm plank	Frame + two 10 cm pins to displace the bed laterally	None (Comment: breath holding)	Two 10 cm attached to one side of the bed	Displacement	Clutch Movement restricted to 8 [mm]

Author [year]	Fn [c/s]	Cable Length	Bed Mass	Bed Frame	Suspension From	Damping	Lateral Motion	Form Factor	Locking
Rappaport [1956]	0.1~0.25	6.5 [ft]	4 [lb]	61S-T1 aluminum frame + fabric + foot cross brace	Frame + 4 inches long pins displace the bed laterally	Frictional resistance / cotton pads / viscous fluid + overshoot < 20%	4 inches long pins attached to the rear	Velocity	Clamping device for loading Mechanical stop to limit movement
Reeves [1957]	0.1	Vertical length = 81 [in]	8 [lb]	Aluminum honeycomb panel (thick = 1 in)	Wall (cables suspended from a double ring hinge) + displaced laterally by V arm	Damping factor: 0.026	V-arm on ball and socket joint	Acceleration	
Von Wittern [1953]	0.6	V-shaped wires 70 [cm]	10 [kg]	Wooden T stricter + plate + foot and shoulder plates	Frame	Piston in an oil filled cylinder	V-shaped wires just allow longitudinal movement	Acceleration	

2.5. Cuff-Less BP Monitoring

Due to the limitation of the current BP monitoring techniques and with the advent of the new technologies (such as wearable technologies) many studies have been conducted on the cuff-less and continuous BP devices to incorporate them into daily objects and devices (e.g., weighing scales, chairs, wrist watches, and mobile devices) [12], [20], [63]. Recent studies have used the physiological signals (amenable to easy measurement) from such devices to enable ubiquitous (a.k.a. cuff-less) BP monitoring. Two alternative cuff-less BP monitoring techniques have been the focus of such studies: pulse transit time (PTT) and pulse wave analysis (PWA).

1. PTT-based approach to BP monitoring

PTT is the time required for an arterial pulse wave to travel between two different sites in the arterial tree, e.g., between a central artery and a peripheral artery. PTT can be simply measured by the time difference between proximal and distal arterial waveforms. PTT is famously known to have an inverse relationship with BP. This well-known physical relationship between BP and PTT is the basis of PTT-based BP monitoring. [7].

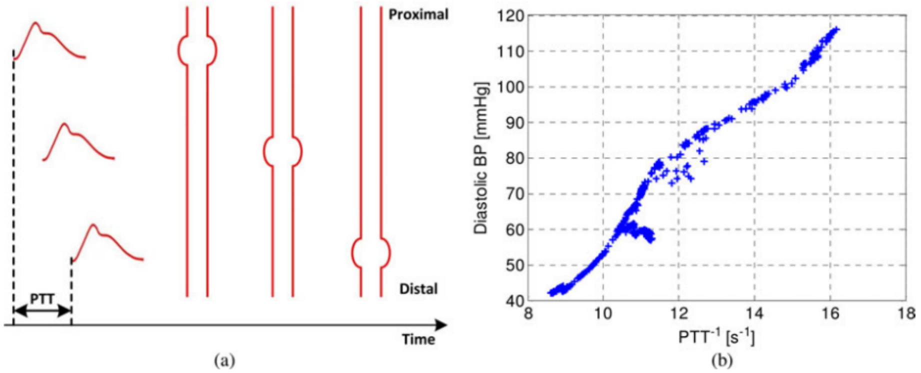

(a) (b)

Fig. 2-10: PTT provides a basis for cuff-less BP monitoring. (a) PTT is the time delay for the pressure wave to travel between two arterial sites and can be estimated from the relative timing between proximal and distal arterial waveforms. (b) PTT is often inversely related to BP. [7]

Most PTT-based techniques for cuff-less BP monitoring employed pulse arrival time (PAT: the time interval between the R-peak in the electrocardiogram (ECG) signal and a fiducial point in the photoplethysmogram (PPG)). In addition, some studies use impedance cardiography (ICG), ballistocardiogram (BCG), and seismocardiogram (SCG) to determine the PTT through cardiac mechanical vibrations [14].

2. PWA-based approach to BP monitoring

PWA approach exploits fiducial points in an arterial pulse wave to construct predictors of BP, often leveraging the state-of-the-art machine learning techniques [14]. In the existing body of work, PPG [70]–[72] and BCG [20], [73] as well as piezoelectric tonometry [74] have been explored primarily due to the amenity to easy instrumentation based on the wearables (e.g., a wristband).

3. PTT-PWA fusion approach to BP monitoring

More recently, there is an increasing interest in PTT-PWA fusion for ubiquitous BP monitoring. In general, it is natural to exploit PTT-PWA by capitalizing on the fiducial points in the arterial pulse waves already measured to compute PTT. In addition, noting that PTT computed using diastolic fiducial points may strictly correspond to only diastolic BP (DP) whereas PAT (which includes the pre-ejection period (PEP)) may better correspond to systolic BP (SP) than DP [75], PTT-PWA has the potential to enable independent tracking of DP and SP [76]. Prior work has reported the fusion of impedance plethysmography (IPG) PPG PTT and IPG PWA [77], IPG PTT and IPG PWA [78], [79], PAT and PPG PWA [80]–[83], BCG-PPG PTT and BCG PWA [84], BCG PTT-PWA [85], and PAT and PAT variability [86]. In particular, our team's prior work on PTT- PWA fusion based on the wearable BCG demonstrated the potential of BCG-based PTT-PWA fusion to achieve performance superior to PTT or PWA alone. Therefore, motivating its extension to whole-body BCG-based techniques for ubiquitous BP monitoring.

Chapter 3: Exponentially Tapered Vs. Uniform Tube Load Model

3.1. Introduction

Tube-load (TL) model has the potential to serve as an effective physics-based model of the arterial hemodynamics based on the following reasons: (i) it is characterized by a small number of parameters as opposed to the frequency response model, thus facilitating individualization with small amount of data; and (ii) all its parameters are equipped with physiological implications, thus facilitating the assessment of patient-specific CV health based on the individualized TL model parameters in conjunction with the BP waveform data. In fact, when combined with techniques for estimating subject-specific TL model parameters, the TL model is very useful in estimating and monitoring arterial hemodynamic indices[23]. The most well-known TL model is the uniform lossless TL model[23], in which an artery of interest is modeled as a uniform lossless tube (or transmission line) terminated with a load that is in general frequency dependent. In conjunction with the advances in novel techniques for estimating subject-specific parameters therein (e.g., (i) by fitting the TL model to diametric (such as arm and leg) BP waveforms and exploiting the fact that both the diametric BP waveforms originate from the unknown yet common central BP [43], [44], or (ii) by fitting it to a distal BP waveform with physiologically relevant constraints that central blood flow is zero during diastole and/or central BP is smoother than distal BP [45]–[47]), the uniform lossless TL model is effective and robust in providing valuable insights related to the CV hemodynamics[48]–[56].[1]

---

[1] This work has been published in [99].

Despite its success thus far, the simplicity of the uniform lossless TL model motivates investigations for its potential improvement by incorporating more realistic components. In particular, arteries exhibit tapering, bifurcations, and BP loss. Previous studies have investigated the TL models equipped with bifurcations and pressure loss to demonstrate that such an extension of the uniform lossless TL model may lead to small but statistically significant improvement in its goodness of fit. Along this path, the goal of this study was to investigate if there is any benefit in incorporating the geometric tapering into the TL model. To achieve this goal, this study comparatively investigated the tapered versus uniform TL models as a mathematical representation for BP wave propagation in human aorta. The relationship between the aortic inlet and outlet BP waves was formulated based on the exponentially tapered and uniform TL models. Then, the validity of the two TL models was comparatively investigated by fitting them to the experimental aortic and femoral BP waveform signals collected from 13 coronary artery bypass graft surgery patients.

This chapter is organized as follows. Experimental data, the TL models, and the data analysis details are given in section 3.2. Section 3.3 presents key results, which are interpreted and discussed in Section 3.4. Section 3.5 provides conclusions derived from this study.

3.2. Methods

3.2.1 Experimental Data

The experimental data collected in our prior work[56], [87] were used. In brief, invasive central aortic and femoral BP data were collected from 13 patients undergoing coronary artery bypass graft with cardiopulmonary bypass. Inclusion criteria were: (i) ages 18-80 years, inclusive, and (ii) scheduled for coronary artery bypass graft procedure with cardiopulmonary bypass. Exclusion criteria were: (i) scheduled for heart surgery other than coronary artery bypass graft which can incur distortion of central aortic BP waveform (e.g., aortic valve repair, etc.), (ii) female of childbearing potential, (iii) emergency surgery, and (iv) body mass index greater than 35. The study was carried out following the recommendations of the University of Alberta Health Research Ethics Board with written informed consent from all subjects. All subjects gave written informed consent in accordance with the Declaration of Helsinki. The protocol was approved by the University of Alberta Health Research Ethics Board (ID Pro00021889).

Data used in this work were collected right before or after the cardiopulmonary bypass. Following the induction of anesthesia and before the cardiopulmonary bypass, a catheter was inserted into the femoral artery. Then, a cannula was inserted into the ascending aorta by a surgeon immediately before or after the cardiopulmonary bypass. Then, ascending aortic and femoral arterial BP waveforms were recorded at a sampling rate of 1 kHz for up to 2 min.

3.2.2 Tube-Load Models

In this study, a variant of the exponentially tapered TL model of the aorta developed by Fogliardi et al. [88] and a uniform TL model were investigated (Fig. 3-1).The tapered TL model relates the aortic inlet ($P(j\omega,0)$) and outlet ($P(j\omega,L)$) pressures by way of the following transfer function:

$$\frac{P(j\omega,L)}{P(j\omega,0)} = H(j\omega|\theta_1,\theta_2,\theta_3) = \frac{2\theta_3\bar{\Delta}e^{-\left[\bar{\Delta}-\frac{\theta_1}{2}\right]}}{\theta_3\left(\bar{\Delta}+\frac{\theta_1}{2}\right)+j\omega\theta_2e^{\theta_1}+\left[\theta_3\left(\bar{\Delta}-\frac{\theta_1}{2}\right)-j\omega\theta_2e^{\theta_1}\right]e^{-2\bar{\Delta}}} \tag{3-1}$$

where $\theta_1 = qL$, $\theta_2 = \tau = L\sqrt{l_0 c_0}$, $\theta_3 = \frac{R_p}{Z_{c0}}$, and $\overline{\Delta} = \overline{\Delta}(\theta_1, \theta_2) = \sqrt{\left(\frac{\theta_1}{2}\right)^2 + (j\omega\theta_2)^2}$. The parameters are equipped with the following physical meanings: (i) q denotes the rate of tube tapering; (ii) L denotes the tube length; (iii) τ denotes the pulse transit time (PTT), time taken for the BP wave to travel from the inlet to the outlet of the aorta[75]; (iv) l_0 and c_0 denote the inertance and compliance per unit length at the tube inlet; and (v) R_p and Z_{c0} denote the terminal load resistance and tube characteristic impedance, respectively. The uniform TL model is derived as a simplified case of the tapered TL model when $q = 0$ (meaning that there is no tapering). Given that $\theta_1 = 0$ and $\overline{\Delta} = j\omega\tau$ when $q = 0$, Eq. (3-1) reduces to the following:

$$\frac{P(j\omega, L)}{P(j\omega, 0)} = H(j\omega|\theta_1 = 0, \theta_2, \theta_3) = \frac{2\theta_3}{(\theta_3 + 1)e^{j\omega\theta_2} + (\theta_3 - 1)e^{-j\omega\theta_2}} \tag{3-2}$$

It is noted that θ_1 implies the absolute extent of tapering between the tube inlet and outlet cross-sectional radii: $\frac{r(L)}{r(0)} = e^{-\frac{\theta_1}{2}}$. In addition, the reflection constant at the tube-load interface is given by $\Gamma = \frac{\theta_3 - 1}{\theta_3 + 1}$.

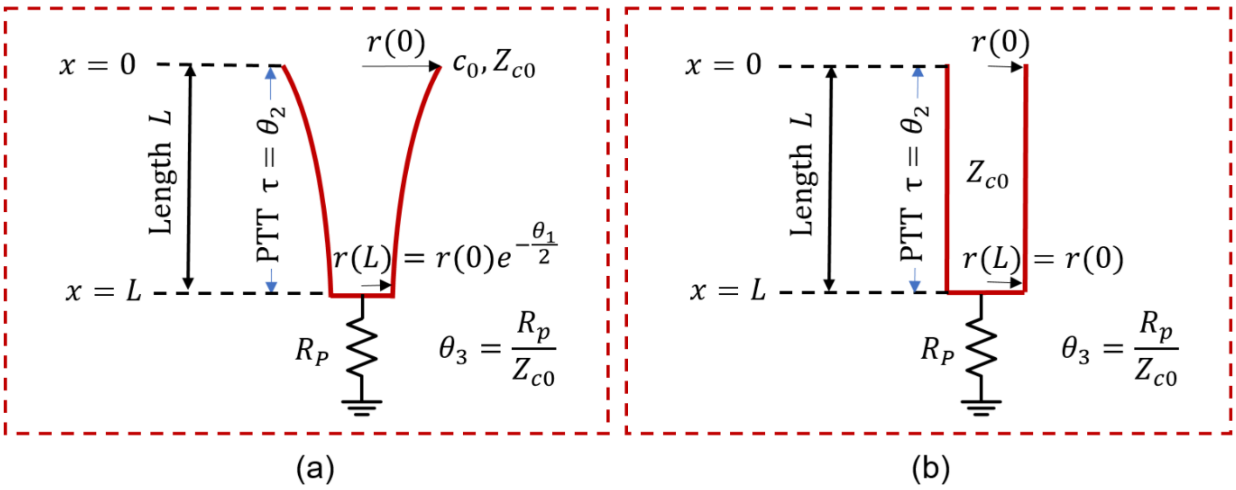

Fig. 3-1: Exponentially tapered (a) versus uniform (b) tube-load (TL) models. Exponentially tapered TL model is characterized by 3 parameters: $\theta_1 = qL$, $\theta_2 = \tau = L\sqrt{(l_0\, c_0)}$, $\theta_3 = R_p/Z_{c0}$ *, where q denotes the rate of tube tapering; L denotes the tube length;* τ *denotes the pulse transit time (PTT);* l_0 *and* c_0 *denote the inertance and compliance per unit length at the tube inlet; and* R_p *and* Z_{c0} *denote the terminal load resistance and tube characteristic impedance, respectively. Uniform TL model is derived as a special case of exponentially tapered TL model when* $q = 0$ *and is thus characterized by 2 parameters* θ_2 *and* θ_3.

3.2.3 Data Analysis

The validity of the tapered and uniform TL models was investigated and compared by fitting the models to the ascending aortic and femoral arterial BP waveforms associated with each subject on an individual basis. Details follow.

In each subject, a 15 beat-long pair of ascending aortic and femoral arterial BP waveforms were extracted from the recorded data and then down-sampled at 100 Hz. The first 10 beat-long data (called the training data) were used for model fitting, while the remaining 5 beat-long data (called the testing data) were used for assessing the validity of the models thus fitted. In this way, the TL models could be tested in the same CV state as when they were trained using the data not presented in the training process. For the sake of model fitting, the following optimization problem was solved using MATLAB and its Optimization Toolbox to derive the optimal parameter estimates θ^* associated with each subject from the training data:

$$\theta^* = \arg\min_{\theta \in \Omega_\theta} \left\| P(t, L) - \hat{P}(t, L|\theta) \right\| \tag{3-3}$$

where $P(t, L)$ is the aortic outlet BP (i.e., the femoral arterial BP) at time t, and $\hat{P}(t, L|\theta)$ is the aortic outlet BP at time t predicted by the (tapered or uniform) TL model equipped with the parameters $\theta = \{\theta_1, \theta_2, \theta_3\}$, when the aortic inlet BP (i.e., the ascending aortic BP) data were inputted. The domain Ω_θ was defined as $\Omega_\theta = \{\theta | \theta_1 > 0, \theta_2 > 0, \theta_3 > 0\}$ based on the physical meanings of the TL model parameters. The model-predicted aortic outlet BP $\hat{P}(t, L|\theta)$ was computed as follows. Given the set of TL model parameters θ at each iteration of optimization, the aortic inlet BP signal $P(t, 0)$ in the time domain was transformed via the fast Fourier transform (FFT) to yield the frequency-domain signal $P(j\omega, 0)$. Then, the frequency-domain aortic outlet BP signal $\hat{P}(j\omega, L|\theta)$ was computed as follows:

$$\hat{P}(j\omega, L|\theta) = H(j\omega|\theta_1, \theta_2, \theta_3) P(j\omega, 0) \tag{3-4}$$

Finally, $\hat{P}(j\omega, L|\theta)$ was transformed via the inverse FFT to yield the time-domain signal $\hat{P}(t, L|\theta)$.

It is well known that PTT is the most critical high-sensitivity parameter in the uniform TL model [56], [89]. Our parametric sensitivity analysis of the tapered tube-load model indicated that PTT is likewise the most critical high-sensitivity parameter in the tapered TL model. Hence, the TL model fitting problem in (3) was solved by (i) sweeping θ_2 over a physiologically plausible range while (ii) θ_1 and θ_3 were determined for each value of θ_2. In deriving the optimal θ_1 and θ_3

associated with each θ_2, multiple (85) initial guesses were employed to ensure that the solution obtained from the optimization problem corresponds to (or at least is very close to) global minimum. For each θ associated with each of the θ_2 values examined, the cost function in Eq. (3-3) was evaluated. Then, θ associated with the minimum cost function value was determined as θ^*. In this way, the integrity and accuracy of the estimated TL model parameters was maximized.

The validity of the TL models was then assessed using both testing and training data. The testing data were employed to assess (i) the goodness of fit including the root-mean-squared error (RMSE) and correlation coefficient (r value) between the measured aortic outlet BP waveform versus model-predicted aortic outlet BP waveform derived from the aortic inlet BP waveform as well as (ii) the accuracy-complexity trade-off via the Akaike Information Criterion (AIC), and also (iii) the goodness of fit including the root-mean-squared error (RMSE) and correlation coefficient (r value) between the measured aortic inlet BP waveform versus model-predicted aortic inlet BP waveform derived from the aortic outlet BP waveform (to assess the ability of the two TL models as the basis for estimating central from distal BP). The AIC was computed as follows:

$$\mathrm{AIC} = N \ln \frac{1}{N} \sum_{t=1}^{N} \left[P(t,0) - \hat{P}(t,0|\theta^*)\right]^2 + 2K + \frac{2K(K+1)}{N-K-1} \tag{3-5}$$

where N is the size of the testing data and K is the number of model parameters. The first term rewards the goodness of fit, while the second term penalizes the complexity. The third term is intended to compensate for the limited size of the testing data[90]. These metrics were first computed for both the tapered and uniform TL models on the subject-by-subject basis and then were aggregated across all subjects for comparison. For the RMSE and r value, mean and standard deviation (SD) were computed. The statistical significance in the difference in these metrics was determined using the Wilcoxon signed-rank test with the Holm-Bonferroni correction for multiple comparisons. For the AIC, the tapered versus uniform TL models were compared in terms of the number of subjects in which the AIC metric was smaller (note that smaller AIC implies superior accuracy-complexity trade-off). The training data were employed to assess (i) the frequency response of the two TL models in comparison to the data-based non-parametric frequency response in individual subjects as well as (ii) the physiological relevance of PTT values associated with the two TL models in comparison to the PTT derived directly from the aortic inlet and outlet BP waveforms using the intersecting tangent method [91].

3.3. Results

Table 3-1 summarizes the validity metrics of the tapered versus uniform TL models, including the RMSE, correlation coefficient (r value), and the number of preferred TL model (tapered versus uniform) in terms of the AIC values. Fig. 3-2 shows representative aortic outlet (femoral) BP waveforms derived from the two TL models associated with (a) $\theta_1 = qL \cong 0$ and (b) $\theta_1 = qL = 0.6$ when aortic inlet (central aortic) BP waveform was inputted. Fig. 3 shows representative frequency responses of the two TL models associated with (a) $\theta_1 = qL \cong 0$ and (b) $\theta_1 = qL = 0.6$ in comparison with the non-parametric frequency response derived directly from the aortic inlet and outlet BP waveforms. Table 3-2 summarizes the parameter values estimated for the two TL models. Fig. 3-4 compares the individual-specific PTT and reflection constant values between the two TL models. Fig. 3-5 shows the individual-specific PTT values associated with the two TL models in comparison to the PTT values derived directly from the aortic inlet and outlet BP waveforms.

Table 3-1: The validity metrics of the tapered versus uniform TL models, including the root-mean-squared error (RMSE), correlation coefficient (r value), and the number of TL models associated with the smallest Akaike Information Criterion (AIC) values.

	RMSE [mmHg]		Correlation Coefficient		AIC
	Outlet BP	Inlet BP	Outlet BP	Inlet BP	Outlet BP
Tapered TL	3.3+/-1.1	2.5+/-1.1	0.98+/-0.02	0.98+/-0.01	6
Tapered TL (1.7≤q≤3)	3.9+/-1.1*	2.8+/-1.1*	0.97+/-0.02*†	0.98+/-0.01*	0
Uniform TL	3.4+/-1.1	2.8+/-1.0*	0.98+/-0.01	0.98+/-0.01*	7

*: Significantly different from tapered TL ($p<0.05$ with Holm-Bonferroni correction). †: Significantly different from uniform TL ($p<0.05$ with Holm-Bonferroni correction).

Table 3-2: Parameter values estimated for the two TL models.

	PTT (τ) [ms]	Reflection Constant (Γ)	Tapering Constant (qL)
Tapered TL	78+/-16†	0.55+/-0.19*†	0.6+/-0.7*†
Tapered TL (1.7≤q≤3)	84+/-02†	0.73+/-0.09*†	1.7+/-0.1*†
Uniform TL	70+/-13*	0.43+/-0.15*†	0*

*: Significantly different from tapered TL ($p<0.05$ with Holm-Bonferroni correction). †: Significantly different from uniform TL ($p<0.05$ with Holm-Bonferroni correction).

(a) qL ~= 0

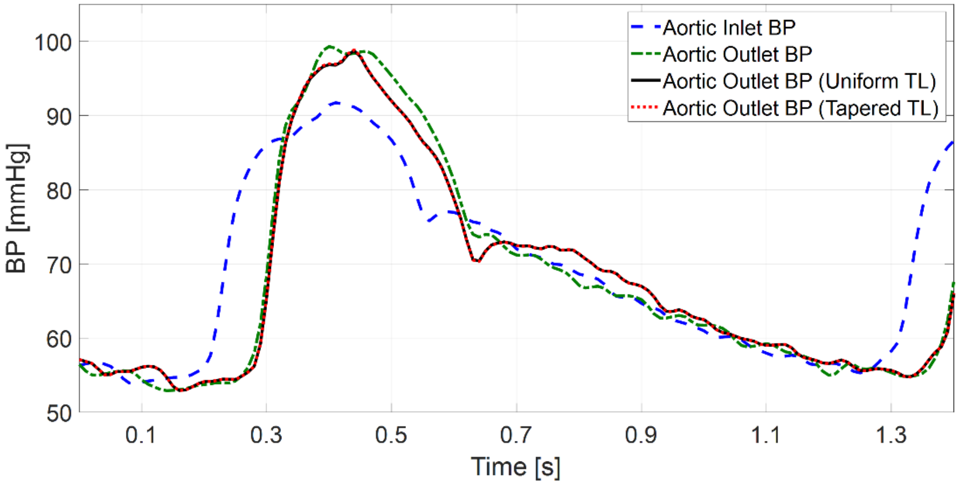

(b) qL = 0.6

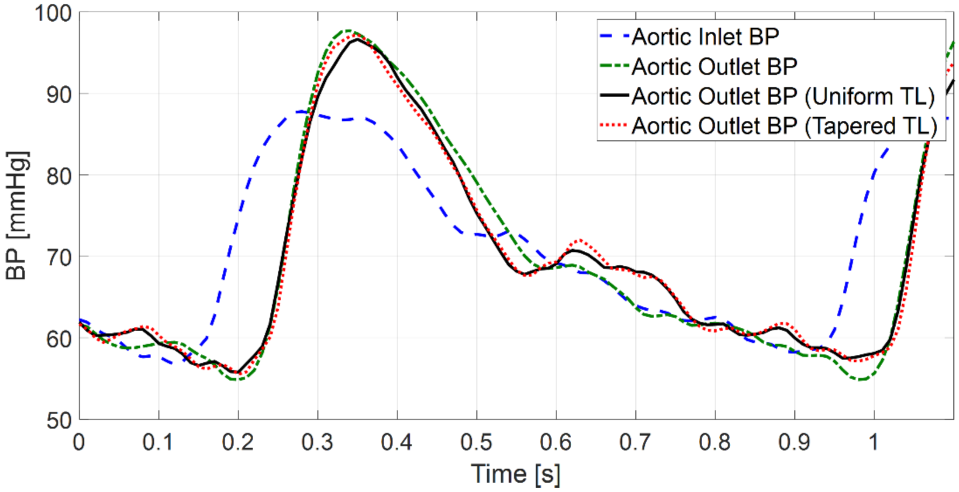

Fig. 3-2: Representative central aortic blood pressure (BP) waveforms derived from tapered versus uniform tube-load (TL) models when ascending aortic BP waveform was inputted. (a) Uniform TL model was preferred in terms of AIC (qL≅0). (b) Tapered TL model was preferred in terms of AIC (qL = 0.6).

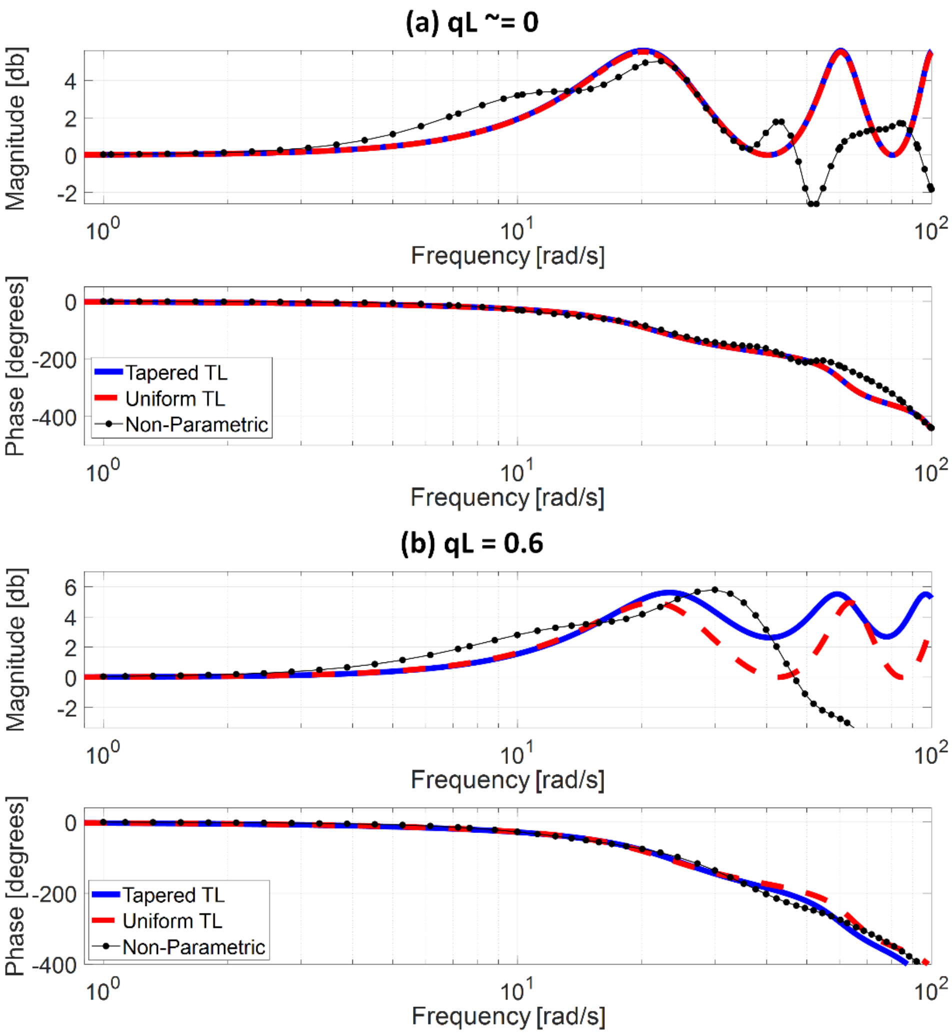

Fig. 3-3: Representative frequency responses of the two tube-load (TL) models in comparison with the non-parametric frequency response derived directly from the aortic inlet and outlet blood pressure (BP) waveforms. (a) Uniform TL model was preferred in terms of AIC ($qL \cong 0$). (b) Tapered TL model was preferred in terms of AIC ($qL = 0.6$).

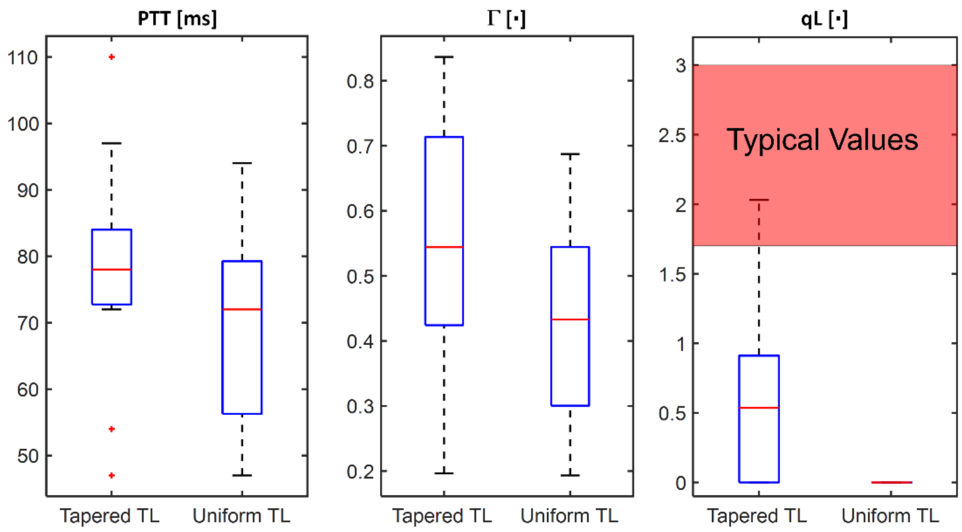

Fig. 3-4: Comparison of individual-specific pulse transit time (PTT), reflection constant (Γ) and radius ratio (qL) values associated with tapered versus uniform tube-load (TL) models.

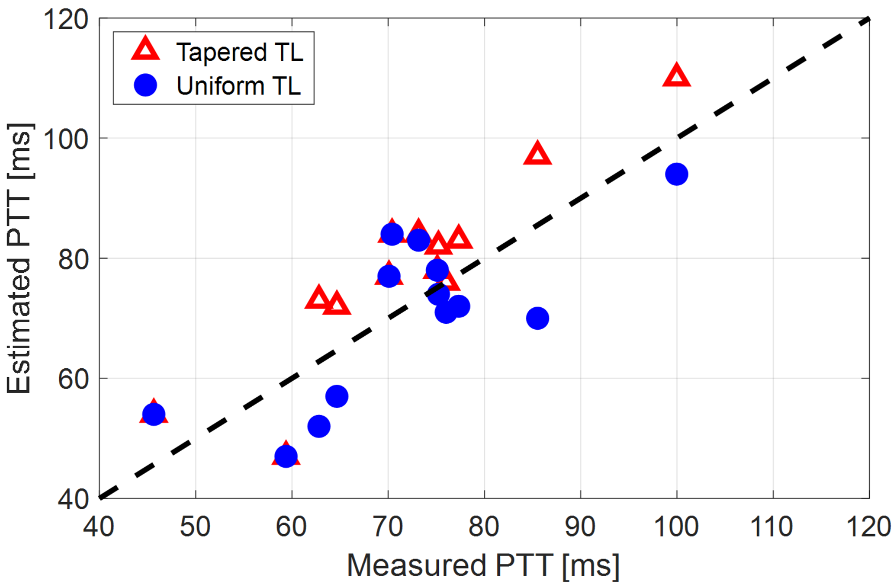

Fig. 3-5: Individual-specific pulse transit time (PTT) values associated with the two tube-load (TL) models in comparison to the PTT values derived directly from the aortic inlet and outlet blood pressure (BP) waveforms.

3.4. Discussion

The uniform TL model has the potential to enable patient-specific assessment of CV health with its minimal number of physiologically interpretable model parameters that may be individualized using a small amount of data. Despite its demonstrated success in CV health and disease monitoring applications, opportunities exist for its potential improvement by incorporating realistic components. In this study, the effect of adding an exponential tapering to the TL model as an approximation for aortic geometric tapering on its predictive performance and physiological relevance was investigated.

The exponentially tapered and uniform TL models exhibited comparable goodness of fit for the aortic outlet BP whose differences were not statistically significant, both in terms of RMSE and correlation coefficient (Table 3-1 and Fig. 3-2). The two TL models also exhibited frequency responses comparable to the non-parametric frequency response derived from the aortic and femoral BP waveforms in most patients (Fig. 3-3; note that the non-parametric frequency response may not be meaningful beyond ~30 rad/s considering that the energy associated with the arterial BP waveform is concentrated in the heart rate and its 3~4 harmonics and that the heart rate of the subject is ~1 Hz (Fig. 3-2)). As a consequence, the uniform TL model was superior to the exponentially tapered TL model in terms of AIC by virtue of its smaller number of requisite parameters (uniform: 2; tapered: 3): the former was preferred to the latter in 7 out of 13 subjects (Table 3-1). Although the number of subjects in which the uniform TL model was preferred to its tapered counterpart was not dominant, the difference in the goodness of fit between the two TL models was small even in the remaining 6 subjects in which the tapered TL model was preferred to its uniform counterpart (<3 % on the average in terms of RMSE; see Fig. 3-2(a) and Fig.

3-2(b)). Further, the frequency responses were quite comparable in the 6 subjects in which the tapered TL model was preferred to its uniform counterpart (see Fig. 3-3(a) and Fig. 3-3(b)). On the other hand, there was a notable difference between the two TL models in only 2 subjects. Hence, it may be argued that the uniform TL model is a viable model to represent the BP wave propagation in the aorta and that the benefit of using the exponentially tapered TL model may not be large. As an additional note, the goodness of fit for the aortic inlet BP associated with the same TL models showed that the tapered TL model was significantly superior to its uniform counterpart both in terms of RMSE and correlation coefficient. Yet, the absolute amount of difference was only marginal.

The comparable goodness of fit between the exponentially tapered and uniform TL models was supported by the values of the tapering constant ($\theta_1 = qL$) estimated for the exponentially tapered TL model: it was estimated to be 0.6 on the average, which corresponds to the aortic inlet-outlet radius ratio of 1.5. In addition, its value exhibited a large degree of inter-individual variability (1.17 in terms of the coefficient of variation). Interestingly, the tapering constant was very close to zero (corresponding to zero tapering and aortic inlet-outlet radius ratio of 1) in 6 out of the 13 subjects investigated in this study (including the subject shown in Fig. 3-2(a)), while in no subjects its value was large enough to be compatible with the anatomically plausible typical value associated with the femoral artery (~2.5, which corresponds to the aortic inlet-outlet radius ratio of ~3.5[92]–[94]). Despite its relatively small value, the aortic tapering also impacted the remaining parameters in the TL model. In particular, the PTT values derived from the fitting associated with the uniform TL model were comparable to the PTT measured directly from the aortic inlet and outlet BP waveforms (72+/-12 [ms]), whereas the PTT values derived from the fitting associated with the tapered TL model were significantly different from the PTT measured directly from the data (Table 3-2 and Fig. 3-4, Fig. 3-5). In fact, the tapered TL model exhibited a tendency of overestimating the PTT relative to the direct PTT measurements across all subjects (Fig. 3-5). In addition, the tapered TL model had significantly larger reflection constants than the uniform TL model (Table 3-2). These trends can be explained by analyzing the parametric sensitivity of the frequency response associated with the tapered TL model (especially, the amplitude (M_G) and location (F_G) of its first peak, which may be the most practically critical peak considering the limited frequency contents of the aortic BP signals [43]; Fig. 3-6). First, an increase in the tapering constant decreases the amplitude M_G of the first peak in the frequency response while increasing its frequency coordinate F_G (Fig. 3-6 (a)). Second, an increase in the PTT in the tapered TL model decreases F_G (Fig. 3-6 (b)). Third, an increase in the reflection constant in the tapered TL model increases M_G while decreasing F_G (Fig. 3-6 (c)). Putting them all together, the presence of aortic tapering in the tapered TL model is compensated for by the larger PTT and reflection constant relative to the uniform TL model (i.e., tapered TL model with zero aortic tapering), in such a way that the amplitude (M_G) and location (F_G) of the first peak in the frequency response associated with the two TL model remain the same as dictated by the data to be fitted.

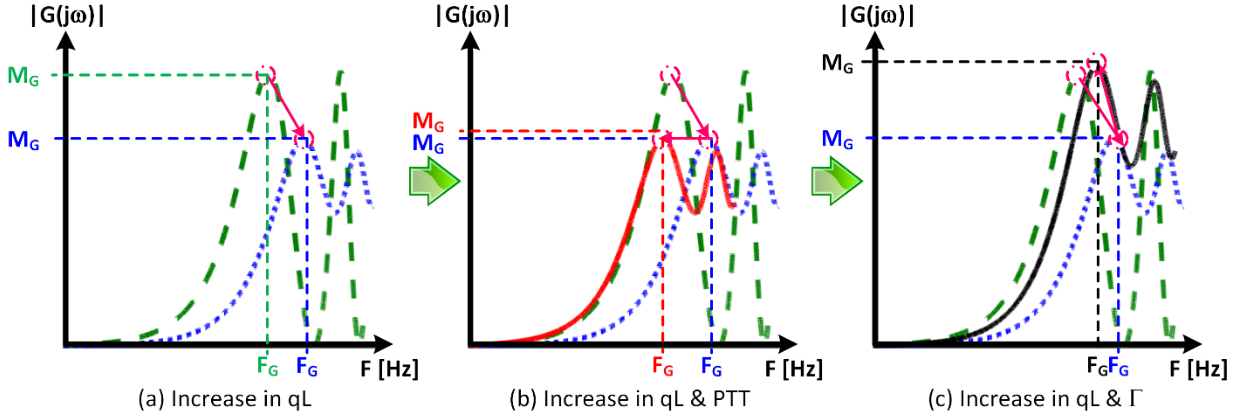

(a) Increase in qL

(b) Increase in qL & PTT

(c) Increase in qL & Γ

Fig. 3-6: Parametric sensitivity of the frequency response associated with the tapered tube-load (TL) model. (a) An increase in the tapering constant (qL) decreases the amplitude MG of the first peak in the frequency response while increasing its frequency coordinate F_G*. Green dashed line: frequency response of uniform TL model. Blue dotted line: frequency response of tapered TL model (qL>0) with pulse transit time (PTT) and reflection constant (Γ) identical to uniform TL model. (b) An increase in the PTT in the tapered TL model decreases* F_G*. Red solid line: frequency response of tapered TL model in (a) with larger PTT. (c) An increase in the reflection constant in the tapered TL model increases* M_G *while decreasing* F_G*. Black solid line: frequency response of tapered TL model in (a) with larger reflection constant.*

When the tapering constant was constrained in solving the model fitting problem in Eq. (3-3) to restrict the aortic inlet-outlet radius ratio in the vicinity of its anatomically plausible value (1.7~3.0), the exponentially tapered TL model underperformed the uniform TL model both in terms of RMSE and correlation coefficient (Table 3-1). Interestingly, the tapering constant was estimated to be its lower bound in most subjects (11 out of 13), which suggests that the exponentially tapered TL model tends to somehow minimize the degree of aortic tapering in order to maximize its goodness of fit. In addition, perhaps due to the restrictions imposed on the tapering constant, the values of PTT and reflection constant were significantly different from those associated with the uniform TL model (Table 3-2). It is noted that both PTT and reflection constant were significantly over-estimated relative to the uniform TL model, consistently with the insight obtained from the parametric sensitivity analysis in Fig. 3-6.

On the one hand, the results all in all suggest that exponential aortic tapering may not be physiologically relevant for at least two reasons. First, the TL model with exponential tapering tends to fall back to the uniform TL model as it is fitted to the experimental data. Second, the TL model with exponential aortic tapering exhibited poor predictive accuracy than the uniform TL model if anatomically plausible aortic tapering was enforced. In fact, this finding may be corroborated by a prior study, which showed that the tapered TL model did not exhibit superiority to its uniform counterpart in representing the aortic impedance[95]. On the other hand, the results may not be simply interpreted as there being no value in incorporating the aortic tapering into TL models in general. In fact, available anatomical data on the aortic radius with respect to the distance from the heart [92]–[94] could be fitted reasonably well with an exponential function ($r>0.97$; Fig. 3-7). In addition, aortic tapering is known to be associated with continuous wave reflection[96] as well as the distribution of atherosclerosis[97]. One plausible explanation for the limited benefit of incorporating aortic tapering in the TL model is that the aortic tapering estimated for the tapered TL model considered in this work includes the influence of aortic branching, which was not explicitly modeled in this work but is known to offset the aortic tapering to yield impedance matching in the forward direction[98]. In particular, considering that femoral BP was used as aortic outlet BP in this work and also that aortic branching rather than geometric tapering may be the primary factor responsible for the reduction of arterial diameter beyond the abdominal aorta, it may not be trivial to interpret the tapering constant estimated in this work. In this regard, it may be worth investigating how to appropriately incorporate both the aortic tapering and branching in order to enhance the TL models in terms of both goodness of fit and physiological relevance.

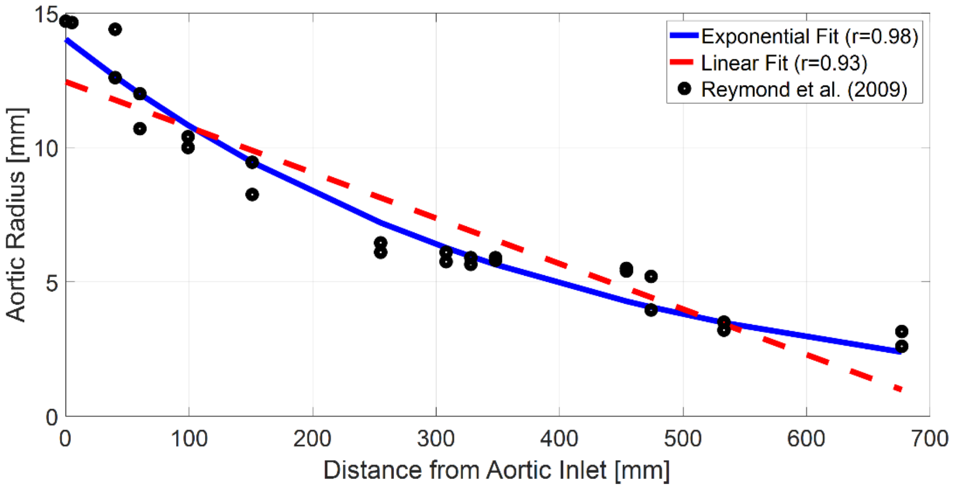

Fig. 3-7: Typical anatomical aortic diameter data with respect to the distance from aortic inlet (black circles) and its exponential (blue solid line) and linear (red dashed line) fits. The anatomical data are from a prior work [94].

3.5. Summary

The results of this chapter suggest that the uniform TL model may be more robust and thus preferred as the representation for BP wave propagation in the human aorta relative to the exponentially tapered TL model. In comparison with the uniform TL model, the exponentially tapered TL model may not provide valid physiological insight on the aortic tapering, and the improvement in the goodness of fit offered by the exponential aortic tapering may only be marginal. Considering that exponential aortic tapering is relevant from a physiological standpoint, future work on more rigorous investigation and refinement of exponentially tapered TL model will be rewarding.

Chapter 4: BCG Model

4.1. Introduction

The current understanding of the BCG waves is mostly limited to brute force data-driven analysis of the BCG waveform. There have been a few theoretical studies to explain the mechanism underlying the BCG waveform with limited success. While a few mathematical models of the BCG phenomenon have been proposed they either were not able to reproduce the primary BCG waveforms [15], [16] or were far too complex to give useful mechanistic insights [8], [17].

Recently, Kim et. al. mathematically modeled the BCG as the difference of pressure gradients in the ascending and descending aorta [22] and could reproduce the major waves in the whole-body BCG waveform. Kim's model, although insightful in that it shed light on the relationship between BCG and aortic BP waves, is not practically useful for the measurement of CV risk predictors based on BCG. The reason is that this model only elucidates how the BCG is constructed from the three BP waves, but the three BCG waves cannot be estimated from the BCG using this model. So, since many CV risk predictors can be derived from blood pressure pulse, the ultimate goal is to develop a model that can get a single conveniently measured BCG waveform and produce a blood pressure waveform. The first step in addressing this challenge is to relate one BP wave and one BCG waveform together. Hence, the goal of this chapter is to find a closed-form mathematical model that estimates BCG from only one BP waveform. Such a model enables us to investigate the effect of various CV risk predictors and parameters on the BCG.

To realize the goal of this chapter, first leveraging the uniform tube load model in chapter 3, a model is built that relates BP waves at different locations of the aorta (the major artery in the human body). Then this model is integrated with the BCG mechanism model in [22] to result in a closed-form BCG model that gets a single BP waveform as the input and produces a BCG waveform as the output. Fig. 4-1 shows the block diagram of the closed-form BCG model. In addition, to validate this model, the simulated BCG waveform from a typical BP waveform is compared with multiple typical BCG recordings reported in the literature in terms of shape and its capability to reproduce major BCG fiducial points.

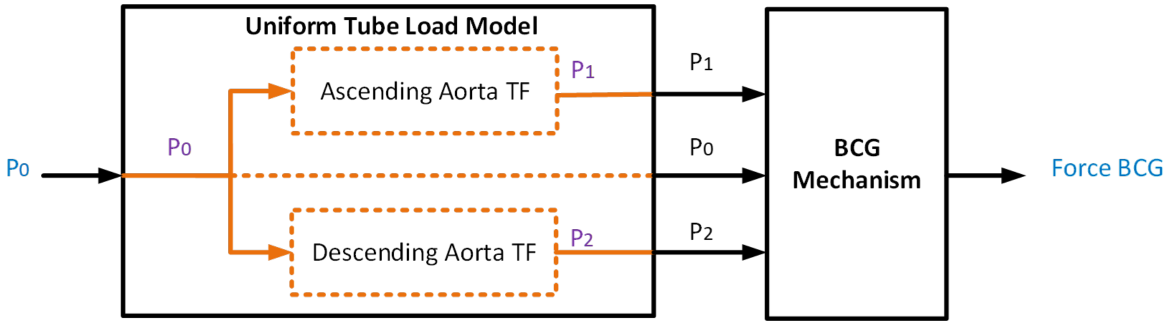

Fig. 4-1: The closed-form mathematical model to predict the BCG waveform from a single BP waveform

4.2. Closed-Form Mathematical Model of BCG and BP

A closed-form mathematical model to predict the BCG waveform from a single BP wave was conceived. The model was generated by the integration of the following two models:

1. A mechanistic model of the BCG force generation that estimates BCG force from three arterial BP waveforms
2. A transmission line (TL) model to mathematically associate the three BP waveforms at different arterial cites together

4.2.1 BCG Mechanism Model

The BCG mechanism model was adopted from our team's prior work [22]. In this work, the BCG waveform was modeled as an instantaneous force in the head-to-foot direction by analyzing the equilibrium of forces exerted on the blood in the main artery of the body (i.e., aorta). A simple model was resulted which suggested that the BCG is mostly due to the pressure gradients in the ascending and descending aorta. This model estimated the BCG from three aortic BP waveforms according to Eq. (4-1):

$$F_{BCG}(t) = A_D\big(P_1(t) - P_2(t)\big) - A_A(P_0(t) - P_1(t)) \tag{4-1}$$

Where, $F_{BCG}(t)$ is the BCG as the inertial force of the circulating blood, A_D and A_A are the descending and ascending aortic cross-sectional areas, $P_0(t)$, $P_1(t)$, and $P_2(t)$ are the aortic inlet, aortic arch, and the descending aortic BP waves [22]. Eq. (4-1) suggests that finding the BP waves from the BCG waveform is plausible.

4.2.2 Tube-Load Model

To find a closed-form relation between the BP wave and BCG wave we need to find transfer functions that mathematically associate $P_0(t)$, $P_1(t)$, and $P_2(t)$ together. To this end, we propose to find two transfer functions, $G_{21}(s)$ and $G_{01}(s)$ which are defined as: $L[P_2] = G_{20}(s)L[P_0]$ and $L[P_1] = G_{10}(s)L[P_0]$. Here, $L[.]$ is the Laplace transform. To find these two transfer functions the transmission line model of [99] is used to mathematically associate the BP at the inlet of a large artery to the BP wave at the outlet. To this end, the aorta is estimated as a uniform lossless tube with a type I load as shown in Fig. 4-2.

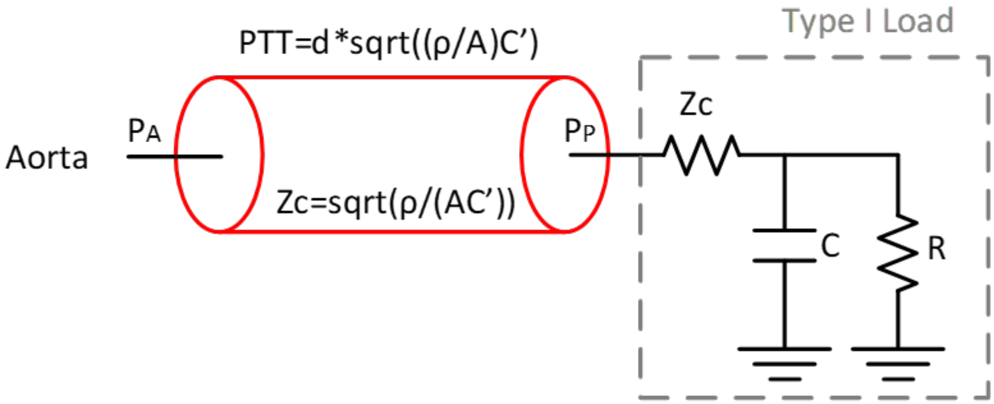

Fig. 4-2: Arterial tube load model with type I load [23]

In this model, d is the tube length, ρ is the blood density, A is the tube cross-sectional area, C' is the tube compliance per unit length, PTT is pulse transit time associated with the tube, Z_c is the characteristic impedance, P_A and P_P are the pressure pulse waves at the inlet and the outlet of the tube respectively, C is the load compliance, and R is the load resistance.

The arterial characteristic impedance, Z_c, can be found using the following equation

$$Z_C(MAP) = \sqrt{\frac{\rho}{A(MAP)C'(MAP)}} \tag{4-2}$$

As seen by Eq. (4-2), Z_c, A, and C' are all functions of mean arterial pressure (MAP). Therefore, if the values of cross-sectional area and unit length tube compliance are known for a specific MAP, then Z_c can be calculated.

Pulse transit time (PTT or T) which is the time that it takes for the arterial pulse wave to travel from the inlet of the tube to the outlet of the tube can be defined as below

$$T = d \times \sqrt{\frac{\rho \times C'(MAP)}{A(MAP)}} \tag{4-3}$$

For any load, the reflection coefficient at the load is given by the following relation [23].

$$\Gamma(j\omega) = \frac{Z_L(j\omega) - Z_c}{Z_L(j\omega) + Z_c} \tag{4-4}$$

Where, Z_L is the load impedance and can be shown as below for the special case of type I load shown in Fig. 4-2.

$$Z_L(j\omega) = Z_c + \frac{R}{1 + j\omega RC} \tag{4-5}$$

Simplifying for the type I load in the current model the reflection coefficient becomes as

$$\Gamma(j\omega) = \frac{R}{R + 2Z_c + 2j\omega Z_c RC} \tag{4-6}$$

The transfer function relating the central aortic pressure (P_A) waveform to a peripheral arterial pressure (P_P) waveform in the general case, is given as follows [23]:

$$P_P = \frac{1 + \Gamma(j\omega)}{e^{j\omega T} + \Gamma(j\omega)e^{-j\omega T}} P_A \tag{4-7}$$

Substituting Eq. (4-6) for reflection coefficient into Eq. (4-7), the following relationship is obtained:

$$P_P = \frac{1+\Gamma(j\omega)}{e^{j\omega T}+\Gamma(j\omega)e^{-j\omega T}} P_A = \frac{1+\dfrac{R}{R+2Z_c+2j\omega Z_c RC}}{e^{j\omega T}+e^{-j\omega T}\dfrac{R}{R+2Z_c+2j\omega Z_c RC}} P_A$$

$$= \frac{2R+2Z_c+2j\omega Z_c RC}{(R+2Z_c+2j\omega Z_c RC)e^{j\omega T}+Re^{-j\omega T}} P_A \tag{4-8}$$

$$= \frac{\dfrac{1}{Z_c C}+\dfrac{1}{RC}+j\omega}{\left(\dfrac{1}{2Z_c C}+\dfrac{1}{RC}+j\omega\right)e^{j\omega T}+\dfrac{1}{2CZ_C}e^{-j\omega T}} P_A$$

Therefore, setting $s = j\omega$, the transfer function, $G_{PA}(s)$, which describes the transformation relating P_A to P_P is defined as below.

$$G_{PA}(s) = \frac{P_P(s)}{P_A(s)} = \frac{\dfrac{1}{Z_c C}+\dfrac{1}{RC}+s}{\left(\dfrac{1}{2Z_c C}+\dfrac{1}{RC}+s\right)e^{sT}+\dfrac{1}{2CZ_C}e^{-sT}} \tag{4-9}$$

Now looking at the special case at hand, the aorta associated with the BCG model, can be represented as two tubes in series with each other where they are also in series with a lumped model that represents the load at the end of the aorta. Fig. 4-3 shows the diagram of this model.

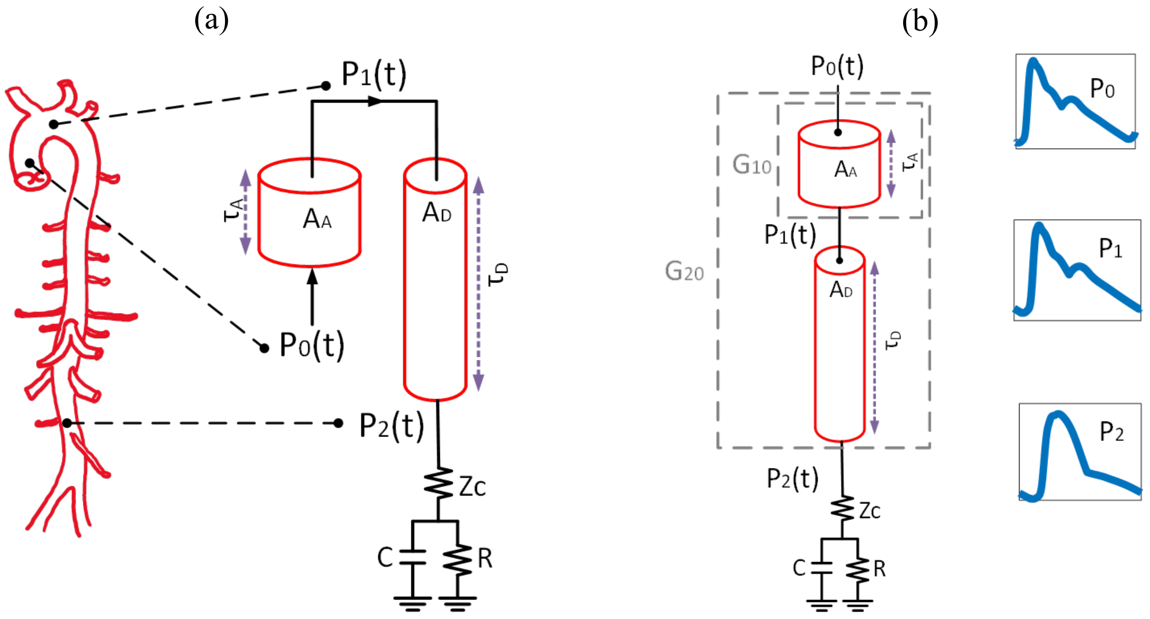

Fig. 4-3: Tube-load representation of the aorta. (a) shows a schematic of the aorta and its component as lumped blocks (b) Shows the block diagram of mathematical components of the aorta and its peripheral load as well as representative BP waves at the aortic inlet (P0), aortic arch (P1), and aortic outlet (P2)

To find the transfer function for the ascending aorta, $G_{10}(s)$, some simplifying and physiologically plausible assumptions are considered. In the model of $G_{10}(s)$, the tube is short and therefore the change in BP shape from the inlet to the outlet of the tube is very small. Consequently, the transfer function $G_{10}(s)$ that shows the transformation between P_0 and P_1 can be written as:

$$G_{10}(s) = \frac{P_1(s)}{P_0(s)} = e^{-\tau_A s} \tag{4-10}$$

which shows P_1 is found by lagging the aortic inlet pressure (P_0) by a pulse transit time, τ_A. τ_A is the time associated with the duration it takes the BP pressure wave to reach the aortic arch from the aortic inlet.

In addition, to find $G_{20}(s)$, the exact model in Fig. 4-2 is used. In this model, the portion of the aorta from the aortic inlet to the outlet of the artery at the femoral site is shown with the tube and the rest of the arterial tree after that comprises the load that is shown with three lumped elements. Therefore, substituting P_0 and P_2 and $T = \tau_D$ in Eq. (4-9), the relationship for G_{20} which is the transfer function relating P_0 to P_2 can be written as

$$G_{20}(s) = \frac{P_2(s)}{P_0(s)} = \frac{\frac{1}{Z_c C} + \frac{1}{RC} + s}{\left(\frac{1}{2Z_c C} + \frac{1}{RC} + s\right) e^{s\tau_D} + \frac{1}{2CZ_C} e^{-s\tau_D}} \tag{4-11}$$

Here, τ_D is the pulse transit time associated with the descending portion of the aorta.

4.2.3 The Transfer Function of the Closed-Form BCG Model

Having the transfer functions $G_{10}(s)$ and $G_{20}(s)$, Eq. (4-1) is transformed to the following mathematical model for estimating the BCG in the Laplace domain:

$$\begin{aligned} F_{BCG}(s) &= A_D\big(P_1(s) - P_2(s)\big) - A_A\big(P_0(s) - P_1(s)\big) \\ &= A_D\big(G_{10}P_0(s) - G_{20}P_0(s)\big) - A_A\big(P_0(s) - G_{10}(s)P_0(s)\big) \\ &= \Big(A_D\big(G_{10}(s) - G_{20}(s)\big) - A_A\big(1 - G_{10}(s)\big)\Big) P_0(s) \\ &= \left(A_D \left(e^{-\tau_A s} - \frac{\frac{1}{Z_c C} + \frac{1}{RC} + s}{\left(\frac{1}{2Z_c C} + \frac{1}{RC} + s\right) e^{s\tau_D} + \frac{1}{2CZ_C} e^{-s\tau_D}} \right) \right. \\ &\quad \left. - A_A(1 - e^{-\tau_A s}) \vphantom{\frac{1}{1}} \right) P_0(s) = H(s)P_0(s) \end{aligned} \tag{4-12}$$

Where, $H(s)$ is the closed-form transfer function relating P_0 to BCG wave. This mathematical relation has 6 unknowns, A_A, A_D, τ_A, τ_D, Z_cC, RC and their nominal values can be obtained from the experimental data reported in the literature.

4.2.4 Model-Based Estimation of the BCG Wave

To simulate BCG using this model, first, a representative BP waveform was generated based on the physiological knowledge of the cardiovascular system provided in the literature. The typical BP waveform was fed into the closed-form BCG model represented by Eq. (4-12). Nominal values for the parameters of the model were chosen based on the information from the literature. A representative BCG waveform was computed in the end as a result of plugging in the representative BP wave into the nominal closed-form BCG model. Fig. 4-4 shows the representative BP wave at the inlet of the aorta, as well as the intermediate BP waves computed in the model, at the aortic arch and outlet of the aorta.

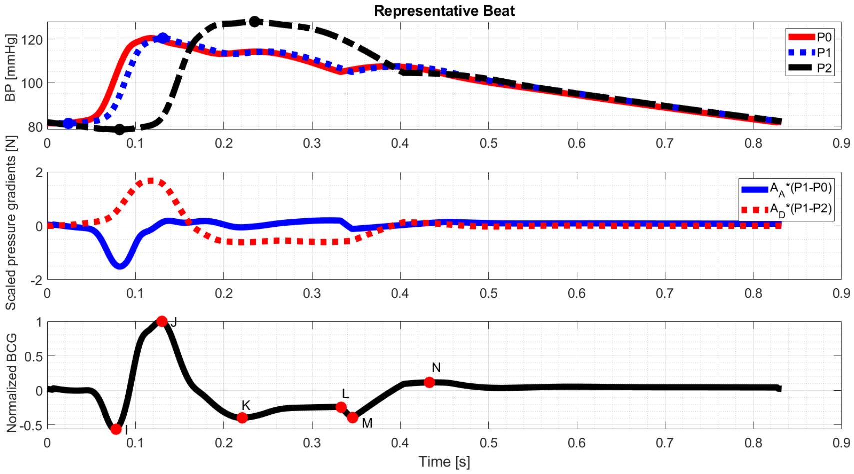

Fig. 4-4: A representative BCG waveform computed by the mathematical model with nominal parameters. The major BCG waves (i.e., I, J, K, L, M, N waves) are shown as red dots on the BCG waveform.

In addition, the figure shows the simulated pressure gradients in the ascending and the descending parts of the aorta, the major artery in the body, which are the main reason for the generation of BCG according to the BCG mechanism model. Moreover, the figure also, shows the model estimated BCG waveform.

4.3. Closed-Form Model Validation

The validity of the model with respect to the experimental data was assessed in the following way: the ability of the model to reproduce the major BCG waves was investigated. To this end, the experimental BCG waves reported in the literature were collected from 6 papers, [100]–[105], and normalized with respect to the amplitude of their J wave. Then, the major BCG waves in the waveforms from the literature were averaged and +/-2SD confidence interval regions were computed for each of the major BCG waves. Then the morphology of the J peak-normalized BCG waveform estimated from the model with nominal parameter values was compared with the average BCG waveform from the literature. The close morphological similarity of the BCG waveform to in vivo experimental BCG measurements in the literature (Fig. 4-5) supports the validity of the mathematical model.

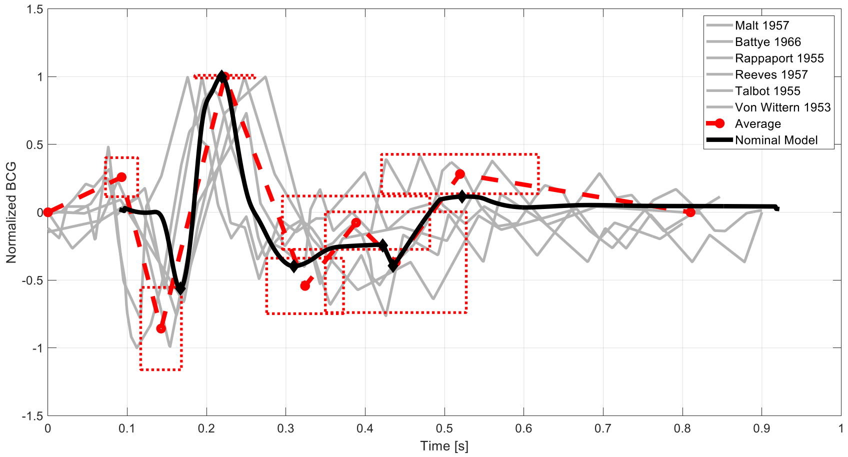

Fig. 4-5: Examples of in vivo experimental BCG measurements in the literature.

4.4. Conclusion

In this chapter, a closed-form mathematical model was developed that could predict the BCG waveform from a single arterial BP waveform. The model can be defined using 6 model parameters that are physiologically interpretable. A representative BP waveform along with nominal values for model parameters were inputted to the model and a BCG waveform was predicted as the output. The simulated BCG waveform showed close similarity with six BCG waveform recordings from the literature that supports the validity of the model.

Chapter 5: Application of the Closed-Form BCG Model in Unobtrusive Cardiovascular Parameter Monitoring

5.1. Introcution

Ballistocardiogram (BCG) has the potential to realize unobtrusive cardiovascular (CV) parameter monitoring. Studies have shown that characteristic features extracted from BCG can be convenient and effective surrogates of CV parameters such as arterial blood pressure [85], [106], pulse transit time (PTT) and pulse wave velocity [85], [106], [107], and cardiac output (CO) [18][108].

Despite reasonable success, most of the prior studies on BCG-based CV health monitoring face a common challenge. In the absence of physiological knowledge of BCG, most studies resort to ad-hoc data-driven approaches in which they investigate the association between a set of subjectively selected BCG features to the target CV parameters [18], [19], [21], [109], [110]. Therefore, the features thus selected may only pertain to the specific data under study and may not generalize to other data.

To overcome this challenge, in this chapter a systematic approach to BCG feature selection for CV parameter monitoring was developed based on the closed-form BCG model. Hence, the results of the model-based analysis do not depend on a specific data set which is the key advantage of this approach.

The objective of this chapter was to develop a model-based approach for the systematic selection of BCG wave features for effective unobtrusive tracking of CV parameters. The closed-form BCG model was extended using the physiological knowledge of the arterial system. The result was a model that could be fully defined by setting four physiological variables associated with a specific cardiovascular state. Then using this extended mathematical model, a sensitivity analysis was performed by perturbing the inputs to the model (CV parameters) to simulate different cardiovascular states. Next, the effect of these perturbations on the output of the model (BCG wave and subsequently BCG features) was investigated. Afterward, three candidate BCG features most sensitive to each CV parameter of interest were selected. To evaluate the efficacy of the feature selection method, two approaches were utilized using the experimental whole-body (scale) BCG data collected from 17 human subjects: (i) The experimental BCG features were ranked based on their sensitivity to the CV parameters; then the experimentally developed ranking was compared with the model-based ranking. (ii) Two regression models based on the fusion of PTT and PWA (pulse wave analysis based on the BCG waveform) for the estimation of systolic and diastolic pressures were developed and compared using (a) all the experimentally available BCG features and (b) the set of 3 model-selected BCG features.

The innovations of this chapter were (i) the development of an extended mathematical model that can generate BCG waveform from a set of four physiological variables, and (ii) systemic selection of BCG features based on model-based sensitivity analysis.

5.2. Extended Mathematical Model

To achieve the goal of this chapter, first, the closed-form BCG model in chapter 4 was extended to receive a blood flow (BF) waveform and produce the BCG waveform. Then, the model was characterized by a set of physiologically relevant rules that relate the model parameters to 4 physiological variables (i.e., age, heart rate (HR), stroke volume (SV), and total peripheral resistance (TPR)). As a result, the BCG waveform can be simulated by inputting a template BF waveform and the 4 physiological variables which indicate a specific cardiovascular state (Fig. 5-1).

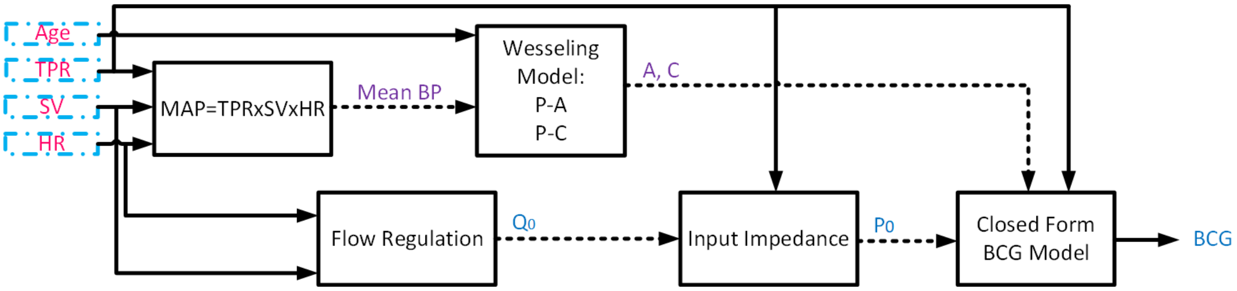

Fig. 5-1: A mathematical model to predict the BCG waveform from the heart blood flow waveform based on the age, HR, SV, and TPR parameters.

In the first step, a typical blood flow waveform is constructed from the flow waves reported in [111] and leveraging the assumption that flow is zero during the diastole. The typical BF is shown in Fig. 5-2.

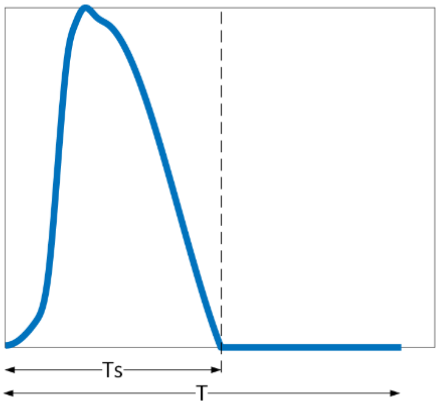

Fig. 5-2: Typical Blood Flow (BF) waveform

In this BF waveform, T is the heart period (inverse of the heart rate, $T = \frac{1}{HR}$ and T_s is the left ventricular ejection period.

If the values of age, HR, SV, and TPR are known and entered as inputs to the model the flow wave is adjusted to represent these values using the following relations. T_s can be computed from the heart rate (HR) according to the following equation

$$T_s = 0.417 \times (1 - e^{-2T}) \tag{5-1}$$

In addition, the amplitude of the BF wave is adjusted in a way that the integral of the area under the BF wave during the left ventricular ejection period, SV, is equal to the value entered as the input to the model. In other terms, SV is the volume of blood ejected from the left ventricle in each beat.

Cardiac output is the volumetric flow rate of the heart pumping output and is calculated by

$$CO = HR \times SV \tag{5-2}$$

The mean arterial pressure can be computed from Frank's Windkessel model. This model describes the hemodynamics of the arterial system in terms of resistance and compliance. Using Frank's well-established relation between the TPR and cardiac output (CO) the mean arterial pressure (MAP) was computed [41].

$$MAP = CO \times TPR \tag{5-3}$$

The arterial cross-sectional area, $A_D(P)$, of the descending aorta, and the unit length compliance are functions of mean arterial pressure (MAP) and were computed according to the model proposed in [112]. Eq. (5-4) shows how $A_D(P)$ was computed [112].

$$A_D(MAP) = A_{max}\left[0.5 + \frac{1}{\pi}\arctan\left(\frac{MAP - P_0}{P_1}\right)\right] \tag{5-4}$$

Where, A_{max}, P_0, and P_1 are the constants in the model that were defined and evaluated experimentally according to [112].

The unit length compliance is the derivative of $A_D(MAP)$ with respect to MAP.

$$C'(MAP) = \frac{A_{max}/\pi P_1}{1 + \left(\frac{MAP - P_0}{P_1}\right)^2} \tag{5-5}$$

Recalling the tube-load model in the previous chapter, consider the arterial tree approximated into lumped upper body and lower body circulations that are connected in parallel. For the sake of the BCG force estimation, the BP and BF wave in the lower body circulation must be calculated. The lower body circulation is modeled as a uniform lossless tube with a type I load as shown in Fig. 4-2 in the previous chapter. It is assumed that a constant fraction of the cardiac output, shown by K_d, flows through the lower body circulation.

In this model, C is the load compliance and R is the resistance associated with peripheral arteries in the lower body. Z_c is the aortic characteristic impedance and can be expressed as

$$Z_C(MAP) = \sqrt{\frac{\rho}{A_D(MAP)C'(MAP)}} \tag{5-6}$$

Where, ρ is the blood density. The load compliance in this model is constant and the load resistance, R, is computed via Eq. (5-7).

$$R = TPR/K_d - Z_c \tag{5-7}$$

The transfer function ($Z_a(j\omega)$), input impedance, relating the central aortic pressure waveform ($P_A(j\omega)$) to the central aortic flow waveform ($Q_A(j\omega)$) in the frequency domain, is given below [23].

$$Q_A(j\omega) = Z_a(j\omega)P_A(j\omega) = \frac{1}{Z_c}\frac{e^{j\omega T} - \Gamma(j\omega)e^{-j\omega T}}{e^{j\omega T} + \Gamma(j\omega)e^{-j\omega T}}P_A(j\omega) \tag{5-8}$$

in which T is the pulse transit time (PTT) between the central aorta and peripheral artery (PTT in Fig. 4-2).

$$T = d \times \sqrt{\frac{\rho \times C'(MAP)}{A_D(MAP)}} \tag{5-9}$$

and d is the tube length. Recalling the equation for reflection coefficient for a type I load as

$$\Gamma(j\omega) = \frac{R}{R + 2Z_c + 2j\omega Z_c RC} \tag{5-10}$$

Therefore, the input impedance, $Z_a(j\omega)$, for this model is:

$$Z_a(j\omega) = \frac{P_A(j\omega)}{Q_A(j\omega)} = Z_c \frac{e^{j\omega\tau_D} + \frac{R}{R + 2Z_c + 2j\omega Z_c RC} e^{-j\omega\tau_D}}{e^{j\omega\tau_D} - \frac{R}{R + 2Z_c + 2j\omega Z_c RC} e^{-j\omega\tau_D}}$$

$$= Z_c \frac{(R + 2Z_c + 2j\omega Z_c RC)e^{j\omega\tau_D} + Re^{-j\omega\tau_D}}{(R + 2Z_c + 2j\omega Z_c RC)e^{j\omega\tau_D} - Re^{-j\omega\tau_D}} \tag{5-11}$$

$$= Z_c \frac{\left(\frac{1}{2Z_cC} + \frac{1}{RC} + j\omega\right) e^{j\omega\tau_D} + \frac{1}{2Z_cC} e^{-j\omega\tau_D}}{\left(\frac{1}{2Z_cC} + \frac{1}{RC} + j\omega\right) e^{j\omega\tau_D} - \frac{1}{2Z_cC} e^{-j\omega\tau_D}}$$

Having the input impedance, $Z_a(j\omega)$, from Eq. (5-11), the BP waveform at the aortic inlet, $P_0(j\omega)$, in the frequency domain can be estimated from the BF harmonics.

$$P_0(j\omega) = Z_a(j\omega)Q_0(j\omega) \tag{5-12}$$

Also, the time domain BP wave, $P_0(t)$, is computed by applying the inverse Fourier transform to the harmonics $P_0(j\omega)$.

Finally, by substituting $s = j\omega$, and $P_0(s)$ in Eq. (5-12) into the following closed-form BCG model rewritten from chapter 4,

$$
\begin{aligned}
F_{BCG}(s) &= A_D\big(P_1(s) - P_2(s)\big) - A_A\big(P_0(s) - P_1(s)\big) \\
&= A_D\big(G_{10}P_0(s) - G_{20}P_0(s)\big) - A_A\big(P_0(s) - G_{10}(s)P_0(s)\big) \\
&= \Big(A_D\big(G_{10}(s) - G_{20}(s)\big) - A_A\big(1 - G_{10}(s)\big)\Big)\, P_0(s) \\
&= \left(A_D \left(e^{-\tau_A s} - \frac{\frac{1}{Z_c C} + \frac{1}{RC} + s}{\left(\frac{1}{2Z_c C} + \frac{1}{RC} + s\right) e^{s\tau_D} + \frac{1}{2CZ_C} e^{-s\tau_D}} \right) \right. \qquad (5\text{-}13) \\
&\quad \left. - A_A\left(1 - e^{-\tau_A s}\right) \right) P_0(s) = H(s)P_0(s)
\end{aligned}
$$

a transfer function is obtained that estimates BCG from a BF wave, $Q_0(s)$. Fig. 5-3 shows the flowchart of the transfer function resulting from this integration.

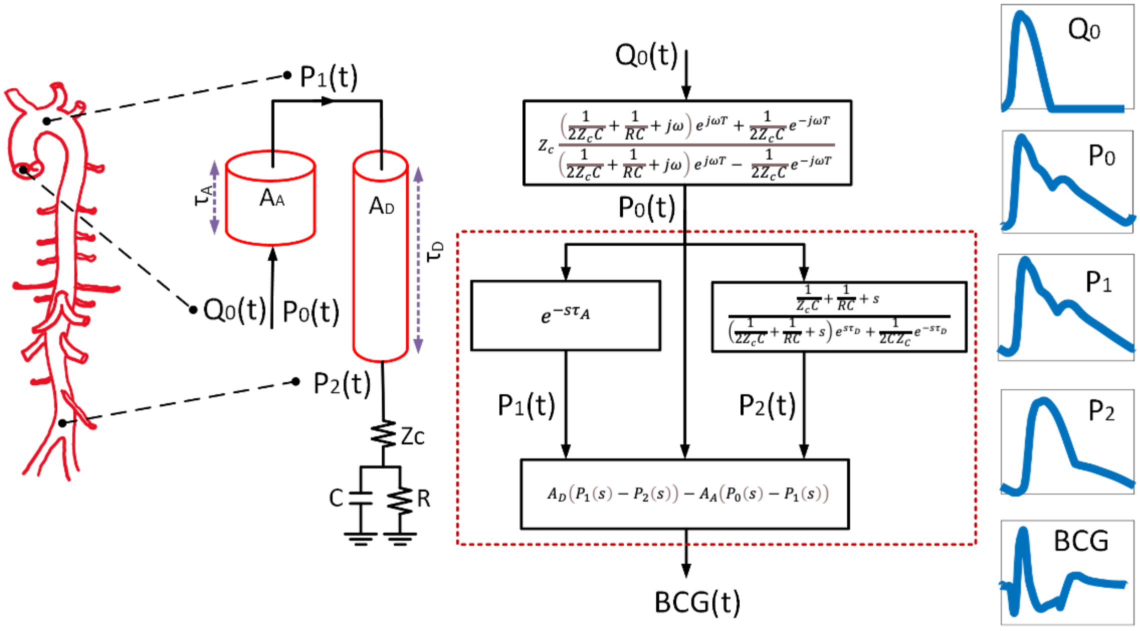

Fig. 5-3: An extended model with flow waveform as the input and BCG waveform as the output

The mathematical model estimating BCG from $Q_0(s)$ is as below

$$\begin{aligned}
F_{BCG}(s) &= A_D\big(P_1(s) - P_2(s)\big) - A_A\big(P_0(s) - P_1(s)\big) = H(s)Z_a(s)Q_0(s) \\
&= \left(A_D \left(e^{-\tau_A s} - \frac{\frac{1}{Z_c C} + \frac{1}{RC} + s}{\left(\frac{1}{2Z_c C} + \frac{1}{RC} + s\right) e^{s\tau_D} + \frac{1}{2CZ_C} e^{-s\tau_D}} \right) \right. \\
&\qquad \left. - A_A\left(1 - e^{-\tau_A s}\right) \right) Z_c \frac{\left(\frac{1}{2Z_c C} + \frac{1}{RC} + s\right) e^{s\tau_D} + \frac{1}{2Z_c C} e^{-s\tau_D}}{\left(\frac{1}{2Z_c C} + \frac{1}{RC} + s\right) e^{s\tau_D} - \frac{1}{2Z_c C} e^{-s\tau_D}} Q_0(s) \\
&= G(s)Q_0(s)
\end{aligned} \tag{5-14}$$

This model has 6 independent internal parameters: T, τ_A, $Z_c C$, RC, A_A, and A_D. The value of load compliance, C, is constant and set based on the values suggested in the literature [112], [113]. Having the four inputs to the model (i.e., age, HR, SV, and TPR) the rest of the model parameters are found by the empirical and physical relationships that are described previously in this chapter. In sum, the BCG is predicted as depicted in Fig. 5-4, according to the following steps:

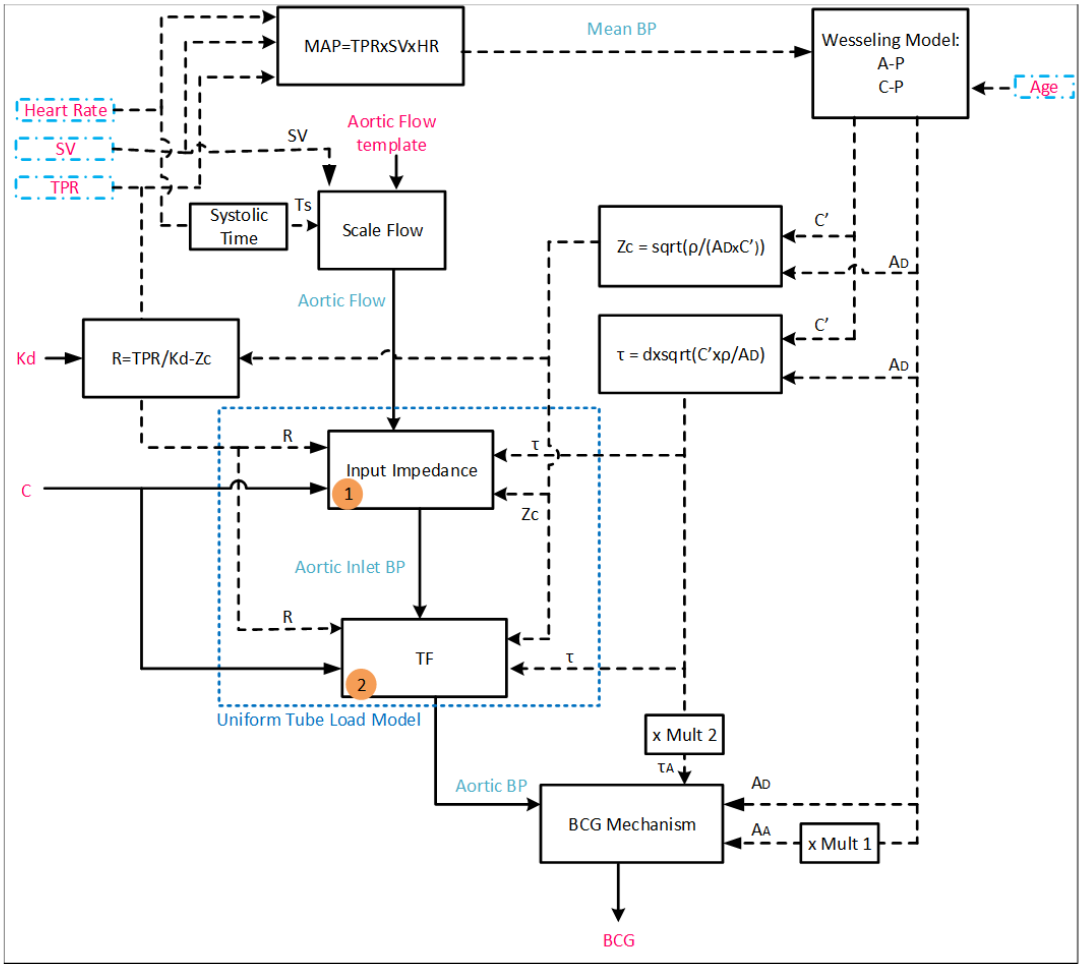

Fig. 5-4: Flow chart of the model which gets four inputs: age, HR, SV, and TPR and estimates BCG waveform

1) For a specific cardiovascular state scenario, the age input is used in conjunction with HR, SV, and TPR (which yields mean arterial blood pressure (BP)) to compute the arterial cross-sectional and compliance per unit length.

2) The arterial compliance per unit length is used to compute the arterial characteristic impedance and pulse transit time (PTT).

3) The arterial characteristic impedance is used in conjunction with TPR to compute the arterial terminal resistance.

4) HR is used to compute the left ventricular ejection time (LVET). Then, the heart blood flow is shaped using LVET, SV, and a normalized flow waveform template.

5) The parameters computed above are used to derive the aortic input impedance function. Then, the heart blood flow is inputted to the aortic input impedance function to compute the aortic inlet BP.

6) The parameters computed above are likewise used to characterize the transfer function between the aortic inlet BP and aortic outlet BP. Then, the aortic inlet BP is inputted to the transfer function to compute the aortic outlet BP. The aortic inlet BP is likewise used to calculate the aortic arch BP.

7) The aortic inlet, aortic arch, and aortic outlet BPs are inputted to the BCG mechanism model to compute the BCG waveform.

5.3. Experimental Data

Experimental data from prior work was used [108]. Data from 17 young healthy subjects (age 25±5 years old; gender 12 male and 5 female; height 174±10 cm; weight 74±17 kg) under the approval of the University of Maryland Institutional Review Board (IRB) was collected. For the sake of this study, the following physiological signals were used: (i) an ECG acquired using 3-gel electrodes in the Lead II configuration and interfaced with a wireless amplifier (BN-EL50, Biopac Systems, Goleta, CA, USA); (ii) a whole body BCG was instrumented using a strain gauge embedded in a customized weighing scale (BC534, Tanita, Tokyo, Japan) (iii) a PPG signal which was instrumented using a finger clip sensor (8000AA, Nonin Medical, Plymouth, MN, USA); and (iv) a reference BP pulse acquired using a fast servo-controlled finger cuff embedded with a PPG sensor on the ring finger of a hand, which was height-compensated and transformed to brachial BP pulse (ccNexfin, Edwards Lifesciences, Irvine, CA, USA). These signals were acquired at a sampling rate of 1KHz during four BP perturbing interventions (including cold pressor (CP), mental arithmetic (MA), slow breathing (SB), and breath-holding (BH)) and 5 resting periods (R1, R2, R3, R4, and R5) in between them while the participants stood still.

In each subject, the data was divided into 9 periods, R1, CP, R2, MA, R3, SB, R4, BH, and R5. Then, the fiducial points required to investigate the efficacy of the model-based feature selection method were extracted. The details of the feature extraction can be found in [114]. In brief, after band-pass filtering, the BCG and PGG signals were gated using the ECG R waves as the reference. The low-quality beats were removed. Then the BCG was smoothed using a 10-order exponential moving average. The features in BCG including the I, J, and K waves were extracted as described in [114]. Three wave-to-wave timing (I-J T, I-K T, J-K T) and two wave-to-wave amplitudes (I-J A, J-K A) were constructed from these features. The reference DP and SP were also extracted from the BP pulse beats as the minimum and maximum in the waveform. PP was computed as the difference between SP and DP (PP=SP-DP). PTT was computed as the time interval between the PPG foot and the J wave in the BCG. SV and TPR were recorded in the experiment. The data were analyzed in the following steps. First, the outliers in the extracted characteristic features were identified and removed. Second, the sample size of the characteristic features was increased using the bootstrap technique. Third, univariate linear regression analysis was conducted at the individual level to find the correlations between each BCG feature and each CV parameter. Fourth, the median of the bootstrapped features was computed for each period and was used for the construction of PTT-PWA models.

5.4. Model-Based BCG Feature Selection

The mathematical model was used to study the impact of different CV risk predictors and parameters (i.e., SP, PP, DP, SV, and HR) on the morphology of the BCG waveform (Fig. 5-5).

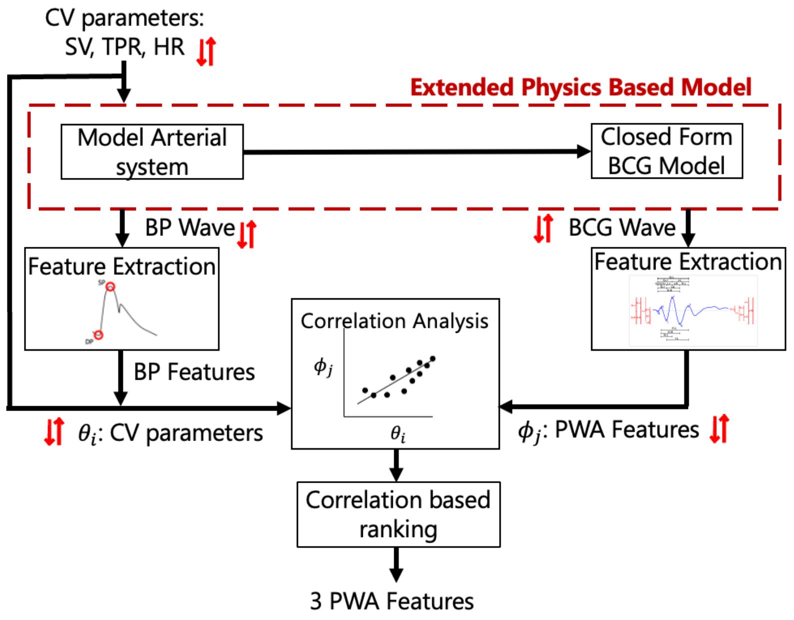

Fig. 5-5 Flow chart of systematic selection of the BCG features for cardiovascular parameter tracking

Different CV situations can be simulated by alteration in the model inputs. Random Perturbations up to +/-50% of the SV, HR, and MAP were implemented, and these values were entered into the model which resulted in alterations in internal BP waves and consequently the output BCG wave. Some of the perturbations resulted in unrealistically low or high SP and DP values which were excluded based on the following criteria: the waves associated with DP<50 [mmHg] and/or SP>200 [mmHg] were excluded from the results. From the BCG waveform associated with each eligible SV-TPR-HR combination, fiducial points of I, J, K, L, M, and N waves were extracted and a total of 36 features were constructed: 15 wave-to-wave intervals (I-J, I-K, I-L, I-M, I-N, J-

K, J-L, J-M, J-N, K-L, K-M, K-N, L-M, L-N, M-N) and 21 wave/wave-to-wave amplitudes (I, J, K, L, M, N, I-J, I-K, I-L, I-M, I-N, J-K, J-L, J-M, J-N, K-L, K-M, K-N, L-M, L-N, M-N). Then, the relationship between these features versus SV, HR, TPR, SP, DP, PP, and MAP were assessed using the univariate correlation analysis.

5.5. Efficacy of the Model-Based Feature Selection in BP Tracking

To determine the efficacy of the model-based feature selection technique, its performance was investigated in tracking SP and DP which are two important CV risk predictors. Two common approaches in cuffless DP and SP tracking are PTT and pulse wave analysis (PWA). In addition, a technique based on the fusion of the two approaches is on the rise and has demonstrated potential to track DP and SP [85].

To show the efficacy of model-based BCG feature selection, a comparative study between three models was performed to investigate their DP and SP tracking performance. The first model was based on the famous PTT technique for cuffless BP monitoring. The second and third models were based on the PTT, PWA fusion technique. In the second model, a small subset of BCG features (i.e., three features) that proved most sensitive to BP based on the model-based analysis were used. In the third model, all experimentally available BCG features were included. In the two latter models, a technique developed in [115] was used to aggregate all BCG features into a single predictor of BP which is orthogonal to PTT. In the end, the efficacy of the three models (PTT, model-based PTT-PWA fusion, and brute-force PTT-PWA fusion) was evaluated and compared using the experimental scale BCG and BP data collected from 17 human subjects.

5.5.1 Construction of BP Predictor Orthogonal to PTT

As mentioned above, this technique is adopted from a prior work to reduce the dimensionality of BCG features used for BP tracking [115]. First, the BP, PTT, and PWA features associated with each subject were normalized using their respective mean values on a subject-by-subject basis to reduce the adverse effect of inter-subject variability in the features.

$$\tilde{P}_D^{(i)} = \frac{P_D^{(i)} - \bar{P}_D^{(i)}}{\bar{P}_D^{(i)}}, \quad \tilde{P}_S^{(i)} = \frac{P_S^{(i)} - \bar{P}_S^{(i)}}{\bar{P}_S^{(i)}} \tag{5-15}$$

$$\tilde{\tau}^{(i)} = \frac{\tau^{(i)} - \bar{\tau}^{(i)}}{\bar{\tau}^{(i)}}, \quad \tilde{\phi}_k^{(i)} = \frac{\phi_k^{(i)} - \bar{\phi}_k^{(i)}}{\bar{\phi}_k^{(i)}} \tag{5-16}$$

Where $P_D^{(i)}$ and $P_S^{(i)}$ are the DP and SP vectors, $\tau^{(i)}$ is the PTT vector and $\phi_k^{(i)}$ is the k-th PWA feature vector, all associated with the i-th subject (i = 1, 2, …, N=17). $\tilde{P}_D^{(i)}$, $\tilde{P}_S^{(i)}$, $\tilde{\tau}^{(i)}$, and $\tilde{\phi}_k^{(i)}$ are the normalized DP, SP, PTT, and k-th feature vectors; and $\bar{P}_D^{(i)}$, $\bar{P}_S^{(i)}$, $\bar{\tau}^{(i)}$, and $\bar{\phi}_k^{(i)}$are the mean DP, SP, PTT and k-th feature vectors all associated with the i-th subject. Second, the normalized reference BP, PTT, and PWA features pertaining to individual subjects were aggregated into the following BP, PTT, and PWA feature vectors.

$$P_D \triangleq \begin{bmatrix} \tilde{P}_D^{(1)} \\ \vdots \\ \tilde{P}_D^{(N)} \end{bmatrix}, \quad P_S \triangleq \begin{bmatrix} \tilde{P}_S^{(1)} \\ \vdots \\ \tilde{P}_S^{(N)} \end{bmatrix} \tag{5-17}$$

$$\tau \triangleq \begin{bmatrix} \tilde{\tau}^{(1)} \\ \vdots \\ \tilde{\tau}^{(N)} \end{bmatrix}, \quad \phi \triangleq \begin{bmatrix} \tilde{\phi}_1^{\ (1)} & & \tilde{\phi}_M^{\ (1)} \\ \vdots & \cdots & \vdots \\ \tilde{\phi}_1^{\ (N)} & & \tilde{\phi}_M^{\ (N)} \end{bmatrix} \tag{5-18}$$

Third, BP was decoupled into two components: the component of BP explainable by PTT and the orthogonal component of BP which is not explainable by PTT. This was done by projecting BP to PTT and subtracting it from BP.

$$P_X^{\perp} \triangleq P_X - \frac{P_X^T \tau}{\tau^T \tau}\tau \tag{5-19}$$

Where $P_X^{\perp}$, $X = D, S$, is the component of BP orthogonal to PTT. Fourth, two predictors of BP were derived (each pertaining to DP and SP) according to [115] by aggregating the PWA features of interest to maximize the covariance between $P_X^{\perp}$ and PWA features and a vector v was computed that provides the weights for the PWA features.

$$\psi_X = \sum_{k=1}^{M} v(k)\phi(k) \tag{5-20}$$

Where, $v(k)$ is the k-th element of v and $\phi(k)$ is the k-th PWA feature. In this way, ψ_D and ψ_S are computed which are the population-averaged predictors of BP.

5.5.2 BP Trend Monitoring Performance Evaluation

The efficacy of scale BCG-based PTT-PWA fusion compared to PTT was evaluated using the experimental data. The goals were to (i) assess the potential of model-based analysis in selecting effective features for BP trend tracking and (ii) compare the performance of the PTT-PWA fusion with PTT.

To assess the potential of model-based BCG feature selection for BP trend tracking, two PTT-PWA fusion models were compared. Linear regression models were constructed that related normalized PTT and BP predictors derived in the previous section to normalized reference BP on an individual basis, using the experimental data

$$\tilde{P}_X^{(i)} = k_{X,1}^{(i)}\tilde{\tau}^{(i)} + k_{X,2}^{(i)}[\tilde{\phi}_1^{(i)} \quad \dots \quad \tilde{\phi}_M^{(i)}]v + k_{X,3}^{(i)} \tag{5-21}$$

Where, $k_{X,1}^{(i)}$, $k_{X,2}^{(i)}$, $k_{X,3}^{(i)}$, $X = D, S$, are the coefficients pertaining to the i-th subject that can be determined using the least square method. The first PTT-PWA fusion model (named model-based PTT-PWA) was based on the subset of PWA features selected by the model-based analysis (M = 3) and the second PTT-PWA fusion model (named brute-force PTT-PWA) was constructed from all the 8 experimentally available BCG features (M = 8). Once the linear regression models were obtained, the PTT ($\tilde{\tau}^{(i)}$) and PWA features ($[\tilde{\phi}_1^{(i)} \quad \dots \quad \tilde{\phi}_M^{(i)}]$) were plugged into the regression models to predict $\tilde{P}_X^{(i)}$, and the actual BP, $P_X^{(i)}$ was estimated using Eq. (5-15):

$$P_X^{(i)} = \bar{P}_X^{(i)}\tilde{P}_X^{(i)} + \bar{P}_X^{(i)} \tag{5-22}$$

PTT-PWA fusion models were evaluated and compared based on the 4 error metrics: (i) correlation coefficient, (ii) root-mean-squared error (RMSE), (iii) precision, and (iv) mean absolute error (MAE) between reference BP and BP estimated by the regression models in Eq. (5-21) and Eq. (5-22). The aforementioned evaluation procedure was performed on each BP level (DP and SP) subject specifically and performance metrics were aggregated across all subjects to derive statistics associated with each BP level.

In addition, to comparatively evaluate PTT-PWA fusion with PTT, a regression model for the case of PTT was developed. To do so, $k_{X,2}^{(i)}$ was set to 0 in Eq. (5-21) and $k_{X,1}^{(i)}$ and $k_{X,3}^{(i)}$ were determined. Then, as described above the 4 error metrics were evaluated for the PTT model as well.

Statistical tests were performed to compare the efficacy of the regression models for BP trend monitoring. Model-based PTT-PWA fusion and brute-force PTT-PWA fusion were compared by performing paired t-tests on the 4 error metrics. The intention of this comparison was to demonstrate the validity and effectiveness of the model-based analysis approach in systematically narrowing down the feature set to those important for BP tracking. In addition, the efficacy of PTT and model-based PTT-PWA fusion were compared using another paired t-test. The intention of this comparison was to show the potential value of scale BCG-based PTT-PWA fusion on top of PTT.

5.6. Results

Table 5-1 summarizes the correlation coefficients of the model-based BCG features associated with all the features commonly found in the experimental dataset. Table 5-2 summarizes the correlation coefficients associated with the univariate correlation analysis on the experimental data. Both tables show results of ranking the features based on the correlation coefficients in descending order. Table 5-3 summarizes the performance of scale BCG PTT, PTT-PWA fusion based on 3 features selected using the model-based analysis, and PTT-PWA fusion based on all the 8 features in tracking BP trend. The performance of the models was reported in terms of correlation coefficient (r), RMSE, precision, and MAE.

Table 5-1: Correlation coefficients between individual model-based BCG features versus peripheral CV parameters (colors indicate the three highest-ranked features in the experimental data, blue: ranked 1st, cyan: ranked 2nd, pink: ranked 3rd)

RANK	**SP**	**r**	**DP**	**r**	**PP**	**r**	**SV**	**r**	**TPR**	**r**
1	I-K T	0.95	I-K T	0.95	J A	0.81	J-K A	0.66	I A	0.93
2	J-K T	0.94	J-K T	0.94	J-K A	0.65	K A	0.56	K A	0.81
3	I-J T	0.93	I-J T	0.93	I-J A	0.62	I-J A	0.56	I-J A	0.74
4	J A	0.61	K A	0.82	J-K T	0.58	J A	0.50	J-K A	0.74
5	K A	0.55	I A	0.53	I-K T	0.56	I A	0.48	J-K T	0.52
6	I-J A	0.26	J A	0.21	I-J T	0.51	I-J T	0.07	I-K T	0.47
7	J-K A	0.20	J-K A	0.00	I A	0.14	I-K T	0.00	J A	0.47
8	I A	0.18	I-J A	0.00	K A	0.00	J-K T	0.00	I-J T	0.36

Table 5-2: Correlation coefficients between individual BCG features versus peripheral CV parameters calculated from univariate regression applied to the experimental data (colors indicate the three highest-ranked features in the experimental data, blue: ranked 1st, cyan: ranked 2nd, pink: ranked 3rd)

RANK	**SP**	**r**	**DP**	**r**	**PP**	**r**	**SV**	**r**	**TPR**	**r**
1	I-K T	0.32	I-K T	0.44	J-K A	0.54	J A	0.50	J-K T	0.29
2	K A	0.31	J-K T	0.39	I-J A	0.53	J-K A	0.46	I-K T	0.26
3	J-K T	0.30	I-J T	0.27	J A	0.53	I-J A	0.46	K A	0.12
4	J-K A	0.26	K A	0.09	K A	0.51	K A	0.39	J-K A	0.12
5	I-J T	0.22	I A	0.08	I A	0.46	I A	0.26	I A	0.11
6	J A	0.20	J-K A	0.06	I-K T	0.23	I-J T	0.17	I-J T	0.09
7	I-J A	0.18	J A	0.04	I-J T	0.21	I-K T	0.09	J A	0.07
8	I A	0.11	I-J A	0.01	J-K T	0.14	J-K T	0.05	I-J A	0.01

To assess the validity of the BCG features predicted to have a high correlation with SP, DP, PP, SV, and TPR, these BCG features were compared to the BCG features that exhibited high correlations to SP, DP, PP, SV, and TPR in the experimental dataset. The dataset only included a subset of the BCG features (I-J T, I-K T, J-K T, I A, J A, K A, I-J A, and J-K A). We found that (i) concerning SP, 2 out of the top 3 BCG features (associated with the 3 highest correlation coefficients) were identical (I-K T and J-K T), (ii) with regard to DP, the top 3 BCG features (associated with the 3 highest correlation coefficients) were identical (I-K T, I-J T, and J-K T), (iii) with regard to PP, the top 3 BCG features (associated with the 3 highest correlation coefficients) were identical (J A, I-J A, and J-K A), (iv) with regard to SV, 2 out of the top 3 BCG features (associated with the 3 highest correlation coefficients) were identical (J-K A and I-J A), and (v) with regard to TPR, 1 out of the top 3 amplitude BCG features (associated with the 3 highest correlation coefficients) was identical (K A), both between model prediction and experimental dataset.

*Table 5-3: Correlation coefficients(r), Root-mean-squared errors (RMSE), precision, and mean absolute errors (MAE) associated with scale BCG-based PTT, model-based PTT-PWA, and brute-force PTT-PWA fusion in cuffless BP trend tracking. *: significantly different relative to model PTT-PWA (paired t-test, P<0.05)*

DP	PTT	model PTT-PWA	Brute-Force PTT-PWA
r	0.60*	0.74	0.75
RMSE [mmHg]	11.15*	9.28	8.98
Precision [mmHg]	11.85*	9.92	9.73
MAE [mmHg]	9.13*	7.75	7.44

The model-based PTT-PWA fusion achieved significant improvement in tracking BP trends relative to scale BCG PTT, in terms of all four metrics. Comparing the error metrics and correlation coefficients associated with the model-based PTT-PWA and brute-force PTT-PWA fusion showed that there was no significant difference between the two models.

5.7. Discussion

The current gold standard waveform for detecting CV parameters and risk predictors is the central BP wave. However, its acquisition is challenging. On the other hand, BCG is amenable to convenient instrumentation. Therefore, understanding the association between CV parameters and BCG is useful for the development of novel ultra-convenient techniques for CV health monitoring. In this chapter an extended physiological model was developed that can be leveraged to find the BCG features which respond to changes in CV parameters. This model was used for the systematic selection of scale BCG PWA features based on model-based sensitivity analysis. Investigation using experimental data demonstrated the effectiveness of the model-based systematic method in the selection of BCG features most sensitive to perturbations in CV parameters and in BP trend tracking.

5.7.1 Model-Based BCG Feature Selection

Comparisons between model-based and experimental data rankings to find most sensitive BCG features to changes in CV parameters showed a high degree of similarity. In fact, in 4 out of 5 CV parameters (DP, SP, PP, and SV) at least 2 out of 3 highest ranked features were similar which suggests the validity of the model-based sensitivity analysis developed in this chapter.

5.7.2 BP Trend Monitoring

Given the fact that the improvement achieved by fusing PWA to PTT was moderate, it is concluded that PTT may play the primary role in tracking BP trends. However, PWA offers meaningful complementary value in that PWA-based BP predictors were orthogonal to PTT and significantly improved all four metrics.

Comparing the performance metrics associated with the model-based PTT-PWA fusion and the brute-force PTT-PWA fusion showed the power of systematic PWA feature selection. In fact, there were no significant differences between the two models in both DP and SP cases, which suggested that model-based sensitivity analysis was effective in reducing the set of PWA features required for BP trend tracking by excluding non-essential PWA features.

5.8. Conclusions

In this chapter, leveraging the closed-form BCG model, an extended mathematical model was developed which allowed for the investigation of the effect of the changes in the CV state on the morphology of the BCG waveform. Thus, this mathematical model can serve as a systematic tool to elucidate the relationship between the CV risk predictors and the BCG. In addition, by perturbing the CV variables that were inputs of the model, the relationship between the features in the BCG waveform and various CV risk predictors was studied. The BCG features deemed sensitive to changes in CV parameters were used in tracking the BP trend. The advantage of selecting the features based on the sensitivity analysis using the model was that the set of chosen features is generalizable to different data sets, therefore, this method has the potential to facilitate ubiquitous BP trend tracking.

Chapter 6: BCG Recording

6.1. Introduction

A prior work has developed a mathematical model elucidating the mechanism underlying the genesis of BCG [22]. This work hypothesized that the heart-induced force acting on the body (force BCG) results from the arterial BP gradients in the ascending and descending aorta. This finding indicated that the morphology of the BGC waveform has a close association with the underlying aortic BP waveforms. However, this hypothesis still needs to be validated. There are two challenges in the way of this model validation. First, the model needs to be validated in different hemodynamic states using simultaneous recordings of BCG and three BP waveforms. In addition, the BP waveforms need to be captured invasively, from three different locations in the aorta. Therefore, an invasive animal study should be performed in which BP measurement sensors can be placed inside an animal's arteries to measure BP. Second, BCG waveforms recorded with different sensors and different devices have morphological differences [30]. Therefore, the relationship between the force BCG and the BCG measured by various instruments may differ substantially. Consequently, a measurement technique must be developed to capture the heart-induced body movements that has the closest affinity with the "true BCG" (i.e. output of the BCG mechanism model).

To address these challenges, the aim of this chapter was to develop and construct a BCG recording apparatus that can capture the closest BCG morphology to the "true BCG". This BCG recording apparatus should be able to accommodate measurements in humans as well as large animals (such as pigs).

6.2. BCG Instrumentation Apparatus

The purpose of the BCG recording apparatus is to measure the movements of the body resulting from the heartbeat. Various designs and measurement sensors have been proposed for BCG measurements. Most of these methods record one of the four quantities: force, acceleration, velocity, or displacement [116]. It is necessary to make a careful study to answer the following questions:

1. What quantity is being measured with the BCG instrument?
2. What are the physical requirements for the device that would result in a reasonably reliable record of the “true BCG”?

Let’s start with the definition of the so-called “true” BCG. As mentioned earlier the goal of the BCG recording device is to measure the heart-induced body movements. Assume a person floating in free space and in the absence of respiration. The law of conservation of momentum dictates that throughout one cardiac cycle, the body will not acquire any net momentum as a result of the heartbeat. If the measurement of the body movements could be made under such ideal circumstances, they would represent the “true” BCG. In practice, usually, there is a binding between the subject and the environment. The addition of these bindings alters the shape of the recordings of BCG. Therefore, the BCG morphology depends on the dynamics of the recording device, the body, and the binding between the two [117], [100].

In this work, multiple candidates of the BCG measurement devices were considered that may result in recordings close to the true BCG:

(i) an accelerometer directly attached to the body;

(ii) a sliding bed (with air bearings)

(iii) Ultra-Low Frequency (ULF) BCG (hanging bed)

The three designs were compared based on the following factors: (1) cost, (2) their demonstrated ability to measure true BCG in the literature, and (3) their convenience for invasive measurement of BCG in pigs. Since the sliding bed requires the use of costly air bearings and high precision manufacturing and there were not many studies on the BCG recorded using such a setup it was excluded from the study. In the end, designs (i) and (iii) were selected for fabrication and their effectiveness in BCG measurement was investigated in animal and human experiments. Details follow.

6.3. The Physical Basis of the Apparatus for BCG Recording

The purpose of this section is to investigate the physical properties of the two BCG recording devices mentioned above. To represent the two designs considered in this study, the following simple mechanical system is introduced and analyzed (Fig. 6-1). Depending on the assumptions on the binding between the instrument and the ground the following mechanical model can represent the direct body accelerometer or the ULF BCG bed.

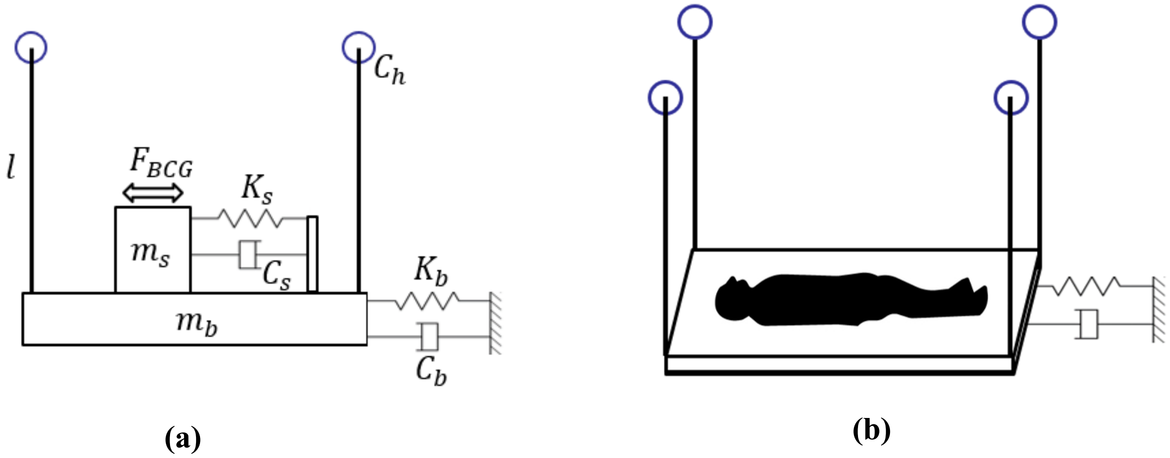

Fig. 6-1: Schematic representation of the BCG recording system. (a) The BCG is shown as a force inserted on the subject by the heart. The couplings between the subject and the BCG device and the device and the surrounding are

shown. (b) The BCG setup is shown as a bed hanging from the ceiling using four cables loaded with a subject. A spring and damper provide additional coupling between the BCG bed and the surrounding.

In this system, the subject with the mass m_s is represented by a cart that is coupled to the BCG apparatus by a spring and frictional force. The BCG apparatus is represented by a platform (i.e., bed) suspended from the ceiling using four cables. The BCG bed has a mass of m_b. The system of subject and BCG is coupled to the surrounding in the same way. From this system, the dynamical equations governing the motion of the subject and BCG are as follows:

$$m_s\ddot{x_s} + C_s(\dot{x}_s - \dot{x}_b) + K_s(x_s - x_b) = F_{bcg} \tag{6-1}$$

$$m_b\ddot{x_b} + C_s(\dot{x}_b - \dot{x}_s) + K_s(x_b - x_s) + C_a\dot{x}_b + k_a x_b = 0 \tag{6-2}$$

Where, x_s, $\dot{x}_s$, and $\ddot{x_s}$ are the displacement, velocity, and acceleration of the body with respect to a fixed reference. Similarly, x_b, $\dot{x}_b$, and $\ddot{x}_b$ are the displacement, velocity, and acceleration of the BCG device with respect to a fixed reference. K_s and C_s are the spring and damper constants that represent the binding between the body and BCG bed (skin, cloths, and straps). The coupling between the BCG bed and the surrounding is defined using the following spring (K_a) and damper constants (C_a)

$$\begin{gathered} K_a = K_b + \frac{mg}{l} \\ C_a = C_b + C_h \end{gathered} \tag{6-3}$$

Where, K_b and C_b are the spring and damper constants that provide an additional connection between the bed of the BCG device and the surrounding. Rewriting Eq. (6-1) and Eq. (6-2) in the Laplace domain the following transfer function is obtained to describe the relationship between the displacement of the body and the BCG force generated by the heart.

$$\frac{X_s}{F_{bcg}} = \frac{m_b s^2 + (C_s + C_a)s + K_a + K_s}{m_s m_b s^4 + (m_s C_s + m_b C_s + m_s C_a)s^3 + (C_a C_s + m_s k_s + m_b K_s + K_a m_s)s^2 + (K_a C_s + C_a K_s)s + K_a K_s} \tag{6-4}$$

Using Eq. (6-4) and different assumptions on the values of model parameters, we will make assessments about the nature of the quantity that is being measured by each of the two selected techniques of BCG instrumentation, which are: (1) An accelerometer on the body, (2) ULF BCG bed.

6.3.1 Accelerometer on the Body

In this case, the binding between the bed and the surrounding is infinitely large so the bed is practically fixed and does not move. To satisfy this assumption K_a must be ∞. This assumption would result in the following simplification in Eq. (6-4).

$$\frac{X_s}{F_{bcg}} = \frac{K_a}{(K_a m_s)s^2 + (K_a C_s)s + K_a K_s} = \frac{1}{m_s s^2 + C_s s + K_s} \tag{6-5}$$

In addition to the $K_a \to \infty$ assumption if we postulate that the binding between the body and the bed surface is strong (that can be accomplished by strapping the body to the bed) then $\frac{K_s}{m_s} \gg 1$. This means that in this method of BCG measurement, the mechanical system including the body and the BCG measurement device has a high natural frequency. In addition, we can reduce Eq. (6-5) to the following:

$$\frac{X_s}{F_{bcg}} \approx \frac{1}{K_s} \tag{6-6}$$

From the above equation, we can deduce that displacement recordings in such a setup would be proportional to the true BCG force generated by the heart.

6.3.2 ULF BCG Bed

In this case, the binding between the bed and the surrounding is infinitely small and finite $\frac{K_a}{m_s+m_b} \ll 1$. However, we will assume a rigid contact between the body and the bed which means that $K_s \to \infty$. This assumption would result in the following simplification in Eq. (6-4).

$$\frac{X_s}{F_{bcg}} = \frac{K_s}{(m_s k_s + m_b K_s)s^2 + (C_a K_s)s + K_a K_s} = \frac{1}{(m_s + m_b)s^2 + C_a s + K_a} \tag{6-7}$$

From the above equation and considering $\frac{K_a}{m_s+m_b} \ll 1$, we can simplify Eq. (6-7) further.

$$\frac{s^2 X_s}{F_{bcg}} \approx \frac{1}{(m_s + m_b)} \tag{6-8}$$

This shows that measurements of acceleration in the ULF BCG bed setup would be proportional to the true force BCG.

6.4. BCG Bed Design and Construction

This section explains the requirements and constraints for the design of the BCG recording apparatus. As explained in section 6.3.2, the optimal sensing method for the measurement of BCG in the ULF BCG bed is an accelerometer. Therefore, an acceleration form sensor (accelerometer) is selected that (i) can act as the direct body BCG measurement sensor, and (2) can be placed on the ULF BCG bed setup to measure the acceleration of the bed.

6.4.1 Requirements for the Accelerometer on the Body

Due to the three-dimensional nature of the BCG, the accelerometer should be able to record movement in three axes. The motion should be sensed by an accelerometer that can give an undistorted record of acceleration throughout the entire frequency spectrum of interest (approximately 1~40 Hz). In addition, the accelerometer must have a noise floor smaller than the amplitude of the BCG generated in pigs that will be used in the animal study. Therefore, selecting an accelerometer with a noise floor as low as possible is of great importance. According to prior experimental data, the amplitude of BCG acceleration in pigs is around 4 mg and in humans is around 10 mg. So, the selected accelerometer must have a noise floor at least 10 times smaller than these values in the frequency range of interest to reliably measure the BCG.

6.4.2 Requirements for the ULF BCG Bed

According to [68] the following factors should be considered for the design of ULF BCG bed:

1. The natural frequency of the system, which must be much lower than the important frequencies in the BCG signal to be measured.
2. The damping of the system, which can influence the natural frequency of the system and the ability of the BCG apparatus to restore its equilibrium in due time.
3. The relative motion between the body and the BCG.

The mentioned factors were interpreted into requirements for the elements in the BCG bed. The tunable elements in the design of the BCG bed are (1) the length of the suspension cable, (2) the weight of the suspended bed, and (3) damping. In addition, there were some external factors such as the dimensions of the storage space (the surgical room in which the invasive experiments would be performed) imposing some additional constraints on the design.

Cable length

Scarborough in [118] analyzed the frequency spectrum of the BCG that is of interest in the study of BCG and stated that most of the BCG information can be seen in the frequency range of 1 [Hz] to 40 [Hz]. These frequencies must be measured without distortion. Other studies also suggest upper limits for the natural frequency of the ULF BCG bed. For example, [119] suggested that the natural frequency of the BCG bed must be lower than 0.3 Hz. If we assume the ULF BCG bed setup as a simple pendulum with a natural frequency of

$$f = \frac{1}{2\pi} \times \sqrt{\frac{g}{l}} \tag{6-9}$$

Where, g is the gravitational acceleration constant and l is the length of the suspension cable. The constraint on the natural frequency determines the lower bound for the length of the suspension cables in the bed setup.

In addition, there are two spatial constraints to be considered in the choice of the bed height and subsequently the length of the cable. First, the BCG bed should move through door frames that have a standard height of 7 feet. Second, the maximum height of the external frame of the bed should not exceed the ceiling height which is 9 feet. To satisfy all the constraints on the cable length, the requirement on the natural frequency of the bed was relaxed to 0.4 Hz to accommodate for smaller cable heights. As shown in Fig. 6-2 using Eq. (6-9) the frequency of 0.4 is approximately associated with a cable length of 63 [in]. Therefore, $l > 63\ [in]$.

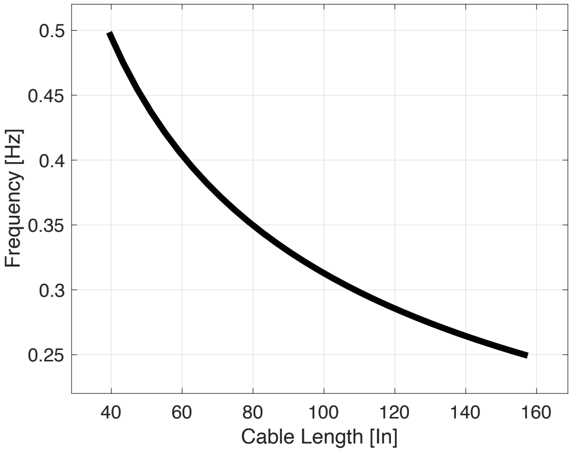

Fig. 6-2: Frequency of the BCG bed apparatus versus the length of the suspension cable

Bed mass

Since the BCG force generated by the heart is very small in magnitude, if the BCG bed is heavy the amplitude of movements becomes very small and may not be detectable. Therefore, another requirement is that the mass of the suspending part of the ULF BCG bed must be as low as possible. A higher limit of 22 [lb] was selected for the mass of the moving part of the bed per prior works in the literature.

Damping

In [120] burger explained the necessity of the existence of damping for the ULF BCG bed. They suggested the optimal damping for the system must be chosen in a way that there is a 25 percent overshoot. To achieve this amount of overshoot, the damping must be adjusted for each subject separately. Therefore, there is a need for an adjustable damping system. Therefore, a damping system in the following form is designed based on [116] in which a horizontal plate is floated in a box of treacle and attached to the suspended part of the bed. The value of damping can be adjusted by changing the distance between the horizontal plate and the bottom of the box (Fig. 6-3).

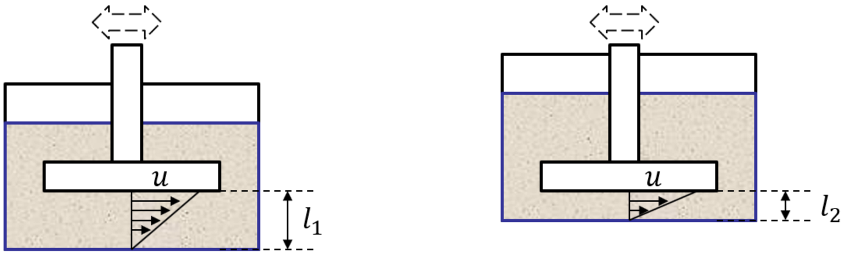

Fig. 6-3: The adjustable damping system. By adjusting the distance between the plate and the bottom of the box (l_1 and l_2) velocity gradient changes which results in a change in the shear forces acting upon the moving plate

The change in the distance changes the velocity gradient in the equation of shear force, τ.

$$\tau = \mu \frac{du}{dy} \tag{6-10}$$

Where, y is the displacement in the vertical direction and u is the flow velocity.

6.5. The Initial Design of the ULF BCG Bed

A moving bed is suspended from a custom-built rigid external frame of $31 \times 78 \times 78$ $[in^3]$. The height of the external frame was chosen to be 78 [in] since the bed needs to be transportable and fit through the door frames. The suspended bed must have a mass of less than 22 lb. Fig. 6-4 shows the initial design for the BCG bed setup. Two different designs were considered for the measurement of BCG in human and animal subjects. A flat plate was used as the platform for the human subject to lie upon. Since the animal must lie on its back for the surgical procedure, a trough-shaped platform was used to keep the animal fixed on the bed.

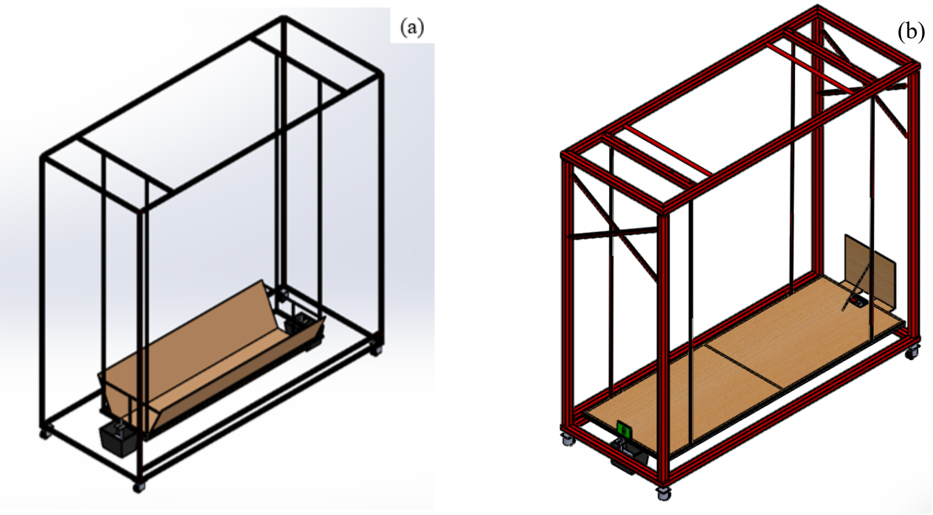

Fig. 6-4: Drawing of the initial ULF BCG bed for animal and human study. (a) Animal bed. (b) Human bed.

6.6. Construction of the BCG Bed and Design Iterations

Based on the initial design, a BCG bed apparatus was constructed and tested on human subjects (Fig. 6-5). The external frame was built using a welding technique to increase the rigidity of the frame and avoid any motion noise due to the vibration of the external frame.

Fig. 6-5: Initial ULF BCG bed constructed for recording data in human

The experimental procedure is described in 6.8. The recordings from this trial experiment were not satisfactory in the sense that the periodic BCG morphology was hardly detectable in the captured data. This resulted in implementing some improvements in the design (Fig. 6-6 (a)).

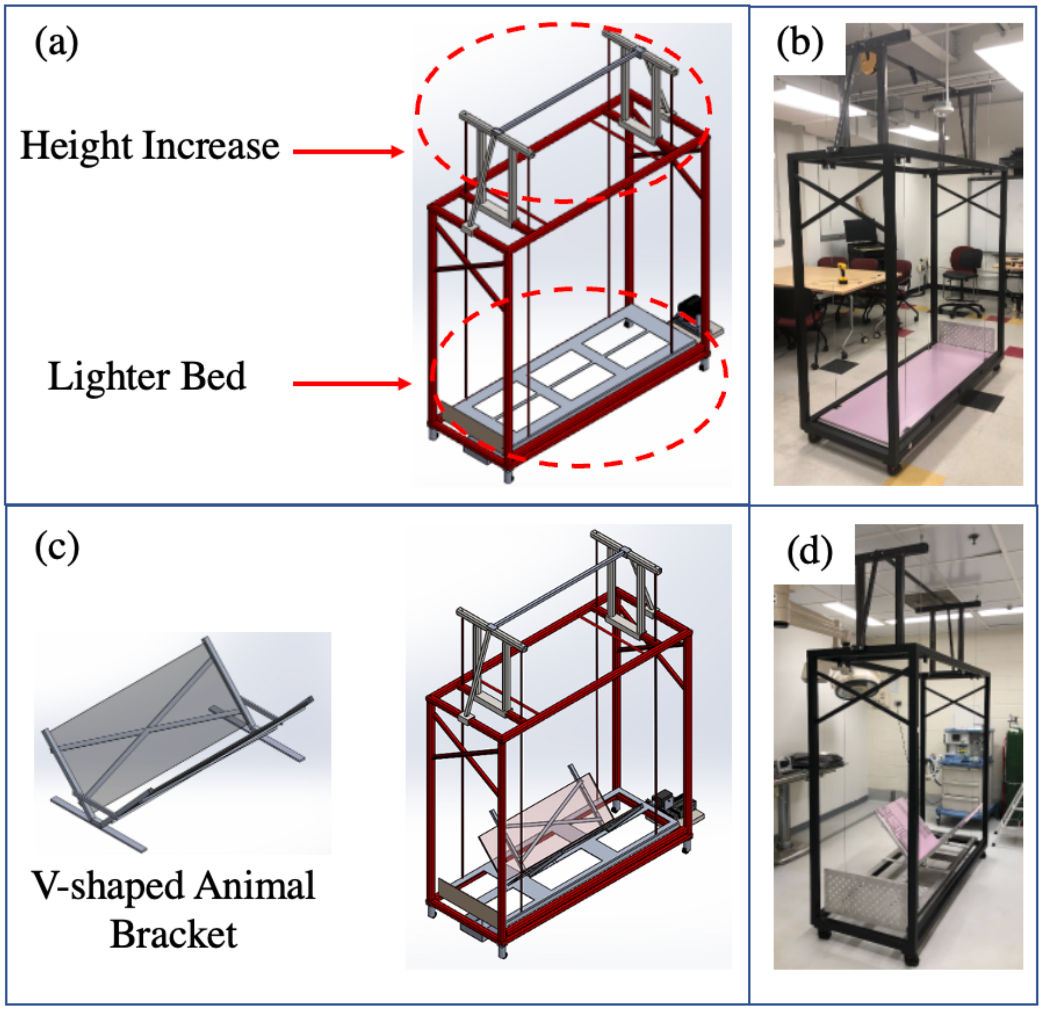

Fig. 6-6: Final design of ULF BCG bed for animal and human testing. (a) The improved design of the human bed with increased cable height and decreased suspended weight (b) Final Fabricated BCG bed for human testing (c) Design of V-shaped bracket attached to the suspended platform for animal testing (d) Final Fabricated BCG bed for animal testing

Two factors in the BCG bed design were changed to improve the BCG recordings. First, the original weight of the constructed moving part in the human platform was reduced by ~50% to reach 12 lb. This was done by cutting portions of the platform out and punching small holes in the remaining parts. Second, the height of the suspension cable was increased by adding a removable height extension component to the external frame. The final length of the cable thus obtained was 93 [in] which is associated with the natural frequency of 0.32 Hz according to Fig. 6-2. The final design of the BCG bed with height extension and decreased weight is shown in Fig. 6-6. For human experiment, a lightweight foam is placed on top of the flat suspended platform. For animal testing, a V-shaped bracket is designed and added on top of the suspended platform to hold the animal (i.e., pig) on its back.

6.7. Characterizing the Model of ULF BCG Bed via Modal Testing

According to [121], modal testing is the process involved in testing components or structures with the objective of obtaining a mathematical description of their dynamic or vibration behavior. However, it must be remembered that no single test or analysis procedure is best for all cases and so it is very important that a clear objective is defined before any test is undertaken so that the optimum methods or techniques may be used. Here the goal was to characterize the mathematical model of the ULF BCG bed and body described in Fig. 6-1. To realize this goal two specific aims were identified. First, the vibration properties of the BCG bed without any subjects lying on it must be found. Second, the binding between the subject's body and the platform on which the subject lies must be identified.

6.7.1 Aim 1: Finding the Vibration Properties of the BCG Bed

A modal test of the BCG apparatus with no subject was performed, to measure the apparatus's vibration properties. This application was borne out of the need to meet the damping requirements for the BCG bed system and to find the model parameter values of the BCG bed (D_b and β_b).

6.7.2 Aim 2: Finding the Spring and Damper Constants in the Body Bed Binding

It was assumed that the binding between the body and the bed is described as a simple spring and damper connection (as shown in Fig. 6-1). A modal test was performed with the primary goal of finding the spring and damper constants in this mathematical model (D_s and β_s).

6.8. Experimental Protocol

In this section the details of three experimental protocols are given which were performed for: (1) characterizing the mathematical model of the body and BCG bed dynamics, (2) testing the efficacy of the BCG instrumentation using the ULF BCG bed in human, (3) investigating the efficacy of BCG instrumentation using the ULF BCG bed in animal.

6.9. Experimental Protocol for Modal Testing

As stated earlier, the optimum modal testing method must be chosen based on the goal and desired applications. In this section, the method of modal testing is suggested for each of the aims mentioned above.

Goal 1: Finding the vibration properties of the BCG bed

The goal was to find the spring and damping constants for the BCG bed (D_b and β_b). For this purpose, an impulse test was performed and the time response of the free vibrations of the BCG bed was measured. A dead load was placed on the swinging part of the bed, equal to the average weight of the subjects in the study. An impulse force was applied on the swinging part by tapping the BCG bed with a hammer. The acceleration of the swinging bed was recorded by placing an accelerometer on the swinging bed and calculating the damping and spring constants leveraging the formulas for the damped vibration of a single degree of freedom system.

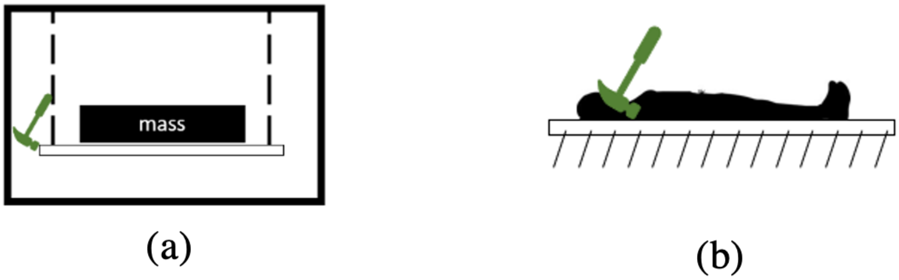

(a)
(b)

Fig. 6-7: Modal testing to find vibration properties of the BCG bed system. (a) Impulse testing on the BCG loaded with dead weight (b) Impulse testing on the body lying on a rigid unmoving floor

Goal 2: Finding the spring and damper constants in the body bed binding

As stated before, the binding between the body and the bed is assumed to be a spring and damper connection with a single degree of freedom and two unknown values (D_s and β_s). The appropriate modal test to find the spring and mass constants is an impulse test. In this experiment, the subject lay on a rigid surface (not the swinging bed) and a tap was applied on the shoulder. An accelerometer was placed on the subject's chest to measure the movements induced in the body by the shoulder tap. The time response of the free vibrations of the body was recorded (by placing an accelerometer on the subject's chest) from 3 human subjects. Then, the spring and damper constants were calculated from the impulse response of the single degree of freedom system. Details follow. In a first degree of freedom system, the equation of motion can be written as

$$m\ddot{x} + C\dot{x} + Kx = F \tag{6-11}$$

Where m, C, K, and F are mass, damping constant, spring constant, and external force applied to the system respectively. Solving the above equation of motion would provide the relationship between overshoot and the period of oscillations. Having the impulse response of the system (as shown in Fig. 6-8), these relationships can be used to find the damping and spring constants associated with the second-order system.

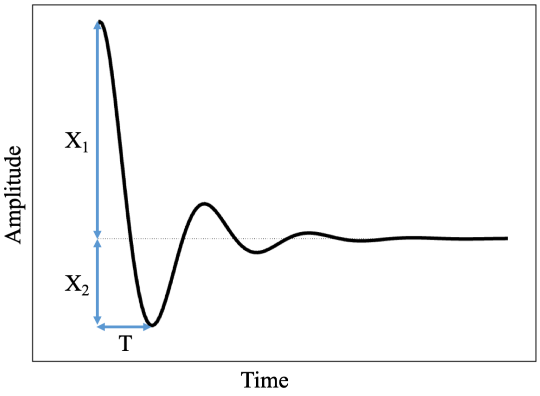

Fig. 6-8: The impulse response of a single degree of freedom damped system indicating the amplitudes in two consecutive inversion points used to calculate overshooting. T is the period of oscillation of the free vibrations.

The values for C_i and K_i, (i = a and s, respectively associated with the binding between the BCG bed and the surrounding, and the binding between the body and the platform) can be calculated by making use of the following equations [122]:

$$C = \frac{4\, m\, ln(\frac{x_1}{x_2})}{T} \tag{6-12}$$

$$K = \frac{16\pi^2 m^2 + C^2 T^2}{4\, m\, T^2} \tag{6-13}$$

6.9.1 Human Pilot Experiments and Data Processing

The efficacy of the BCG bed in measuring the BCG signals was tested by collecting data from 5 human subjects (Fig. 6-9 (a)). The following signals were collected in each subject: (i) an ECG acquired using 3-gel electrodes in the lead II configuration and interfaced with a wireless amplifier (BN-EL50, Biopac Systems, Goleta, CA, USA), (ii) a wearable chest BCG in the head-to-foot direction acquired using an accelerometer (PCB356A32, PCB Piezoelectronics, Inc., NY, USA), (iii) a bed BCG in the head-to-foot direction acquired using an accelerometer (PCB356A32, PCB Piezoelectronics, Inc., NY, USA). The signals were acquired at a sampling rate of 1 kHz. The subjects were asked to lie still on the suspended platform.

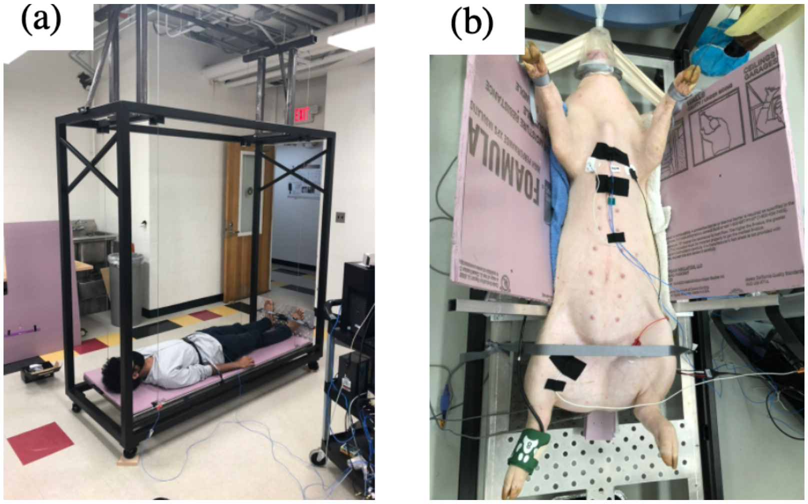

Fig. 6-9: Experimental setup for the recording of BCG signal using the BCG bed apparatus in (a) Human (b) Animal

The data was collected during two periods when subjects were breathing and then they were asked to hold their breath and the measurement was repeated. After band pass filtering (0.5 to 10 Hz) the individual BCG beats were identified using the ECG R waves as the gating reference. The BCG beats associated with each beat were concatenated and representative BCG beats were calculated by taking the median of all beats.

6.9.2 Animal Pilot Experiments and Data Processing

Under the approval of the Institutional Animal Care and Use Committee (IACUC), data from 2 swine subjects was collected under anesthesia and in strict accordance with the IACUC guidelines (Fig. 6-9 (b)). Once general anesthesia and mechanical ventilation were established, the following signals were collected using a Biopac MP 150 data acquisition system (Biopac Systems, Goleta, CA, USA) with a sampling frequency of 1KHz: (i) an ECG acquired using 3-gel electrodes in the lead II configuration (Biopac Systems, Goleta, CA, USA), (ii) chest head-to-foot and anterior-posterior BCG signals were acquired by placing an accelerometer on the midsternum (PCB356A32, PCB Piezoelectronics, Inc., NY, USA). (iii) a bed BCG signal in the head-to-foot direction was acquired by placing an accelerometer on the suspended platform of the BCG bed. ECG R-peaks were detected using the famous Pan-Tompkins method [123] and used for gating the cardiac beats. BCG signals were band-pass filtered (0.5 to 10 Hz). The periodic peaks in the BCG bed signal associated with large respiration-induced motion were detected and the distorted cardiac beats in the vicinity of the respiratory peaks were excluded from further analysis. A representative wave was calculated by taking the median of the remaining beats.

6.10. Results

Fig. 6-10 (a) shows the impulse response of the BCG bed when it is loaded with a dead weight. Fig. 6-10 (b) shows an example plot of the impulse response of the human body when a tap is applied on the shoulder. Table 6-1 shows the calculated spring and damping constants in the mathematical model of Fig. 6-1 obtained from the impulse tests.

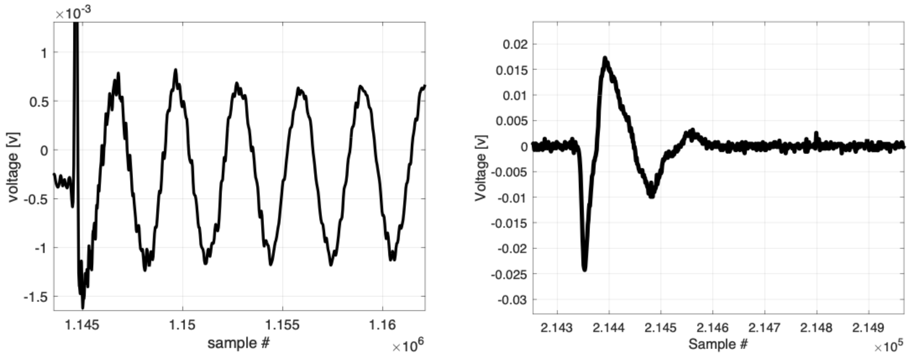

(a) (b)

Fig. 6-10: Free vibration due to an impulse associated with (a) ULF BCG Bed (b) Human subjects lying on a fixed platform

Table 6-1: The values of spring and damping constants for the binding between the BCG bed and the surrounding (Ka and Ca) as well as the average values of the three subjects associated with the spring and damping constants indicating the binding between the supine body and the platform (Ks and Cs)

Property	BCG bed (a)	Body (s) [mean+/-std]
Spring Constant (K) [Kg/s]	168	4967080 +/- 2964613
Damping Constant (C) [Kg/s^2]	22	6139 +/- 4014

Fig. 6-11 shows the representative head-to-foot bed BCG, head-to-foot chest BCG, and anterior-posterior chest BCG. The acceleration BCG signals acquired from the ULF BCG bed system, especially in human subjects have the general morphology of the records published from other ULF systems. The major I, J, and K waves can be clearly detected in the representative BCG signals. The signals exhibited a very consistent pattern in human subjects during the breath-holding period. In the animal, after removing the periods affected by respiration a consistent pattern in the BCG bed signal can be observed.

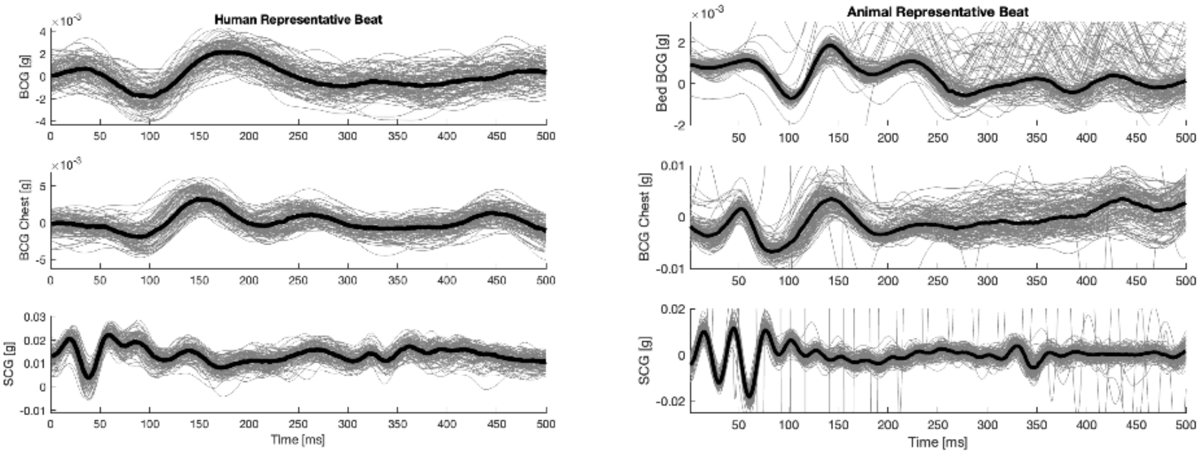

(a) (b)

Fig. 6-11: Representative BCG acquired from the BCG bed apparatus. The top plot is associated with the BCG sensor placed on the suspended platform. The middle plot is associated with the head-to-foot component of the BCG signal acquired from the sensor placed on the subject's chest. The bottom plot is associated with the anterior-posterior component of the BCG signal acquired from the BCG sensor placed on the subject's chest (a) Human BCG. (b) Animal BCG.

6.11. Conclusion

To ultimately evaluate the mathematical model developed in this work, ground truth BCG waves must be measured. Therefore, a BCG instrumentation apparatus was designed by the study of devices in the literature and built to give BCG measurements closest in nature to the "true" BCG in the model. The BCG apparatus consisted of a light platform suspended from a rigid frame. Two designs were constructed to accommodate both human and animal subjects. The physical basis of the BCG apparatus was studied and the mathematical model explaining the dynamics of the body and the BCG bed was characterized using experimental data. Pilot human and animal studies were performed using the BCG bed apparatus to investigate its capability to measure the BCG waveform. The recordings obtained from the BCG bed were close in morphology to the recordings reported in the literature which confirms the efficacy of the apparatus in BCG instrumentation.

Chapter 7: BCG Posture Study

7.1. Introduction

Pulse transit time (PTT) is one of the most widely investigated approaches to cuff-less blood pressure (BP) tracking [124]–[127]. One long-standing challenge associated with PTT is inconvenience associated with the acquisition of both proximal and distal arterial pulses. Recently, the ballistocardiogram (BCG) is receiving an increasing interest as a convenient timing reference for PTT computation [84], [128]–[130], by virtue of its unique advantage that it can be acquired at a distal body site (e.g., foot [84], [128], [129] or wrist [130]) to provide a timing associated with a proximal event (e.g., aortic valve opening). Despite its susceptibility to noise and artifacts, the BCG has the potential to advance cuff-less BP tracking by virtue of its direct relationship to arterial BP [131], [132], either by itself or together with other physiological signals including the electrocardiogram (ECG) and the photoplethysmogram (PPG). Prior work suggests that PTT defined as the time interval between fiducial points in the BCG (e.g., I wave in the force plate and weighing scale BCG [84], [128]–[130] and J wave in the wrist acceleration BCG [130], the use of which are supported by the physical mechanisms underlying the genesis of the BCG [131], [132]) and the PPG (e.g., foot) has a remarkable correlation with BP (especially diastolic BP (DP)).[2]

A major shortcoming of existing work on BP tracking via wrist BCG-PPG PTT is that its implementation is limited to a specific posture: standing with arms vertically held down in the

---

[2] This work has been published in [139]. The author of this dissertation has contributed to the data collection, statistical analysis, and analysis of the mechanisms.

head-to-foot direction. Its versatility and generalizability in other postures has not been studied much. Considering the low signal-to-noise ratio associated with the wrist BCG signal, its acquisition must ideally be performed under minimal body motions. While standing posture is reasonably convenient, there are body postures more convenient than standing (e.g., sitting and supine) that may yield less body motions. In addition, constraining the arm to the main trunk (e.g., by placing the hand on the chest or by putting the hand on the shoulder) rather than holding it down vertically in the head-to-foot direction may help in suppressing wrist motions during BCG acquisition. However, neither the influence of the postural deviation from standing with arms vertically held in the head-to-foot direction on the efficacy of wrist BCG-PPG PTT in cuff-less BP tracking, nor the physical mechanisms responsible for the influence (if there is any), is known. A prior work reported that posture influences the BCG signal [32]. Hence, it is possible that BCG-PPG PTT varies with respect to posture even when BP remains constant. Yet, prior research to understand the impact and mechanism of posture on the BCG and PTT is very rare. To enhance the versatility and robustness of wrist BCG-PPG PTT in BP tracking, the variability in wrist BCG-PPG PTT with respect to a wide range of postural changes as well as the underlying physical mechanisms responsible for such a variability must be understood.

Toward the ultimate goal of enabling robust cuff-less BP tracking with wrist wearables against postural changes, the goal of this chapter is to investigate the posture-dependent variability in wrist BCG-PPG PTT. BCG and PPG signals were acquired from 25 subjects under the combination of 3 body (standing, sitting, and supine) and 3 arm (vertical in head-to-foot direction, placed on the chest, and holding a shoulder) postures. PTT was computed as the time interval between the BCG J wave and the PPG foot, and its variability with respect to the 9 postures was analyzed by invoking an array of possible physical mechanisms. To the best of our knowledge, our work revealed the posture-induced changes in PTT and PAT in depth for the first time, by invoking and quantifying the effect of possible physical mechanisms responsible for such changes. The physical mechanisms discovered, and the analysis performed in this chapter may be applicable to the study of changes in various PTT under diverse postures not considered in this chapter.

7.2. Human Subject Study

Under the approval of the University of Maryland Institutional Review Board (IRB, ID 813845 approved in June 2019) and written informed consent, a total of 25 healthy volunteers was studied by strictly following the IRB guidance. The subjects included 16 males and 9 females (age: 29+/-9 years; weight: 67+/-13 kg; height 170+/-11 cm: mean+/-SD).

7.2.1 Data Acquisition

Upon arrival and completing written informed consent, we placed sensors to each subject to measure the following signals: (i) an ECG measured with 3-gel electrodes in the Lead II configuration and interfaced to a wireless amplifier (BN-EL50, Biopac Systems, Goleta, CA, USA); (ii) a finger clip PPG measured as a surrogate of wrist PPG using a transmittance mode PPG sensor (TSD124A, Biopac Systems, Goleta, CA, USA) and interfaced to a wired amplifier (DA100C, Biopac Systems, Goleta, CA, USA); (iii) a wrist BCG measured using a 3-axis accelerometer and interfaced to a wireless amplifier (BN-ACCL3, Biopac Systems, Goleta, CA, USA); and (iv) a non-invasive arterial BP waveform measured using a fast servo-controlled finger cuff embedded with a blood volume pulse sensor on the ring finger of a hand, which was height-compensated and then transformed to brachial BP (ccNexfin, Edwards Lifesciences, Irvine, CA, USA) so that the measured BP was not affected by postural-induced changes in hydrostatic pressure. We recorded all these signals synchronously at a sampling rate of 1 kHz throughout the study.

After all the sensors were placed, we recorded the signals while each subject took the combination of 3 body (standing, sitting, and supine) and 3 arm (vertical in head-to-foot direction and (HF), placed on the chest (PC), and holding a shoulder (HS)) postures (Fig. 7-1) one after the other as follows. First, the subject was asked to stand still and take HF, PC, and HS postures. Second, the subject was asked to sit on a stool and take HF, PC, and HS postures. Third, the subject was asked to lie on a camping bed and take HF, PC, and HS postures. In each posture, we recorded all the signals for at least 1 min after confirming that transients during postural changes were settled via the visual inspection of the signal waveforms for beat-to-beat consistency.

We used the component of the 3-axis wrist BCG most closely aligned with the head-to-foot direction for data analysis. This corresponds to the superior-inferior axis (shown as Y axis in Fig. 1) in case of HF and the anterior-posterior axis (shown as X axis in Fig. 7-1, which gets approximately aligned with head-to-foot direction, although not perfectly) in case of PC and HS.

7.2.2 Data Analysis

We pre-processed the ECG using a 4th-order Butterworth high-pass filter with the cut-off frequency of 0.1 Hz and the PPG and the BCG using a 2nd-order Butterworth band-pass filter with the pass band of 0.5 Hz-10 Hz. We segmented the data acquired in each subject into 9 periods, each corresponding to each of the 9 postures (Fig. 7-1). Then, we computed BP (both systolic and diastolic) and heart rate representative of each posture in each subject as follows. First, we detected the R waves in the ECG signal by (i) detecting the R waves as local peaks and (iii) removing erroneously detected local peaks that are not the R waves. Second, we gated cardiac beats using the ECG R waves, as time intervals between the neighboring ECG R waves. Third, we computed BP and heart rate associated with each cardiac beat. Fourth, we computed BP and heart rate representative of each posture in each subject as their median values associated with all the gated beats in the period corresponding to the posture in each subject. Finally, we computed BP and heart rate representative of each posture by taking the mean and standard deviation (SD) of these parameters across all the 25 subjects.

In addition, we computed pulse arrival time (PAT: the time interval between the ECG R wave and the PPG foot) and PTT representative of each posture in each subject as follows. First, we detected the PPG foot in each cardiac beat using the intersecting tangent method [133]. Second, we derived the wrist BCG signal representative of each posture as the average of all the gated wrist BCG beats in the period corresponding to the posture in each subject. Third, we detected the BCG J wave in the representative wrist BCG signal as the local peak in the BCG signal between the ECG R wave and the PPG foot. Fourth, we derived the PPG foot timing representative of each posture by taking the median value of all the PPG foot timings relative to the ECG R waves in the period corresponding to the posture in each subject. Fifth, we derived PTT representative of each posture in each subject as the time interval between the BCG J wave and the representative PPG foot timing. Finally, we derived PTT representative of each posture by taking the mean and SD of PTT across all the 25 subjects.

Fig. 7-1: Body and arm posture for BCG acquisition. Body postures (rows): standing, sitting, and supine. Arm postures (columns): vertical in <u>h</u>ead-to-<u>f</u>oot direction (HF), <u>p</u>laced on the <u>c</u>hest (PC), and <u>h</u>olding a <u>s</u>houlder (HS).

We used the repeated-measures two-way ANOVA test to determine the effects of body posture and arm posture as well as their interactions on BP, heart rate, PTT, and PAT. In case the statistical significance was verified, we used the Tukey's HSD multiple comparison tests as post-hoc analysis. Statistical significance was concluded when $p<0.05$. We performed all the statistical analysis using JMP (Version 14, SAS Institute Inc., Cary, NC).

7.3. Results

Table 7-1 summarizes (a) BP and (b) heart rate associated with all the body/arm postures. Table 7-2 summarizes (a) wrist BCG-PPG PTT and (b) PAT associated with all the body/arm postures. Fig. 7-2 presents the profile plots associated with BP, heart rate, PTT and PAT. Fig. 7-3 presents representative wrist BCG waveforms associated with all the body/arm postures. BP and heart rate were comparable between standing and sitting postures. However, they were lower in supine posture than in standing and sitting postures, which may be due to an increase in vagal activations in the former than the latter. Indeed, we found a significant difference in DP, SP, and heart rate with respect to body posture (DP: $F(2,216)=278.88$, $p<0.001$; SP: $F(2,216)=77.58$, $p<0.001$; heart rate: $F(2,216)=177.63$, $p < 0.001$). But there was no significant difference in DP, SP, and heart rate with respect to arm postures. The interaction between body and arm postures was not significant. Tukey post-hoc test revealed that (i) DP and SP were significantly lower in supine posture than in standing and sitting postures and (ii) only SP but not DP was significantly different between standing and sitting postures; while (iii) heart rate was significantly different in all the body postures, highest in standing posture and lowest in supine posture. However, the absolute difference in SP and heart rate between standing and sitting postures was small.

Table 7-1: (a) Blood pressure (BP) and (b) heart rate associated with all the body/arm postures

(a) BP: systolic/diastolic [mmHg]: mean (SE)

	Standing	Sitting	Supine
HF	113 (3)/ 69 (2)	116 (3)/ 69 (2)	102 (3)/ 57 (2)
PC	111 (2)/ 68 (1)	114 (2)/ 69 (2)	106 (3)/ 58 (2)
HS	112 (2)/ 69 (2)	115 (2)/ 69 (2)	105 (3)/ 57 (2)

(b) Heart rate [bpm]: mean (SE)

	Standing	Sitting	Supine
HF	80 (2)	78 (2)	68 (2)
PC	83 (2)	79 (2)	67 (2)
HS	85 (2)	79 (2)	67 (2)

Table 7-2: (a) Wrist BCG-PPG pulse transit time (PTT) and (b) pulse arrival time (PAT) associated with all the body/arm postures.

(a) PTT: mean (SE) [ms]

PTT	Standing	Sitting	Supine
HF	106 (3)	104 (4)	125 (4)
PC	91 (3)	90 (4)	95 (5)
HS	75 (5)	65 (5)	75 (5)

(b) PAT: mean (SE) [ms]

PAT	Standing	Sitting	Supine
HF	273 (4)	271 (4)	268 (4)

PC	283 (4)	284 (5)	274 (5)
HS	283 (5)	274 (4)	267 (4)

PAT practically remained comparable across all the body and arm postures, although there were statistically significant differences. We found a significant difference in PAT with respect to both body posture (F(2,216)=35.86, p<0.001) and arm posture (F(2,216)=28.31, p<0.001) as well as a significant interaction between them (F(4,216)=3.28, p=0.013). However, the absolute difference in PAT between different postures was small.

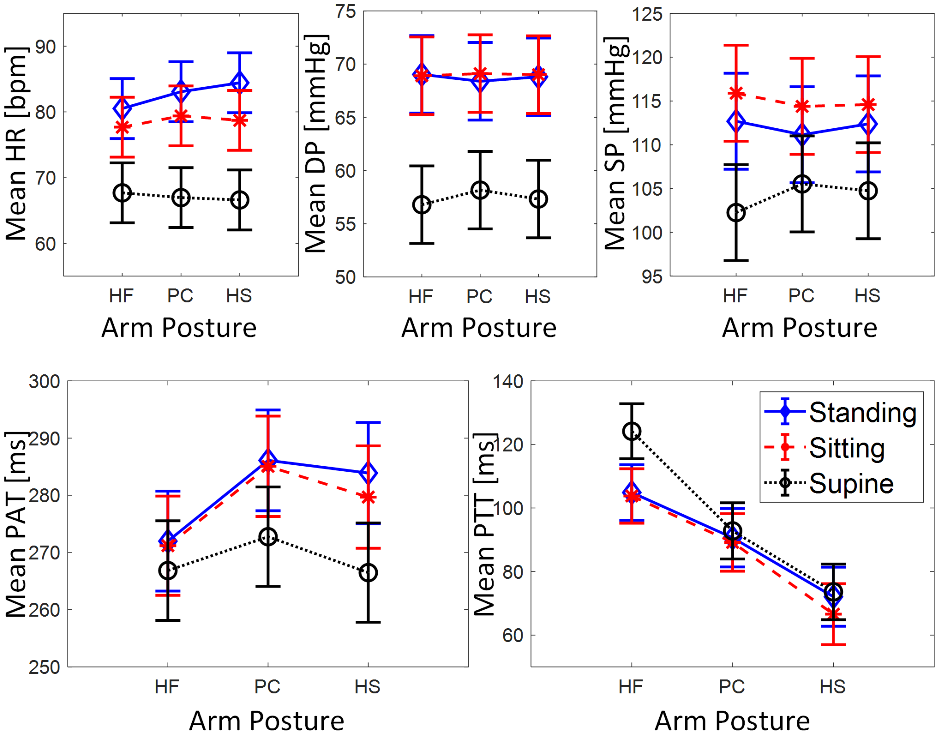

Fig. 7-2: Profile plots associated with (a) blood pressure (BP), (b) heart rate, (c) PTT and (d) PAT.

In contrast to PAT, PTT varied in response to changes in both body and arm postures. We found a significant difference in PTT with respect to both body posture (F(2,216)=9.67, p=0.001) and arm posture (F(2,216)=129.44, p<0.001) as well as a significant interaction between them

(F(4,216)=3.66, p=0.007). Tukey post-hoc test revealed that (i) PTT was not significantly different between standing and sitting postures; (ii) PTT was significantly larger in supine posture than in standing and sitting postures; (iii) PTT was significantly smaller in PC and HS than in HF; and (v) PTT was significantly larger in PC than in HS.

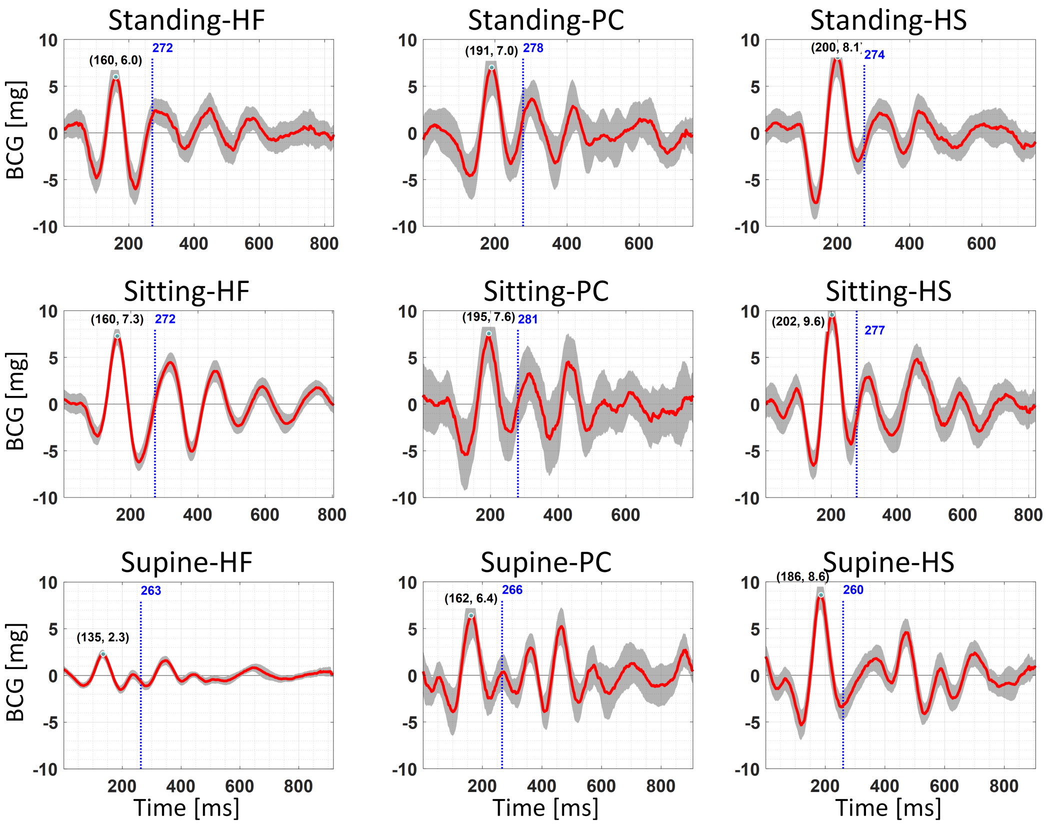

Fig. 7-3: Representative wrist BCG waveforms associated with all the body/arm postures. J wave timing and amplitude are shown in black. PPG foot timing is shown in blue.

The wrist BCG waveform exhibited a large posture-dependent variability. In regard to its body posture-dependent variability, the wrist BCG waveform remained quite consistent in standing and sitting postures while being largely altered in supine posture in case of HF. In particular, the waveform amplitude was decreased, and the timings associated with the fiducial points were altered. In contrast, the wrist BCG waveform remained quite consistent in all the body postures considered in this work in case of PC and HS. In regards to its arm posture-dependent variability, the wrist BCG waveform exhibited distinct morphology associated with HF, PC, and HS. In all the body postures considered in this work, the amplitudes of the I and J waves were larger in HS. In HF, PC, and HS, the timings of the fiducial points (e.g., the J wave) were also notably altered.

7.4. Discussion

Despite its potential for ultra-convenient BP tracking, prior work on BCG-based PTT has been restricted to standing posture with arms vertically held in the head-to-foot direction. It would be ideal if the BCG could provide robust fiducial points for PTT computation in a wide range of body and arm postures. But the impact of body and arm postures on the BCG waveform, and accordingly, the fiducial points therein, remains unknown. Thus, the goal of this work was to investigate the posture-dependent variability of a BCG-based PTT (wrist BCG-PPG PTT). For this purpose, we designed and conducted a human subject study in which wrist BCG-PPG PTT was measured under 9 postures while BP was stably maintained. We invoke possible physical mechanisms responsible for the posture-induced variability in the wrist BCG-PPG PTT. Then, we analyze and interpret the experimentally observed posture-dependent PTT variability using these physical mechanisms. Details follow.

7.4.1 Posture-Dependent Wrist BCG-PPG PTT Variability: Possible Physical Mechanisms

There are an array of physical mechanisms potentially responsible for the posture-induced variability in the BCG-PPG PTT:

1) BP at the heart level: PTT is inversely proportional to BP at the heart level [124], which is the basis for PTT-based cuff-less BP tracking. Hence, BP variability associated with the changes in body and arm postures is responsible for PTT variability associated with these postures.

2) Hydrostatic pressure: In addition to BP at the heart level, PTT is also affected by the hydrostatic pressure due to the height difference between the heart and the wrist. In the presence of height difference between the heart and the wrist, the arterial path between the heart and the wrist is subject to varying BP. Noting that BCG represents the heart event (e.g., aortic valve opening) while PPG represents the distal event (i.e., pulse arrival at the wrist site), the resulting wrist BCG-PPG PTT is determined by the varying BP level along the arterial path from the heart to the wrist rather than just by BP at the heart level. For example, in case of standing posture with arms vertically held in the head-to-foot direction (i.e., HF), the wrist may be approximately 50 cm below the heart level, which may correspond to 35 mmHg increase BP at the wrist approximately relative to BP at the heart level [76]. Hence, the arterial path from the heart to the wrist is subject to an increasing BP: from the heart-level BP at the heart to the heart-level BP plus 35 mmHg at the wrist. Accordingly, the resulting PTT is smaller than PTT when the arm is at the same height as the heart.

3) BCG instrument orientation: In standing posture with arms vertically held in the head-to-foot direction (i.e., HF), the BCG instrument in the wrist wearable acquires the BCG exactly in the head-to-foot direction. If the arm is not held strictly in the head-to-foot direction, the orientation of the BCG instrument is not aligned with the head-to-foot direction. The resulting BCG may be associated with morphology distinct from that of the typical head-to-foot BCG. This distortion in the wrist BCG morphology may alter the timings of the fiducial points therein and the corresponding PTT.

4) Vibration transmission characteristics: How the vibration due to the blood ejected by the heart is transmitted through the body to the wrist may depend on body and arm postures. For example, vibration transmission characteristics may differ between HF and PC/HS, since in the latter the arm is firmly attached to the main trunk. The effect of body and arm postures on the vibration transmission characteristics of the body is largely unknown and is essentially a black box. However, the alteration in the vibration transmission characteristics may alter the morphology of the wrist BCG signal, the fiducial points therein (especially their timings), and ultimately, PTT.

5) PPG instrument-wrist contact pressure: The morphology of the PPG signal is affected by the trans-mural pressure at the PPG-body contact (called hereafter the contact pressure). Our team's recent work showed that PTT computed with PPG as the distal timing reference increases as the PPG-body contact pressure increases in the positive trans-mural pressure regime due to the pressure-dependent change in arterial viscoelasticity [134]. Considering that wrist BP decreases as the arm is raised above the heart level, the PPG-wrist contact pressure decreases as the arm is raised. This decreases the wrist BCG-PPG PTT.

6) Body-environment link: How the body is linked to the environment may also be responsible for the wrist BCG-PPG PTT by altering the BCG morphology. In particular, the BCG morphology may be more damped and its fiducial points delayed in supine posture than in standing and sitting postures due to larger friction at the body-environment interface (i.e., bed in supine; floor in standing; and chair in sitting).

In summary, the change in PTT due to the change in posture (ΔT) may be given by:

$$\Delta T = \Delta T_1 + \Delta T_2 + \Delta T_3 + \Delta T_4 + \Delta T_5 + \Delta T_6 \tag{7-1}$$

where ΔT_1- ΔT_6 are the changes in PTT due to changes in (i) BP at the heart level, (ii) hydrostatic pressure, (iii) BCG instrument orientation, (iv) vibration transmission characteristics, (v) PPG instrument-wrist contact pressure, and (vi) body-environment link, respectively. Note that only ΔT_1 is relevant in the context of PTT-based BP tracking, whereas ΔT_2- ΔT_6 are disturbances that adversely impact the accuracy of BP tracking. In interpreting the experimental results, we capitalize on prior work on the effect of BP (at the heart level) and PPG instrument-body contact pressure on PTT. According to a prior work [135], 1 mmHg BP change may yield approximately 2 ms PTT change in the opposite direction on the average:

$$\Delta T_1 = 2\Delta P, \Delta T_2 = 2\Delta P_H \tag{7-2}$$

where ΔP is the change in BP at the heart level and ΔP_H is the change in hydrostatic pressure. According to our recent work, 1 mmHg contact pressure change may yield approximately 0.2 ms PTT change in the same direction on the average [134]:

$$\Delta T_5 = 0.2\Delta P_c \tag{7-3}$$

where ΔP_c is the change in PPG instrument-wrist contact pressure. These relationships may not generalize perfectly to any subject. Yet, they may still be useful in understanding the relative importance of the physical mechanisms.

7.4.2 Posture-Dependent Wrist BCG-PPG PTT Variability: Interpretation of Results

The wrist BCG-PPG PTT exhibited a few notable behaviors with respect to the changes in body posture and arm posture. First, we will compare and interpret PTT due to body posture change in HS versus PC and HS. Second, we will compare and interpret PTT due to arm posture change in standing and sitting versus supine. Details follow.

Effect of Body Posture Change on PTT

Summary: In HF, the wrist BCG-PPG PTT remained consistent in standing and sitting postures, while it showed drastic increase in supine posture (Table 7-2 (a)). In PC and HS, the wrist BCG-PPG PTT essentially remained consistent across all the body postures considered in this work (Table 7-2 (a)).

Details: In HF, there is little difference in BP at the heart level, hydrostatic pressure, BCG instrument orientation, vibration transmission characteristics, and PPG instrument-wrist contact pressure between standing and sitting postures. In addition, the body-environment link may have had minimal impact on the motions of body and wrist in the head-to-foot direction, as suggested by the comparable wrist BCG waveforms in these body postures (Fig. 7-3). In contrast, there were a number of differences in the physical mechanisms in supine posture compared with standing and sitting postures: (i) BP at the heart level was lower in supine than standing and sitting postures (Table 7-1: (a) Blood pressure (BP) and (b) heart rate associated with all the body/arm postures (a)); (ii) hydrostatic pressure between the heart and the wrist decreased in supine relative to standing and sitting postures; (iii) PPG instrument-wrist contact pressure likewise decreased in supine relative to standing and sitting postures; (iv) body motion may have been more constrained in supine posture than in standing and sitting postures due to much larger contact area at the body-bed interface (encompassing trunk, arms, and legs) than foot-floor and hip-chair interface. The supine posture was associated with approximately 10 mmHg lower BP, 18 mmHg lower effective hydrostatic pressure (in that the arterial path in HF was subject to an increasing BP from its proximal (heart BP) to distal (heart BP plus 35 mmHg) sites assuming the arm length of 50 cm in standing and sitting postures), and 45 mmHg lower PPG instrument-wrist contact pressure. This may approximately amount to 20 ms increase (Eq. (7-2)), 36 ms increase (Eq. (7-2)), and 9 ms decrease (Eq. (7-3)) in PTT, totaling 47 ms increase in PTT. Noting that (i) PTT was larger in supine posture than in standing and sitting postures by approximately 20 ms (Table II(a)), and that (ii) PAT did not change much across body postures (Table 7-2 (b); which means that the time interval between the ECG R wave and the PPG foot did not change much and the change in PTT is primarily attributed to the change in the location of the wrist BCG J wave relative to the PPG foot), it is our speculation that the friction at the body-bed interface may have decreased PTT by approximately 27 ms by distorting the BCG waveform and specifically lagging its J wave by 27 ms.

Noting that wrist was constrained approximately at the heart level in PC and HS with one axis of the BCG instrument approximately aligned with the head-to-foot direction, there may have been negligible difference in hydrostatic pressure due to arm posture, BCG instrument orientation, and vibration transmission characteristics across 3 different body postures. Indeed, assuming the distance of 5 cm between the heart and the wrist (amounting to 1.8 mmHg decrease in hydrostatic pressure), the supine posture may be associated with approximately <4 ms increase in PTT due to hydrostatic pressure relative to standing and sitting postures (Eq. (7-2)). But at the same time, there were a number of differences in the physical mechanisms in supine posture compared with standing and sitting postures: (i) the supine posture was associated with 10 mmHg lower BP at the heart level (Table 7-1 (a)) and 14 mmHg (due to 10 mmHg decrease in BP at the heart level + 4 mmHg decrease in hydrostatic pressure) lower PPG instrument-wrist contact pressure relative to standing and sitting postures; and (ii) the friction at the body-bed interface in supine posture may have decreased PTT (as described above). This may approximately amount to 20 ms increase (Eq. (7-2)), <3 ms decrease (Eq. (7-3)), and 27 ms decrease in PTT, totaling 6 ms decrease in PTT. Noting that PTT remained practically the same (Table 7-2 (a)), 6 ms may be attributed to the approximations associated with our calculation and may practically be negligible.

Effect of Arm Posture Change on PTT

Summary: PTT showed drastic decrease in PC and HS relative to HF in all the body postures (Table 7-2 (a)).

Details: On one hand, BP level was essentially the same in all the arm postures associated with each body posture (Table 7-1 (a)). In addition, the change in BCG instrument orientation was minimal (not shown). On the other hand, there were a number of differences in the physical mechanisms between PC and HS versus HF. In case of standing and sitting postures, the change in the height of the wrist with respect to the heart associated with PC and HS relative to HF may have yielded approximately 36 ms increase in PTT (due to an effective 18 mmHg decrease in the hydrostatic pressure as described above; Eq. (7-2)). This increase in PTT may have been modestly reduced by the decrease in the PPG instrument-wrist contact pressure; the contact pressure was lower by 35 mmHg in PC and HS than HF, which approximately decreases PTT by 7 ms (Eq. (7-3)). Noting that there was no difference in body-environment link in each body posture, it is our speculation that the vibration transmission characteristics may have been a key physical mechanism responsible for the drastic PTT decrease in PC and HS associated with standing and sitting postures (approximately 40~70 ms, given a resultant decrease in PTT of 10~40 ms (Table 7-2 (a))). In case of supine posture, there may have been minimal difference in hydrostatic pressure and PPG instrument-wrist contact pressure (whose effect on PTT may be <4 ms increase (Eq. (7-2)) and <1 ms decrease (Eq. (7-3)), respectively, as described above), and perhaps also in body-environment link between PC and HS versus HF. In addition, the change in BCG instrument orientation was minimal (not shown). Hence, it is our speculation that the vibration transmission characteristics again may have been a key physical mechanism responsible for the drastic PTT decrease in PC and HS associated with supine posture (approximately 30~50 ms, given a resultant decrease in PTT of 30~50 ms (Table 7-2 (a))). As mentioned earlier, the exact mechanism underlying how the posture affects the vibration transmission characteristics and how the vibration transmission characteristics affects wrist BCG-PPG PTT is unknown, other than the conjecture that it may substantially distort the wrist BCG waveform and shift the timings of the fiducial points therein (lagging the J wave in particular; Fig. 7-3). Indeed, PAT did not change much across arm postures (Table 7-2 (b); which means that the time interval between the ECG R wave and the PPG foot did not change much and the change in PTT is primarily attributed to the change in the location of the wrist BCG J wave relative to the PPG foot). Hence, it is our speculation that changing arm posture from HF to PC and HS decreased PTT primarily by distorting BCG waveform, perhaps through the changes in both the mechanical characteristics (e.g., stiffness and damping) of the body and the excitation pathways associated with the changes in posture.

Table 7-3 shows the decomposition of the posture-dependent wrist BCG-PPG PTT variability into the possible physical mechanisms. Fig. 7-4 provides a visual summary of the primary disturbances associated with the effect of body and arm postures on wrist BCG-PPG PTT.

Table 7-3: (a) Blood pressure (BP) and (b) heart rate associated with all the body/arm postures

(a) Body posture change from standing/sitting to supine.

	1	**2**	**3**	**4**	**5**	**6**	**Total**
HF	+20 ms	+36 ms	0 ms	0 ms	-9 ms	-27 ms	+20 ms
PC/HS	+20 ms	+4 ms	0 ms	0 ms	-3 ms	-27 ms	-6 ms

(b) Arm posture change from HF to PC/HS.

	1	**2**	**3**	**4**	**5**	**6**	**Total**
Standing/Sitting	0 ms	+36 ms	0 ms	-40~-70 ms	-7 ms	0 ms	-15~-40 ms
Supine	0 ms	+4 ms	0 ms	-30~-50 ms	-1 ms	0 ms	-30~-50 ms

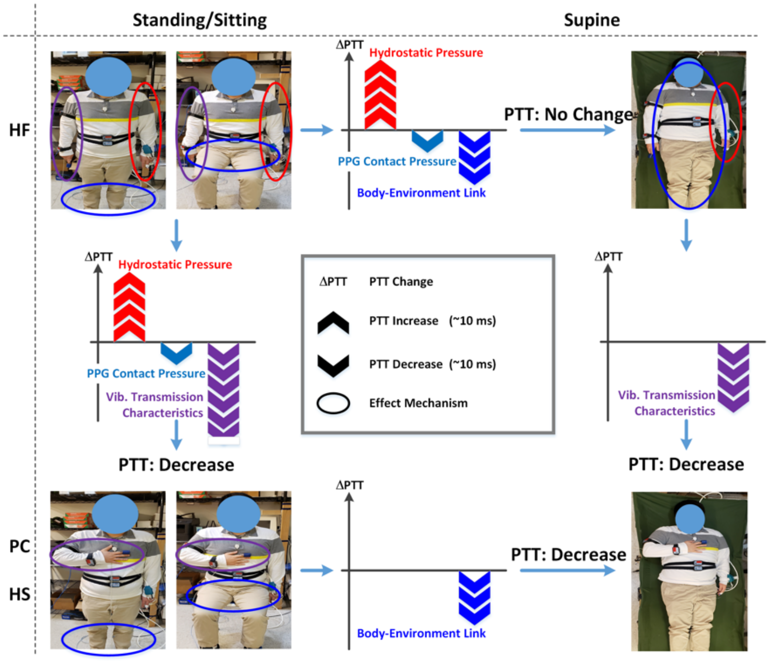

Fig. 7-4: Visual summary of the primary disturbances associated with the effect of body and arm postures on wrist BCG-PPG PTT. BP at the heart level is assumed to remain constant.

Posture-Dependent PAT Variability: Interpretation of Results

Although the primary focus of this chapter is to understand posture-dependent PTT variability, it may also be of interest to understand posture-dependent PAT variability. Noting that PAT is influenced by (i) a subset of the physical mechanisms influencing PTT and (ii) pre-ejection period (PEP), posture-dependent PAT variability may be understood by capitalizing on the results in Table 7-3 and the posture-dependent PEP variability. In particular, PAT is influenced by BP at the heart level, hydrostatic pressure between the heart and the wrist, and PPG instrument-wrist contact pressure while it is not influenced by BCG instrument orientation, vibration transmission characteristics, and body-environment link. In addition, prior work suggests that PEP tends to (i) decrease in supine posture relative to standing and sitting postures due to increased vagal activations and (ii) remain more or less the same in standing and sitting postures [136], [137]. First, consider the PAT variability with respect to body posture. In Table 7-3 (a), BP at the heart level, hydrostatic pressure, and PPG instrument-wrist contact pressure yield approximately 47 ms increase in PTT in HF, and 21 ms increase in PTT in PC and HS in case the body posture changes from standing and sitting to supine. Considering that PAT remained the same in HF while decreased by approximately 10 ms in PC and HS when the body posture changed from standing and sitting to supine (Table 7-2 (b)), it is our speculation that PEP may have decreased by approximately 30~50 ms due to the body posture change. Second, consider the PAT variability with respect to arm posture. In Table 7-3 (b), BP at the heart level, hydrostatic pressure, and PPG instrument-wrist contact pressure yield approximately 29 ms increase in PTT in standing and sitting postures, and 3 ms increase in PTT in supine posture in case the arm posture changes from

HF to PC and HS. Considering that PEP may not have changed during the arm posture change, PAT is predicted to increase by approximately 29 ms in standing and sitting postures while remain more or less the same in supine posture. Our prediction is modestly consistent with the experimental PAT variability of approximately 10 ms increase in standing and sitting postures as well as no change in supine posture (Table 7-2 (b)).

Finally, it is emphasized that numerical estimates of the PTT and PAT variability associated with each of the physical mechanisms predicted in our work (including those shown in Table 7-3) are likely not exact. Nonetheless, they may still be useful in qualitatively determining major physical mechanisms responsible for posture-dependent PTT and PAT variability. In fact, Table 7-3 suggests that hydrostatic pressure between the heart and the wrist, vibration transmission characteristics, and body-environment link appear to be major mechanisms that act as disturbance in the context of cuff-less BP tracking.

Implications to Cuff-Less Blood Pressure Tracking

Experimental observations and interpretations made in this work may lead us to several key implications relevant to the versatility and robustness of wrist BCG-PPG PTT in enabling cuff-less BP tracking under a wide range of postures. First, the evidences for the potential of cuff-less BP tracking via wrist BCG-PPG PTT demonstrated under standing HF posture may generalize directly to HF in sitting posture. Second, even in standing and sitting postures, the aforementioned evidences may not generalize when the arm is in postures other than HF, due to alterations in the vibration transmission characteristics and also possibly due to the distortion in the wrist BCG waveform caused by the deviation of the orientation of the BCG instrument from the head-to-foot direction. Third, body-environment link may have a profound impact on the efficacy of wrist BCG-

PPG PTT via the alteration of the wrist BCG waveform. For example, the aforementioned evidences may not generalize to supine HF posture due to the difference in contact area at the body-bed interface versus foot-floor (in standing) and hip-chair (in sitting) interface.

It is noted that the small change in PAT against body and arm postures does not indicate its robustness against posture but its limited value in tracking BP under a wide range of postures. Indeed, PAT could not capture the effect of the change in BP at the heart level and hydrostatic pressure between the heart and the wrist due to the change in body posture (i.e., standing/sitting to supine).

Lastly, the limitations observed in this work in regard to the versatility and generalizability of the evidence for the potential of cuff-less BP tracking via wrist BCG-PPG PTT in standing HF posture do not simply imply that cuff-less BP tracking via BCG-PPG PTT is not feasible in postures other than specific body and arm postures (i.e., HF in standing and sitting postures). Rather, more profound understanding of the physical mechanisms (e.g., by expanding the mathematical models of the BCG available in the literature [131], [132], [138]) may increase the versatility of the wrist BCG for cuff-less BP tracking. For example, the general applicability of wrist BCG-PPG PTT to wide-ranging postures may be achieved by establishing the understanding of the relationship between various body/arm postures and vibrational transmission characteristics (which is the most prominent disturbance based on this work (Table 7-3)). In addition, the variability in the body-environment interface in various body postures may be detected and accommodated if a rigorous physical insight of its effect on wrist BCG waveform and J wave timing is available. Even if complete understanding of the physical mechanisms turns out to be intractable, the feasibility of cuff-less BP tracking via wrist BCG-PPG PTT in postures other than standing HF posture may still be explored. For example, the BP-dependent behavior of wrist BCG-PPG PTT associated with PC and HS with respect to changes in BP may be studied in order to draw conclusions in regard to the utility of wrist BCG-PPG PTT associated with PC and HS in cuff-less BP tracking.

7.5. Study Limitations

This study has limitations to be accounted for in interpreting its results. First, there are factors that may have impacted the accuracy of BP and PTT measurements. These may include the inaccuracy that may originate from the non-invasive finger BP measurement device and the PPG foot detection method. Our study was conducted in a stable physiological state without any BP-perturbing interventions, in which the BP measurement is reliable, and PPG exhibits high signal quality. Hence, the effect of these inaccuracy on the findings from this study may not be substantial if not negligible. Second, long-term validity of the findings was not shown. It is known that the morphology of the BCG signal is primarily determined by arterial BP waveform [131], [132]. Hence, we anticipate that the findings from this study may remain valid for at least certain longitudinal period (i.e., weeks). Yet, longer-term consistency of the findings must be experimentally proven in a future work.

7.6. Conclusions

This work investigated the variability in the wrist BCG-PPG PTT against wide-ranging body and arm postures. It was illustrated that the posture-dependent wrist BCG-PPG PTT variability is governed by an array of physical mechanisms, including BP at the heart level, hydrostatic pressure between the heart and the wrist, BCG instrument orientation, vibration transmission characteristics, PPG instrument-wrist contact pressure, and body-environment link. Based on the interpretation of the PTT variability with these physical mechanisms, we speculate that the promising potential of the wrist BCG-PPG PTT in cuff-less BP tracking in standing HF posture demonstrated in the existing body of work may generalize to standing and sitting postures with HF, whereas follow-up work is required before its potential in a wide range of body and arm postures can be established. Effort must be invested in particular to achieve more complete understanding of the physical mechanisms responsible for the posture-dependent variability in wrist BCG-PPG PTT as well as rigorous investigation of PTT-BP relationship in various body and arm postures under BP-perturbing interventions.

Chapter 8: Conclusions

Cardiovascular disease (CVD) is the leading cause of mortality and morbidity that imposes a profound impact on health and the economy in the United States as well as globally. Considering the profound negative effect of CVD on public health and the economy, its effective and early detection and management are paramount. Achieving this goal requires ubiquitous and ultra-convenient CV health and risk predictor monitoring. Ballistocardiogram (BCG) has the potential to enable ultra-convenient CV health monitoring due to its close relation to cardiac functions and amenity for convenient measurement.

8.1. Summary of Contributions

Limited understanding of the physical mechanism of BCG has hampered its effective use in CV health and risk assessment. To overcome this challenge, the first part of this dissertation was dedicated to a series of modeling efforts to find the association between CV risk predictors and the BCG using a mathematical model.

Two mathematical models were studied as representations of arterial hemodynamics, and they were compared in terms of their efficacy in reproducing arterial waveforms in humans. An effective but simplistic uniform TL model was compared with an exponential TL model that incorporated a more realistic assumption for arterial tapering in the aorta using experimental invasive human data. This was the first study that investigated the efficacy of incorporating the exponential tapering assumption in humans. The results of this study suggested that the uniform TL model may be more robust and thus preferred as the representation for BP wave propagation in the human aorta relative to the exponentially tapered TL model. In comparison with the uniform

TL model, the exponentially tapered TL model may not provide valid physiological insight into the aortic tapering, and the improvement in the goodness of fit offered by the exponential aortic tapering may only be marginal. Considering that exponential aortic tapering is relevant from a physiological standpoint, future work on more rigorous investigation and refinement of the exponentially tapered TL model will be rewarding.

In the next step, a closed-form mathematical model was developed by the integration of the selected TL model and a prior BCG mechanism model, that could predict the BCG waveform from a single arterial BP waveform. The model can be defined using 6 physiologically interpretable model parameters. A representative BP waveform along with nominal values for model parameters was fed into the model and a BCG waveform was predicted as the output. The simulated BCG waveform showed close similarity with six BCG waveform recordings from the literature that supports the validity of the model.

As the next step, leveraging the closed-form BCG model, an extended mathematical model was developed which allowed for the investigation of the effect of the changes in the CV states on the morphology of the BCG waveform. Thus, the mathematical model can serve as a systematic tool to elucidate the relationship between the CV risk predictors and the BCG. In addition, by perturbing the CV variables that were inputs of the model, the relationship between the features in the BCG waveform and various CV risk predictors was studied. The BCG features deemed sensitive to changes in CV parameters were used in tracking the BP trend. The advantage of this disciplined model-based approach for BCG feature selection was that the set of chosen features is generalizable to different data sets. Therefore, this method has the potential to facilitate ubiquitous BP trend tracking.

To ultimately evaluate the mathematical model developed in this work, ground truth BCG waves must be measured. BCG waveforms recorded with different sensors and different devices have morphological differences. Therefore, a BCG instrumentation apparatus was designed by the study of the devices in the literature and built to give BCG measurements closest in nature to the "true" BCG predicted by the model. The BCG apparatus consisted of a light platform suspended from a rigid frame. Two designs were constructed to accommodate both human and animal subjects. Pilot human and animal studies were performed using the BCG bed apparatus to investigate its capability to measure the BCG waveform. The recordings obtained from the BCG bed were close in morphology to the recordings reported in the literature which confirms the effectiveness of the apparatus in BCG instrumentation.

Rapid technological advances in the field of electronics have made the BCG measured via wrist wearables a viable candidate for CV health monitoring. Toward the ultimate goal of enabling robust cuff-less BP tracking with wrist wearables against postural changes, in the last chapter, the posture-dependent variability in wrist BCG-PPG PTT was investigated. BCG and PPG signals were acquired from 25 subjects under the combination of 3 body (standing, sitting, and supine) and 3 arm (vertical in head-to-foot direction, placed on the chest, and holding a shoulder) postures. PTT was computed as the time interval between the BCG J wave and the PPG foot, and its variability with respect to the 9 postures was analyzed by invoking an array of possible physical mechanisms. This work revealed the posture-induced changes in PTT in depth for the first time, by invoking and quantifying the effect of possible physical mechanisms responsible for such changes. The physical mechanisms discovered, and the subsequent analysis may apply to the study of changes in various PTTs under diverse postures not considered in our work.

8.2. Limitations and Future Work

Overall, this study provides new insights into the association between BCG and CV health parameters. As a result, BCG implemented in daily devices such as bathroom weighing scales and wearables can provide new opportunities for ultra-convenient CV health and disease monitoring. However, there are several limitations that should be addressed in future studies to further pave the path to true convenient BCG-based CV health monitoring.

First, this study lacked simultaneously recorded BCG and BP waveform data. To rigorously evaluate and validate the mathematical model developed in this work, ground truth BCG waves, as well as invasive BP waves, must be measured in the same subjects. Future studies should measure both BCG and BP waveforms under wide-ranging hemodynamic states. Therefore, these studies should be performed in animal subjects that can accommodate invasive measurements and varying hemodynamic states. Then, the experimental data thus obtained should be used to validate the model by assessing its ability to fit the experimental BCG and BP waveforms in different hemodynamic states.

Second, although BCG has a great potential for seamless monitoring of PTT and BP, convenient BP-PTT calibration is still an open challenge for two major reasons. First, there is a need to find the “calibration curve parameters” which are subject-specific. Second, given the fact that the artery stiffens with aging and alters the relationship between PTT and BP, the relation between BP-PTT must be calibrated continuously. Existing PTT-BP calibration techniques typically involve the measurement of reference BP and PTT during BP-perturbing interventions. However, ideal calibration must not require burdensome interventions for the sake of user convenience. Therefore, to enable truly seamless BP tracking efforts must be devoted to developing novel convenient calibration techniques.

Third, the subject cohort used in the study of the PTT-PWA approach in the cuffless BP trend tracking study was not diverse. All subjects were young and healthy with no known cardiovascular disease. In addition, the sample size was not large. The efficacy of the PTT-PWA approach in diverse subject cohorts (such as subjects with isolated systolic hypertension in which DP and SP diverge) needs to be investigated.

Finally, since (i) CV risk predictors and parameters can be easily estimated from arterial BP and blood flow waves but not directly from the BCG, and (ii) BCG unlike BP wave is amenable to convenient instrumentation, the ultimate purpose of the mathematical model is to estimate CV risk predictors from BCG measurement alone. Therefore, future effort must be devoted to characterizing the closed-form BCG model developed in this study and using it to estimate BP waveforms and subsequently CV parameters from BCG recordings.

Bibliography

[1] G. F. Mitchell *et al.*, “Changes in arterial stiffness and wave reflection with advancing age in healthy men and women: The Framingham Heart Study,” *Hypertension*, vol. 43, no. 6, pp. 1239–1245, Jun. 2004, doi: 10.1161/01.HYP.0000128420.01881.aa.

[2] E. Agabiti-Rosei *et al.*, “Central blood pressure measurements and antihypertensive therapy: A consensus document,” in *Hypertension*, Jul. 2007, vol. 50, no. 1, pp. 154–160. doi: 10.1161/HYPERTENSIONAHA.107.090068.

[3] P. Salvi *et al.*, “Comparative study of methodologies for pulse wave velocity estimation,” *Journal of Human Hypertension*, vol. 22, no. 10, pp. 669–677, 2008, doi: 10.1038/jhh.2008.42.

[4] K. Hirata, M. Kawakami, and M. F. O’Rourke, “Pulse wave analysis and pulse wave velocity - A review of blood pressure interpretation 100 years after Korotkov,” *Circulation Journal*, vol. 70, no. 10. Circ J, pp. 1231–1239, 2006. doi: 10.1253/circj.70.1231.

[5] C. H. Chen *et al.*, “Validation of carotid artery tonometry as a means of estimating augmentation index of ascending aortic pressure,” *Hypertension*, vol. 27, no. 2, pp. 168–175, 1996, doi: 10.1161/01.HYP.27.2.168.

[6] D. Gallagher, A. Adji, and M. F. O’Rourke, “Validation of the transfer function technique for generating central from peripheral upper limb pressure waveform,” *American Journal of Hypertension*, vol. 17, no. 11. Am J Hypertens, pp. 1059–1067, Nov. 2004. doi: 10.1016/j.amjhyper.2004.05.027.

[7] R. Mukkamala *et al.*, “Toward Ubiquitous Blood Pressure Monitoring via Pulse Transit Time: Theory and Practice,” *IEEE Transactions on Biomedical Engineering*, vol. 62, no. 8, pp. 1879–1901, 2015, doi: 10.1109/TBME.2015.2441951.

[8] A. Noordergraaf and C. E. Heynekamp, “Genesis of displacement of the human longitudinal ballistocardiogram from the changing blood distribution,” *The American Journal of Cardiology*, vol. 2, no. 6, pp. 748–756, Dec. 1958, doi: 10.1016/0002-9149(58)90272-8.

[9] O. TANNENBAUM, J. A. SCHACK, and H. VESELL, “Relationship between Ballistocardiographic Forces and Certain Events in the Cardiac Cycle,” *Circulation*, vol. 6, no. 4, pp. 586–592, Oct. 1952, doi: 10.1161/01.CIR.6.4.586.

[10] R. S. GUBNER, M. RODSTEIN, and H. E. UNGERLEIDER, “Ballistocardiography; an appraisal of technic, physiologic principles, and clinical value.,” *Circulation*, vol. 7, no. 2, pp. 268–286, 1953, doi: 10.1161/01.CIR.7.2.268.

[11] W. R. Scarborough, R. E. Mason, F. W. Davis, M. L. Singewald, B. M. Baker, and S. A. Lore, “A ballistocardiographic and electrocardiographic study of 328 patients with coronary artery disease; Comparison with results from a similar study of apparently normal persons,” *American Heart Journal*, vol. 44, no. 5, pp. 645–670, 1952, doi: 10.1016/0002-8703(52)90095-1.

[12] O. T. Inan *et al.*, “Ballistocardiography and Seismocardiography : Ballistocardiography and Seismocardiography : A Review of Recent Advances,” *IEEE J. Biomedical and Health Informatics*, vol. 19, no. 4, pp. 1414–1427, 2015, doi: 10.1109/JBHI.2014.2361732.

[13] R. Mukkamala *et al.*, “Towards Ubiquitous Blood Pressure Monitoring via Pulse Transit Time: Theory and Practice,” *IEEE Trans Biomed Eng.*, vol. 62, no. 8, pp. 1879–1901, 2015, doi: 10.1109/TBME.2015.2441951.Towards.

[14] S. Rastegar, H. GholamHosseini, and A. Lowe, “Non-invasive continuous blood pressure monitoring systems: current and proposed technology issues and challenges,” *Australasian Physical and Engineering Sciences in Medicine*, vol. 43, no. 1. Springer Netherlands, pp. 11–28, Nov. 01, 2019. doi: 10.1007/s13246-019-00813-x.

[15] R. M. Wiard, C. A. Figueroa, H. J. Kim, C. A. Taylor, G. T. A. Kovacs, and L. Giovangrandi, “Estimation of central aortic forces in the ballistocardiogram under rest and exercise conditions,” in *Proceedings of the 31st Annual International Conference of the IEEE Engineering in Medicine and Biology Society: Engineering the Future of Biomedicine, EMBC 2009*, 2009, pp. 2831–2834. doi: 10.1109/IEMBS.2009.5333577.

[16] I. STARR, O. HORWITZ, R. L. MAYOCK, and E. B. KRUMBHAAR, “Standardization of the ballistocardiogram by simulation of the heart’s function at necropsy; with a clinical method for the estimation of cardiac strength and normal standards for it.,” *Circulation*, vol. 1, no. 5, pp. 1073–1096, 1950, doi: 10.1161/01.CIR.1.5.1073.

[17] G. Guidoboni *et al.*, “Cardiovascular Function and Ballistocardiogram: A Relationship Interpreted via Mathematical Modeling,” *IEEE Transactions on Biomedical Engineering*, vol. 66, no. 10, pp. 2906–2917, 2019, doi: 10.1109/TBME.2019.2897952.

[18] D. da He, E. S. Winokur, and C. G. Sodini, “An ear-worn vital signs monitor,” *IEEE Transactions on Biomedical Engineering*, vol. 62, no. 11, pp. 2547–2552, Nov. 2015, doi: 10.1109/TBME.2015.2459061.

[19] O. T. Inan, D. Park, L. Giovangrandi, and G. T. A. Kovacs, “Noninvasive measurement of physiological signals on a modified home bathroom scale,” *IEEE Transactions on Biomedical Engineering*, vol. 59, no. 8, pp. 2137–2143, 2012, doi: 10.1109/TBME.2012.2186809.

[20] P. Yousefian *et al.*, “Data mining investigation of the association between a limb ballistocardiogram and blood pressure,” *Physiological Measurement*, vol. 39, no. 7, 2018, doi: 10.1088/1361-6579/aacfe1.

[21] A. D. Wiens, M. Etemadi, S. Roy, L. Klein, and O. T. Inan, “Toward Continuous, Noninvasive Assessment of Ventricular Function and Hemodynamics: Wearable Ballistocardiography,” *IEEE Journal of Biomedical and Health Informatics*, vol. 19, no. 4, pp. 1435–1442, 2015, doi: 10.1109/JBHI.2014.2359937.

[22] C. S. Kim *et al.*, “Ballistocardiogram: Mechanism and Potential for Unobtrusive Cardiovascular Health Monitoring,” *Scientific Reports*, vol. 6, pp. 1–6, 2016, doi: 10.1038/srep31297.

[23] G. Zhang, J. O. Hahn, and R. Mukkamala, “Tube-load model parameter estimation for monitoring arterial hemodynamics,” *Frontiers in Physiology*, vol. 2 NOV, no. November, pp. 1–18, 2011, doi: 10.3389/fphys.2011.00072.

[24] N. Fazeli *et al.*, “Subject-specific estimation of central aortic blood pressure via system identification: preliminary in-human experimental study,” *Medical and Biological Engineering and Computing*, vol. 52, no. 10, pp. 895–904, Sep. 2014, doi: 10.1007/s11517-014-1185-3.

[25] M. Rashedi *et al.*, “Comparative Study on Tube-Load Modeling of Arterial Hemodynamics in Humans,” *ASME Proceedings*, vol. 135, no. March, p. V003T43A003, 2013, doi: 10.1115/DSCC2013-3848.

[26] J. J. Wang and K. H. Parker, “Wave propagation in a model of the arterial circulation,” *Journal of Biomechanics*, vol. 37, no. 4, pp. 457–470, Apr. 2004, doi: 10.1016/j.jbiomech.2003.09.007.

[27] R. Fogliardi, R. Burattini, and K. B. Campbell, “Identification and physiological relevance of an exponentially tapered tube model of canine descending aortic circulation,” *Medical Engineering and Physics*, vol. 19, no. 3, pp. 201–211, 1997, doi: 10.1016/S1350-4533(96)00063-X.

[28] P. Segers and P. Verdonck, “Role of tapering in aortic wave re#ection: hydraulic and mathematical model study,” 2000.

[29] B. E. Westerhof and N. Westerhof, “Uniform tube models with single reflection site do not explain aortic wave travel and pressure wave shape,” *Physiological Measurement*, vol. 39, no. 12, 2018, doi: 10.1088/1361-6579/aaf3dd.

[30] Y. Yao *et al.*, “Mitigation of Instrument-Dependent Variability in Ballistocardiogram Morphology: Case Study on Force Plate and Customized Weighing Scale,” *IEEE Journal of Biomedical and Health Informatics*, vol. 24, no. 1, pp. 69–78, Jan. 2020, doi: 10.1109/JBHI.2019.2901635.

[31] C.-S. Kim, A. M. Carek, O. Inan, R. Mukkamala, and J.-O. Hahn, “Ballistocardiogram-Based Approach to Cuff-Less Blood Pressure Monitoring: Proof-of-Concept and Potential Challenges,” *IEEE Transactions on Biomedical Engineering*, vol. 9294, no. c, pp. 1–1, 2018, doi: 10.1109/TBME.2018.2797239.

[32] J. Alametsä, J. Viik, J. Alakare, A. Värri, and A. Palomäki, “Ballistocardiography in Sitting and Horizontal Positions,” *Physiological Measurement*, vol. 29, no. 9, pp. 1071–1087, 2008, doi: 10.1088/0967-3334/29/9/006.

[33] C. Vlachopoulos, M. O’Rourke, and W. W. Nichols, *McDonald’s Blood Flow in Arteries*. CRC Press, 2011. doi: 10.1201/b13568.

[34] A. A. Brandão *et al.*, “Positioning on Central Arterial Pressure,” *Arquivos Brasileiros de Cardiologia*, vol. 108, no. 2, pp. 100–108, Feb. 2017, doi: 10.5935/abc.20170011.

[35] M. J. Roman *et al.*, “Central pressure more strongly relates to vascular disease and outcome than does brachial pressure: The strong heart study,” in *Hypertension*, Jul. 2007, vol. 50, no. 1, pp. 197–203. doi: 10.1161/HYPERTENSIONAHA.107.089078.

[36] M. J. Roman, P. M. Okin, J. R. Kizer, E. T. Lee, B. V. Howard, and R. B. Devereux, “Relations of central and brachial blood pressure to left ventricular hypertrophy and

geometry: The Strong Heart Study," *Journal of Hypertension*, vol. 28, no. 2, pp. 384–388, 2010, doi: 10.1097/HJH.0b013e328333d228.

[37] B. Williams *et al.*, "Differential impact of blood pressure-lowering drugs on central aortic pressure and clinical outcomes: Principal results of the Conduit Artery Function Evaluation (CAFE) study," *Circulation*, vol. 113, no. 9, pp. 1213–1225, Mar. 2006, doi: 10.1161/CIRCULATIONAHA.105.595496.

[38] F. H. Ding, W. X. Fan, R. Y. Zhang, Q. Zhang, Y. Li, and J. G. Wang, "Validation of the noninvasive assessment of central blood pressure by the sphygmocor and omron devices against the invasive catheter measurement," *American Journal of Hypertension*, vol. 24, no. 12, pp. 1306–1311, Dec. 2011, doi: 10.1038/ajh.2011.145.

[39] A. Wykretowicz *et al.*, "Pulse pressure amplification in relation to body fatness," *British Journal of Clinical Pharmacology*, vol. 73, no. 4, pp. 546–552, Apr. 2012, doi: 10.1111/j.1365-2125.2011.04129.x.

[40] S. Zhou *et al.*, "A review on low-dimensional physics-based models of systemic arteries: Application to estimation of central aortic pressure," *BioMedical Engineering Online*, vol. 18, no. 1, pp. 1–26, 2019, doi: 10.1186/s12938-019-0660-3.

[41] O. Frank, *Die Grundform des arteriellen pulses.* [Place of publication not identified]: [publisher not identified], 1899.

[42] N. Fzeli, "AN ACTIVE NON-INTRUSIVE SYSTEM IDENTIFICATION APPROACH FOR CARDIOVASCULAR HEALTH MONITORING," University of Maryland, 2014.

[43] J.-O. Hahn, A. T. Reisner, and H. H. Asada, “Blind Identification of Two-Channel IIR Systems With Application to Central Cardiovascular Monitoring,” 2009, doi: 10.1115/1.3155011.

[44] G. Swamy, Q. Ling, T. Li, and R. Mukkamala, “Blind Identification of the Aortic Pressure Waveform from Multiple Peripheral Artery Pressure Waveforms,” *Am J Physiol Heart Circ Physiol*, vol. 292, no. 5, pp. H2257-64, 2007, doi: 10.1152/ajpheart.01159.2006.

[45] G. Swamy, D. Xu, N. B. Olivier, and R. Mukkamala, “An adaptive transfer function for deriving the aortic pressure waveform from a peripheral artery pressure waveform,” *American Journal of Physiology - Heart and Circulatory Physiology*, vol. 297, no. 5, pp. 1956–1963, 2009, doi: 10.1152/ajpheart.00155.2009.

[46] J. O. Hahn, A. T. Reisner, F. A. Jaffer, and H. H. Asada, “Subject-Specific Estimation of Central Aortic Blood Pressure Using an Individualized Transfer Function: A Preliminary Feasibility Study,” *IEEE Transactions on Information Technology in Biomedicine*, vol. 16, no. 2, pp. 212–220, 2012, doi: 10.1109/TITB.2011.2177668.

[47] J. O. Hahn, “Individualized Estimation of the Central Aortic Blood Pressure Waveform: A Comparative Study,” *IEEE Journal of Biomedical and Health Informatics*, vol. 18, no. 1, pp. 215–221, 2014.

[48] R. Burattini and K. B. Campbell, “Physiological relevance of uniform elastic tube-models to infer descending aortic wave reflection: a problem of identifiability.,” *Ann Biomed Eng*, vol. 28, no. 5, pp. 512–23, May 2000.

[49] C.-S. Kim, N. Fazeli, M. S. McMurtry, B. A. Finegan, and J.-O. Hahn, “Quantification of Wave Reflection Using Peripheral Blood Pressure Waveforms,” *IEEE Journal of Biomedical and Health Informatics*, vol. 19, no. 1, pp. 309–316, 2015, doi: 10.1109/JBHI.2014.2307273.

[50] G. Swamy, N. B. Olivier, and R. Mukkamala, “Calculation of Forward and Backward Arterial Waves by Analysis of Two Pressure Waveforms,” vol. 57, no. 12, pp. 2833–2839, 2010.

[51] P. Sipkema and N. Westerhof, “Effective length of the arterial system.,” *Ann Biomed Eng*, vol. 3, no. 3, pp. 296–307, Sep. 1975.

[52] M. Gao, G. Zhang, N. B. Olivier, and R. Mukkamala, “Improved pulse wave velocity estimation using an arterial tube-load model.,” *IEEE Trans Biomed Eng*, vol. 61, no. 3, pp. 848–58, 2014, doi: 10.1109/TBME.2013.2291385.

[53] Z. Ghasemi *et al.*, “Estimation of cardiovascular risk predictors from non-invasively measured diametric pulse volume waveforms via multiple measurement information fusion,” *Scientific Reports*, vol. 8, no. 1, pp. 1–11, 2018, doi: 10.1038/s41598-018-28604-6.

[54] B. E. Westerhof, J. P. van den Wijngaard, J. P. Murgo, and N. Westerhof, “Location of a Reflection Site Is Elusive,” *Hypertension*, vol. 52, no. 3, pp. 478–483, Sep. 2008, doi: 10.1161/HYPERTENSIONAHA.108.116525.

[55] S. G. Shroff, D. S. Berger, C. Korcarz, R. M. Lang, R. H. Marcus, and D. E. Miller, “Physiological relevance of T-tube model parameters with emphasis on arterial compliances,” *American Journal of Physiology-Heart and Circulatory Physiology*, vol. 269, no. 1, pp. H365–H374, Jul. 1995, doi: 10.1152/ajpheart.1995.269.1.H365.

[56] N. Fazeli *et al.*, “Subject-specific estimation of central aortic blood pressure via system identification: preliminary in-human experimental study,” *Medical and Biological Engineering and Computing*, vol. 52, no. 10, pp. 895–904, 2014, doi: 10.1007/s11517-014-1185-3.

[57] M. Abdollahzade, C.-S. Kim, N. Fazeli, B. A. Finegan, M. Sean McMurtry, and J.-O. Hahn, “Data-Driven Lossy Tube-Load Modeling of Arterial Tree: In-Human Study,” *Journal of Biomechanical Engineering*, vol. 136, no. 10, p. 101011, 2014, doi: 10.1115/1.4028089.

[58] S. Einav, S. Aharoni, and M. Manoach, “Exponentially tapered transmission line model of the arterial system.,” *IEEE Trans Biomed Eng*, vol. 35, no. 5, pp. 333–9, 1988, doi: 10.1109/10.1390.

[59] K. C. Chang, Y. Z. Tseng, T. S. Kuo, and H. I. Chen, “Impedance and wave reflection in arterial system: simulation with geometrically tapered T-tubes,” *Medical & Biological Engineering & Computing*, vol. 33, no. 5, pp. 652–660, 1995, doi: 10.1007/BF02510782.

[60] B. E. Westerhof *et al.*, “Arterial pressure transfer characteristics: effects of travel time,” *American Journal of Physiology-Heart and Circulatory Physiology*, vol. 292, no. 2, pp. H800–H807, 2007, doi: 10.1152/ajpheart.00443.2006.

[61] M. D. Vaz, T. D. Raj, and K. D. Anura, *Guyton & Hall Textbook of Medical Physiology : a South Asian Edition*.

[62] C.-S. Kim, A. M. Carek, O. T. Inan, R. Mukkamala, and J.-O. Hahn, “Ballistocardiogram-Based Approach to Cuff-Less Blood Pressure Monitoring: Proof-of-Concept and Potential Challenges HHS Public Access,” *IEEE Trans Biomed Eng*, vol. 65, no. 11, pp. 2384–2391, 2018, doi: 10.1109/TBME.2018.2797239.

[63] E. Pinheiro, O. Postolache, and P. S. Girao, “Ballistocardiogram: Model and sensing systems,” Dec. 2016. doi: 10.1109/ICSensT.2016.7796262.

[64] J. W. Gordon, “Certain Molar Movements of the Human Body produced by the Circulation of the Blood.,” *J Anat Physiol*, vol. 11, no. Pt 3, pp. 533–6, Apr. 1877.

[65] Starr, “Studies on the estimation of cardiac ouptut in man, and of abnormalities in cardiac function, from the heart’s recoil and the blood’s impacts; the ballistocardiogram,” 1939.

[66] K. Tavakolian, *Characterization and Analysis of Seismocardiogram for Estimation of Hemodynamic Parameters*. 2010.

[67] W. R. SCARBOROUGH and S. A. TALBOT, “Proposals for ballistocardiographic nomenclature and conventions: revised and extended report of Committee on Ballistocardiographic Terminology.,” *Circulation*, vol. 14, no. 3, pp. 435–450, 1956, doi: 10.1161/01.CIR.14.3.435.

[68] T. J. REEVES, W. B. JONES, and L. L. HEFNER, “Design of an ultra low frequency force ballistocardiograph on the principle of the horizontal pendulum.,” *Circulation*, vol. 16, no. 1, pp. 36–42, 1957, doi: 10.1161/01.CIR.16.1.36.

[69] W. C. Hixson and D. E. Beischer, “Biotelemetry of triaxial ballistocardiogram,” Pensacola, FL, USA, U.S. Naval Medical Center, Pensacola, 1964.

[70] N. Watanabe *et al.*, “Development and Validation of a Novel Cuff-Less Blood Pressure Monitoring Device,” *JACC: Basic to Translational Science*, vol. 2, no. 6, pp. 631–642, 2017, doi: 10.1016/j.jacbts.2017.07.015.

[71] X. Xing and M. Sun, “Optical Blood Pressure Estimation with Photoplethysmography and FFT-Based Neural Networks,” *Biomedical Optics Express*, vol. 7, no. 8, p. 3007, 2016, doi: 10.1364/BOE.7.003007.

[72] K. Atomi, H. Kawanaka, M. S. Bhuiyan, and K. Oguri, “Cuffless Blood Pressure Estimation Based on Data-Oriented Continuous Health Monitoring System,” *Computational and Mathematical Methods in Medicine*, vol. 2017, 2017, doi: 10.1155/2017/1803485.

[73] B. Y. Su *et al.*, “Monitoring the Relative Blood Pressure Using a Hydraulic Bed Sensor System,” *IEEE Transactions on Biomedical Engineering*, vol. 66, no. 3, pp. 740–748, 2019, doi: 10.1109/TBME.2018.2855639.

[74] T.-W. Wang and S.-F. Lin, “Wearable Piezoelectric-Based System for Continuous Beat-to-Beat Blood Pressure Measurement,” *Sensors*, vol. 20, p. Article 851, 2020.

[75] R. Mukkamala *et al.*, “Toward Ubiquitous Blood Pressure Monitoring via Pulse Transit Time: Theory and Practice,” *IEEE Transactions on Biomedical Engineering*, vol. 62, no. 8, pp. 1879–1901, 2015, doi: 10.1109/TBME.2015.2441951.

[76] R. Mukkamala and J.-O. Hahn, “Initialization of Pulse Transit Time-Based Blood Pressure Monitors,” in *The Handbook of Cuffless Blood Pressure Monitoring*, Solà J. and D.-G. R., Eds. Springer, Cham, 2019, pp. 163–190. doi: https://doi.org/10.1007/978-3-030-24701-0_10.

[77] T. H. Huynh, R. Jafari, and W. Y. Chung, “Noninvasive Cuffless Blood Pressure Estimation Using Pulse Transit Time and Impedance Plethysmography,” *IEEE Transactions on Biomedical Engineering*, vol. 66, no. 4, pp. 967–976, 2019, doi: 10.1109/TBME.2018.2865751.

[78] B. Ibrahim and R. Jafari, “Cuffless Blood Pressure Monitoring from an Array of Wrist Bio-impedance Sensors using Subject-Specific Regression Models: Proof of Concept,” *IEEE Transactions on Biomedical Circuits and Systems*, vol. 13, no. 6, pp. 1723–1735, 2019, doi: 10.1109/TBCAS.2019.2946661.

[79] V. P. Rachim and W. Y. Chung, “Multimodal Wrist Biosensor for Wearable Cuff-less Blood Pressure Monitoring System,” *Scientific Reports*, vol. 9, p. Article 7947, 2019, doi: 10.1038/s41598-019-44348-3.

[80] X.-R. Ding, Y.-T. Zhang, J. Liu, W.-X. Dai, and H. K. Tsang, “Continuous Cuffless Blood Pressure Estimation Using Pulse Transit Time and Photoplethysmogram Intensity Ratio,”

IEEE Transactions on Biomedical Engineering, vol. 9294, no. c, pp. 1–1, 2015, doi: 10.1109/TBME.2015.2480679.

[81] X. Ding, B. P. Yan, Y.-T. Zhang, J. Liu, N. Zhao, and H. K. Tsang, “Pulse Transit Time Based Continuous Cuffless Blood Pressure Estimation: A New Extension and A Comprehensive Evaluation,” *Scientific Reports*, vol. 7, no. 1, p. 11554, 2017, doi: 10.1038/s41598-017-11507-3.

[82] Y. Chen, S. Shi, Y. K. Liu, S. L. Huang, and T. Ma, “Cuffless Blood-Pressure Estimation Method using a Heart-Rate Variability-Derived Parameter,” *Physiological Measurement*, vol. 39, no. 9, p. Article 095002, 2018, doi: 10.1088/1361-6579/aad902.

[83] Y. Z. Yoon *et al.*, “Cuff-Less Blood Pressure Estimation Using Pulse Waveform Analysis and Pulse Arrival Time,” *IEEE Journal of Biomedical and Health Informatics*, vol. 22, no. 4, pp. 1068–1074, 2018, doi: 10.1109/JBHI.2017.2714674.

[84] C.-S. Kim, A. M. Carek, O. T. Inan, R. Mukkamala, and J.-O. Hahn, “Ballistocardiogram-Based Approach to Cuffless Blood Pressure Monitoring: Proof of Concept and Potential Challenges,” *IEEE Transactions on Biomedical Engineering*, vol. 65, no. 11, pp. 2384–2391, 2018, doi: 10.1109/TBME.2018.2797239.

[85] C.-S. Kim, A. M. Carek, O. T. Inan, R. Mukkamala, and J.-O. Hahn, “Ballistocardiogram-Based Approach to Cuffless Blood Pressure Monitoring: Proof of Concept and Potential Challenges,” *IEEE Transactions on Biomedical Engineering*, vol. 65, no. 11, pp. 2384–2391, 2018, doi: 10.1109/TBME.2018.2797239.

[86] H. T. Ma, "A Blood Pressure Monitoring Method for Stroke Management," *BioMed Research International*, vol. 2014, p. 571623, 2014, doi: http://dx.doi.org/10.1155/2014/571623.

[87] M. Rashedi *et al.*, "Comparative Study on Tube-Load Modeling of Arterial Hemodynamics in Humans," *ASME Journal of Biomechanical Engineering*, vol. 135, no. March, p. 31005, 2013, doi: 10.1115/1.4023373.

[88] R. Fogliardi, "Identification and physiological relevance of an exponentially tapered tube model of canine descending aortic circulation," *Medical Engineering and Physics*, vol. 19, no. 3, pp. 201–211, 1997.

[89] M. Sugimachi, T. Shishido, K. Miyatake, and K. Sunagawa, "A New Model-Based Method of Reconstructing Central Aortic Pressure from Peripheral Arterial Pressure," *Japanese Journal of Physiology*, vol. 51, no. 2, pp. 217–222, 2001.

[90] K. P. Burnham and D. R. Anderson, *Model Selection and Multimodel Inference: A Practical Information-Theoretic Approach*, 2nd editio. NY, USA: Springer, 2003.

[91] N. R. Gaddum, J. Alastruey, P. Beerbaum, P. Chowienczyk, and T. Schaeffter, "A Technical Assessment of Pulse Wave Velocity Algorithms Applied to Non-Invasive Arterial Waveforms," *Annals of Biomedical Engineering*, vol. 41, no. 12, pp. 2617–2629, 2013, doi: 10.1007/s10439-013-0854-y.

[92] K. S. Matthys *et al.*, “Pulse Wave Propagation in a Model Human Arterial Network : Assessment of 1-D Numerical Simulations against In Vitro Measurements,” *Journal of Biomechanics*, vol. 40, pp. 3476–3486, 2007, doi: 10.1016/j.jbiomech.2007.05.027.

[93] J. J. Wang and K. H. Parker, “Wave Propagation in a Model of the Arterial Circulation,” *Journal of Biomechanics*, vol. 37, pp. 457–470, 2004, doi: 10.1016/j.jbiomech.2003.09.007.

[94] P. Reymond, F. Merenda, F. Perren, D. Rufenacht, and N. Stergiopulos, “Validation of a One-Dimensional Model of the Systemic Arterial Tree,” *American Journal of Physiology*, vol. 297, pp. H208–H222, 2009, doi: 10.1152/ajpheart.00037.2009.

[95] R. Fogliardi, “Identification and physiological relevance of an exponentially tapered tube model of canine descending aortic circulation,” *Medical Engineering and Physics*, vol. 19, no. 3, pp. 201–211, 1997.

[96] P. Segers and P. Verdonck, “Role of Tapering in Aortic Wave Reflection: Hydraulic and Mathematical Model Study,” *Journal of Biomechanics*, vol. 33, no. 3, pp. 299–306, 2000, doi: 10.1016/S0021-9290(99)00180-3.

[97] P. M. Sundell and M. R. Roach, “The Role of Taper on the Distribution of Atherosclerosis in the Human Infra-Renal Aorta,” *Atherosclerosis*, vol. 139, no. 1, pp. 123–129, 1998, doi: 10.1016/S0021-9150(98)00068-9.

[98] A. Noordergraaf, *Circulatory System Dynamics*. New York, NY: Academic Press, 1978.

[99] A. Mousavi, A. Tivay, B. Finegan, M. S. McMurtry, R. Mukkamala, and J. O. Hahn, “Tapered vs. Uniform tube-load modeling of blood pressure wave propagation in human

aorta," *Frontiers in Physiology*, vol. 10, no. JUL, p. 974, Aug. 2019, doi: 10.3389/fphys.2019.00974.

[100] W. W. von Wittern, "Ballistocardiography with elimination of the influence of the vibration properties of the body," *American Heart Journal*, vol. 46, no. 5, pp. 705–714, 1953, doi: 10.1016/0002-8703(53)90223-3.

[101] M. B. Rappaoport, "Displacement, velocity, and acceleration ballistocardiograms as registered with an undamped bed of ultrlow natural frequency," *Journal of Chemical Information and Modeling*, vol. 53, no. 9, pp. 1689–1699, 1955, doi: 10.1017/CBO9781107415324.004.

[102] T. J. REEVES, W. B. JONES, and L. L. HEFNER, "Design of an ultra low frequency force ballistocardiograph on the principle of the horizontal pendulum.," *Circulation*, vol. 16, no. 1, pp. 36–42, 1957, doi: 10.1161/01.CIR.16.1.36.

[103] Malt, "Depressant Effect of Ether on the Heart: A Study With the Ultralow-Frequency Force Ballistocardiograph," 1957.

[104] C. K. Battye, D. C. Deuchar, R. E. George, R. D. Moore, P. J. Winter, and G. Hospital, "Simple, calibrated, ultra-low frequency ballistocardiograph*," vol. 4, pp. 543–554, 1966.

[105] S. A. TALBOT and W. K. HARRISON, "Dynamic comparison of current ballistocardiographic methods. III. Derivation of cardiovascular force from body motions.," *Circulation*, vol. 12, no. 6, pp. 1022–1033, 1955, doi: 10.1161/01.CIR.12.6.1022.

[106] S. L. O. Martin *et al.*, “Weighing Scale-Based Pulse Transit Time is a Superior Marker of Blood Pressure than Conventional Pulse Arrival Time,” *Scientific Reports*, vol. 6, no. October, pp. 1–8, 2016, doi: 10.1038/srep39273.

[107] C. S. Kim, A. M. Carek, R. Mukkamala, O. T. Inan, and J. O. Hahn, “Ballistocardiogram as proximal timing reference for pulse transit time measurement: Potential for cuffless blood pressure monitoring,” *IEEE Transactions on Biomedical Engineering*, vol. 62, no. 11, pp. 2657–2664, 2015, doi: 10.1109/TBME.2015.2440291.

[108] Y. Yao *et al.*, “Unobtrusive estimation of cardiovascular parameters with limb ballistocardiography,” *Sensors (Switzerland)*, vol. 19, no. 13, p. 2922, Jul. 2019, doi: 10.3390/s19132922.

[109] P. Yousefian *et al.*, “Data mining investigation of the association between a limb ballistocardiogram and blood pressure,” *Physiological Measurement*, vol. 39, no. 7, p. 075009, Aug. 2018, doi: 10.1088/1361-6579/aacfe1.

[110] J. H. Shin, K. M. Lee, and K. S. Park, “Non-constrained monitoring of systolic blood pressure on a weighing scale,” *Physiological Measurement*, vol. 30, no. 7, pp. 679–693, 2009, doi: 10.1088/0967-3334/30/7/011.

[111] K. H. Wesseling, J. R. Jansen, J. J. Settels, and J. J. Schreuder, “Computation of aortic flow from pressure in humans using a nonlinear, three-element model,” *Journal of Applied Physiology*, vol. 74, no. 5, pp. 2566–2573, 1993, doi: 10.1152/jappl.1993.74.5.2566.

[112] K. H. Wesseling, J. R. Jansen, J. J. Settels, and J. J. Schreuder, “Computation of aortic flow from pressure in humans using a nonlinear, three-element model.,” *J Appl Physiol (1985)*, vol. 74, no. 5, pp. 2566–73, 1993, doi: 10.1152/jappl.1993.74.5.2566.

[113] N. Saouti, N. Westerhof, P. E. Postmus, and A. Vonk-Noordegraaf, “The arterial load in pulmonary hypertension,” *Eur Respir Rev*, vol. 19, no. 117, pp. 197–203, Sep. 2010, doi: 10.1183/09059180.00002210.

[114] Y. Yao *et al.*, “Unobtrusive estimation of cardiovascular parameters with limb ballistocardiography,” *Sensors (Switzerland)*, vol. 19, no. 13, pp. 1–18, 2019, doi: 10.3390/s19132922.

[115] P. Yousefian *et al.*, “Pulse Transit Time-Pulse Wave Analysis Fusion Based on Wearable Wrist Ballistocardiogram for Cuff-Less Blood Pressure Trend Tracking,” *IEEE Access*, vol. 8, pp. 138077–138087, 2020, doi: 10.1109/ACCESS.2020.3012384.

[116] H. C. Burger, A. Noordergraaf, and A. M. W. Verhagen, “Physical basis of the low-frequency ballistocardiograph,” *American Heart Journal*, vol. 46, no. 1, pp. 71–83, 1953, doi: 10.1016/0002-8703(53)90241-5.

[117] J. L. Nickerson and C. H. J, “The design of the ballistocardiograph,” *Am J Physiol*, vol. 142, no. 1, p. 960103, 1944.

[118] W. Scarborough, “Comments on progress in ballistocardiographic research and the current state of the art,” 1964.

[119] M. B. Rappaport, “Displacement, velocity, and acceleration ballistocardiograms as registered with an undamped bed of ultralow natural frequency: II. Instrumental considerations,” *American Heart Journal*, vol. 52, no. 5, pp. 643–652, 1956, doi: 10.1016/0002-8703(56)90020-5.

[120] H. C. Burger, A. Noordergraaf, J. J. M. Korstenm, and P. Ullersma, “Physical Basis of Ballistocardiography. IV,” *American Heart Journal*, vol. 52, no. 5, 1956.

[121] D. J. Ewins, “Modal Testing: Theory, Practice and Application, 2nd Edition SERIES,” p. 576, 2009, Accessed: Nov. 01, 2021. [Online]. Available: https://www.wiley.com/en-us/9780863802188

[122] H. C. Burger and A. Noordergraaf, “Physical Basis of Ballistocardiography. III,” *American Heart Journal*, 1956.

[123] J. Pan and W. J. Tompkins, “A Real-Time QRS Detection Algorithm,” *IEEE Transactions on Biomedical Engineering*, vol. BME-32, no. 3, pp. 230–236, 1985, doi: 10.1109/TBME.1985.325532.

[124] R. Mukkamala, J. Hahn, O. T. Inan, L. K. Mestha, C. Kim, and T. Hakan, “Toward Ubiquitous Blood Pressure Monitoring via Pulse Transit Time : Theory and Practice,” *IEEE Transactions on Biomedical Engineering*, vol. 62, no. 8, pp. 1879–1901, 2015.

[125] L. Peter, N. Noury, and M. Cerny, “A Review of Methods for Non-Invasive and Continuous Blood Pressure Monitoring: Pulse Transit Time Method is Promising?,” *Irbm*, vol. 35, no. 5, pp. 271–282, 2014, doi: 10.1016/j.irbm.2014.07.002.

[126] D. Buxi, J. Redouté, and M. R. Yuce, “A Survey on Signals and Systems in Ambulatory Blood Pressure Monitoring Using Pulse Transit Time,” *Physiological Measurement*, vol. 36, pp. R1–R26, 2015, doi: 10.1088/0967-3334/36/3/R1.

[127] M. Sharma *et al.*, “Cuff-Less and Continuous Blood Pressure Monitoring: A Methodological Review,” *Technologies (Basel)*, vol. 5, no. 2, p. 21, 2017, doi: 10.3390/technologies5020021.

[128] C.-S. Kim, A. M. Carek, R. Mukkamala, O. T. Inan, and J.-O. Hahn, “Ballistocardiogram as Proximal Timing Reference for Pulse Transit Time Measurement: Potential for Cuffless Blood Pressure Monitoring,” *IEEE Transactions on Biomedical Engineering*, vol. 62, no. 11, pp. 2657–2664, 2015.

[129] S. L. Martin *et al.*, “Weighing Scale-Based Pulse Transit Time is a Superior Marker of Blood Pressure than Conventional Pulse Arrival Time,” *Scientific Reports*, vol. 6, no. November, p. 39273, 2016, doi: 10.1038/srep39273.

[130] P. Yousefian *et al.*, “The Potential of Wearable Limb Ballistocardiogram in Blood Pressure Monitoring via Pulse Transit Time,” *Scientific Reports*, vol. 9, p. Article 10666, 2019.

[131] C.-S. Kim *et al.*, “Ballistocardiogram: Mechanism and Potential for Unobtrusive Cardiovascular Health Monitoring,” *Scientific Reports*, vol. 6, p. 31297, 2016, doi: 10.1038/srep31297.

[132] P. Yousefian *et al.*, “Physiological Association between Limb Ballistocardiogram and Arterial Blood Pressure Waveforms: A Mathematical Model-Based Analysis,” *Scientific Reports*, vol. 9, p. 5146, 2019, doi: 10.1038/s41598-019-41537-y.

[133] E. Hermeling, K. D. Reesink, R. S. Reneman, and A. P. G. Hoeks, “Measurement of Local Pulse Wave Velocity: Effects of Signal Processing on Precision,” *Ultrasound in Medicine and Biology*, vol. 33, no. 5, pp. 774–781, 2007, doi: 10.1016/j.ultrasmedbio.2006.11.018.

[134] A. Chandrasekhar, M. Yavarimanesh, K. Natarajan, J.-O. Hahn, and R. Mukkamala, “PPG Sensor Contact Pressure Should be Taken into Account for Cuff-Less Blood Pressure Measurement,” *IEEE Transactions on Biomedical Engineering*, vol. 67, no. 11, pp. 3134–3140, 2020, doi: 10.1109/tbme.2020.2976989.

[135] R. A. Payne, “Pulse Transit Time Measured from the ECG: An Unreliable Marker of Beat-to-Beat Blood Pressure,” *Journal of Applied Physiology*, vol. 100, no. 1, pp. 136–141, 2006, doi: 10.1152/japplphysiol.00657.2005.

[136] R. W. Stafford, W. S. Harris, and A. M. Weissler, “Left Ventricular Systolic Time Intervals as Indices of Postural Circulatory Stress in Man,” *Circulation*, vol. 41, no. 3, pp. 485–492, 1970, doi: 10.1161/01.CIR.41.3.485.

[137] J. H. Houtveen, P. F. C. Groot, and E. J. C. De Geus, “Effects of Variation in Posture and Respiration on RSA and Pre-Ejection Period,” *Psychophysiology*, vol. 42, no. 6, pp. 713–719, 2005, doi: 10.1111/j.1469-8986.2005.00363.x.

[138] G. Guidoboni *et al.*, "Cardiovascular Function and Ballistocardiogram: A Relationship Interpreted via Mathematical Modeling," *IEEE Transactions on Biomedical Engineering*, vol. 66, no. 10, pp. 2906–2917, 2019, doi: 10.1109/TBME.2019.2897952.

[139] S. Shin *et al.*, "Posture-Dependent Variability in Wrist Ballistocardiogram-Photoplethysmogram Pulse Transit Time: Implication to Cuff-Less Blood Pressure Tracking," *IEEE Transactions on Biomedical Engineering*, vol. 69, no. 1, pp. 347–355, Jan. 2022, doi: 10.1109/TBME.2021.3094200.